Title
Intratidal Transport and Mixing Processes at the Shoal-Channel Interface in a Partially-Stratified Estuary

Author
Collignon, Audric

Publication Date
2012

Peer reviewed|Thesis/dissertation

Intratidal Transport and Mixing Processes at the Shoal-Channel Interface in a Partially-Stratified Estuary

by

Audric Collignon

A dissertation submitted in partial satisfaction of the
requirements for the degree of
Doctor of Philosophy

in

Engineering - Civil and Environmental Engineering

in the

Graduate Division

of the

University of California, Berkeley

Committee in charge:

Professor Mark T. Stacey, Chair
Assistant Professor Evan A. Variano
Professor Michael Manga

Fall 2012

Intratidal Transport and Mixing Processes at the Shoal-Channel Interface in a Partially-Stratified Estuary

Abstract

Intratidal Transport and Mixing Processes at the Shoal-Channel Interface in a Partially-Stratified Estuary

by

Audric Collignon

Doctor of Philosophy in Engineering - Civil and Environmental Engineering

University of California, Berkeley

Professor Mark T. Stacey, Chair

This work addresses transport and mixing processes at work during each tide across the shoal-channel interface. These are fundamental to long-term, large-scale, salt, sediment and biomass budgets yet remain poorly characterized and understood. Most of the analyses presented here are based on field observations collected in South San Francisco Bay, CA, during winter 2009.

Horizontal transport across the interface is governed by the transverse flow, which is predominantly characterized by the presence of one or two lateral circulation cells. This study reveals that these circulation cells can evolve more rapidly than previously thought, reversing multiple times during a single ebb tide. The formation of convergence fronts is found to be sensitive to the direction of the lateral circulation and is therefore marked by a similar intratidal variability. It is hypothesized that these intratidal variations are the result of competing lateral density gradients which are the main forcing mechanism for transverse flows. The outcome of this competition depends strongly on vertical mixing conditions on the slope.

Vertical mixing on the slope is driven for the most part by turbulence generated in the bottom boundary layer, except for occasional late-ebb bursts generated by internal vertical shears. These internal shears result from the destabilizing straining of lateral shear by the lateral circulation which overcomes in this case the stabilizing straining of lateral density gradients.

Horizontal mixing across the interface is quantified indirectly and is found to be driven mostly by lateral shear instabilities, but is also affected by lateral dynamics. As a result, transverse mixing also displays significant intratidal variability. This result poses a challenge to existing parametrization developed for steady shear layers.

To Julia
To my parents Marie and Yann

Contents

List of Figures

List of Tables

Acknowledgments

Many thanks to my advisor Professor Mark Stacey for his insightful and enthusiastic guidance, to my family for their support, to my fellow PhD students and postdocs at UC Berkeley Bowen Zhou, Rusty Holleman, Cristina Poindexter, Gabriele Bellani, Kevin Hsu, Rudi Schuech, Wayne Wagner, Ian Tse, Mary Cousins, Andreas Brand, Jason Simon, Maureen Downing-Kunz, Lauren Goodfriend, Megan Williams, Lissa MacVean, Susan Willis, Margaret Byron, Steve Gladding and Arthur Wiedmer for their assistance and their company, to Dr Jessica Lacy and the staff from USGS for their assistance with field work and insightful comments, to Professors Evan Variano, Tina Chow, Jim Hunt, Rob Harley, Michael Manga, Parker MacCready and Dr Rocky Geyer for many interesting comments, questions, discussions and lectures, to Shelley Okimoto for her dedication and her help. Funding for this research was provided by the National Science Foundation.

Chapter 1

Introduction

Estuaries are special regions of the coastal ocean, where freshwater carried by rivers meets denser, saline ocean waters. Rivers also transport nutrients and suspended sediments and as a result estuaries are often characterized by high biological productivity (Peterson and Festa 1984) and large volumes of sediment are displaced (Geyer et al. 2004) or accumulate every year (Geyer et al. 2001). The convergence of saline and freshwater in estuaries can be an efficient trapping mechanism for pollutants and biomass which often results in persistent water quality issues (MacCready and Geyer 2010), exacerbated by the presence of dense urban areas around many estuaries worldwide. Water agencies also need to quantify the length of salinity intrusion, the distance over which saline water penetrates an estuary, to assess where and when water becomes unsuitable for drinking water or irrigation supply. The first section of this chapter describes the typical features of a partially-stratified shoal-channel estuary and where this work fits in the field of estuarine Physics. The second section introduces South San Francisco Bay, the system studied here. The third section outlines the research questions adressed in this work.

1.1 Background

The partially-stratified shoal-channel estuary

Various estuarine classification methods have been developed over the years, based each on different criteria such as the water balance, geomorphology, the salinity structure and the hydrodynamics (Valle-Levinson et al. 2010). Characterizing the typical partially-stratified shoal-channel estuary involves two of these classifications: one based on salinity structure and the other on geomorphology.

Pritchard (1952a) proposed a geomorphological classification separating three types of estuaries. The first class is the fjord, characterized by a shallow sill at the mouth and a deep (depth $h \geq 100\,\mathrm{m}$) but narrow basin carved by former glaciers. Fjords are typically found at high latitudes. The second class is the bar-built estuary, resulting from the formation of

an offshore sand-bar or spit. This type of estuary is common in subtropical regions of North and South America. The third class is the coastal plain estuary, formed by the drowning of a former river valley due to subsidence or sea-level rise at the end of the last glacial age. These estuaries are typically shallow and wide and characterized by one or few channels (depth $h \sim 10 - 30\,\mathrm{m}$) surrounded by shallow shoals (depth $h \leq 10\,\mathrm{m}$). This type of estuary are more common on the East Coast of the United States and Canada (e.g. Delaware Bay, Chesapeake Bay, Saint Lawrence River estuary) than on the West Coast (e.g. South San Francissco Bay).

Estuaries have also been classified based on their vertical density structure, and more specifically the strength of the density stratification. Given a density field $\rho(x, y, z, t)$, stratification is quantified by the buoyancy frequency N defined as:

$$N^2 = \frac{-g}{\rho_0}\frac{\partial \rho}{\partial z} \tag{1.1}$$

where $g = 9.81\mathrm{m\,s^{-2}}$ is the gravitational acceleration at sea-level and $\rho_0 = 1028\,\mathrm{kg\,m^{-3}}$ is the density of seawater in its reference state ($T_0 = 283\,\mathrm{K}$, $s_0 = 35\,\mathrm{psu}$, $p_0 = 1.01\,10^5\,\mathrm{Pa}$). Although various parameters have been proposed for this classification without a consensus being reached (Geyer and Ralston 2011), a common approach relies on two parameters quantifying the buoyancy forcing from the river discharge and vertical mixing generated by tidal currents (Valle-Levinson et al. 2010). Wind and surface waves may also drive vertical mixing but their contribution varies widely among estuaries and is beyond the scope of this work. Buoyancy forcing increases with river discharge Q_{river} but decreases with the characteristic depth of the estuary h, and tidal mixing increases with the characteristic tidal currents velocity u_{tide} but decreases with h. Strong tidal mixing corresponds then to large tidal currents in shallow estuaries while strong buoyancy forcing corresponds to large river outflows in shallow estuaries.

Four main states in that parameter space are frequently referred to: the salt-wedge state corresponds to strong buoyancy forcing and weak/moderate tidal mixing (e.g. Mississippi, LA), the strongly-stratified state corresponds to weak/moderate buoyancy forcing and weak tidal mixing (e.g. Puget Sound, WA), the well-mixed state corresponds to weak buoyancy forcing and strong tidal mixing. Finally the partially-mixed state corresponds to weak/moderate buoyancy forcing and moderate/strong tidal mixing. Many temperate estuaries including Chesapeake Bay and South San Francisco Bay are frequently found in this last state, characterized by weak, continuous stratification extending over most of the water column except in the well-mixed bottom boundary layer (Valle-Levinson et al. 2010). It is important to note that a single estuary can vary from one state to another over various timescales (e.g. tidal, neap-spring or seasonal cycles), and as a result the term partially-stratified describes a specific dynamical regime rather than a type of estuary.

Transport and mixing in estuaries: the importance of the shoal-channel interface

Most of the research efforts to quantify transport and mixing in estuaries have focused on salinity, mainly because it is the most dynamically active scalar and as such its distribution must be known to address the dynamics of flows in estuaries. The mainstream approach to describe transport and mixing of salinity in an estuary relies on decomposing velocity u and salinity s in three components (Fischer 1972; Lerczak et al. 2006):

$$u = \underbrace{\left[\frac{\langle \int u dA \rangle}{A_0}\right]}_{u_0} + \underbrace{\left[\frac{\langle udA \rangle}{dA_0} - \frac{\langle \int u dA \rangle}{A_0}\right]}_{u_1} + u_2 \tag{1.2}$$

$$s = \underbrace{\left[\frac{\langle \int s dA \rangle}{A_0}\right]}_{s_0} + \underbrace{\left[\frac{\langle sdA \rangle}{dA_0} - \frac{\langle \int s dA \rangle}{A_0}\right]}_{s_1} + s_2 \tag{1.3}$$

where $A_0 = \langle \int dA \rangle$ is the tidally-averaged (brackets $\langle\rangle$) cross-section area, $dA_0 = \langle dA \rangle$ is the tidally-averaged area of a differential section element (which in this framework is allowed to expand and contract as the surface elevation fluctuates with tides). The different velocity and salinity components are the tidally-averaged and sectionally-averaged velocity u_0 and salinity s_0, the tidally-averaged but sectionally-varying velocity u_1 and salinity s_1 and the tidally-varying and sectionally-varying residuals u_2 and s_2. Using this decomposition, the tidally-averaged salt flux F through a cross-section is (MacCready and Banas 2011):

$$\underbrace{\left\langle \int usdA \right\rangle}_{F} = \underbrace{u_0 s_0 A_0}_{F_R} + \underbrace{\int u_1 s_1 dA_0}_{F_E} + \underbrace{\left\langle \int u_2 s_2 dA \right\rangle}_{F_T} \tag{1.4}$$

The first term F_R on the right hand side represents the tendency of the river flow to advect salt down-estuary (seaward).

The second term F_E represents the salt flux associated with the subtidal (tidally-averaged) exchange flow. In many estuaries, this exchange flow u_1 in the absence of wind is typically directed up-estuary near the bed and down-estuary near the surface, while the subtidal salinity field s_1 is characterized by higher salinity near the bed and lower salinity near the surface (Pritchard 1952b; MacCready 1999). This exchange flow can result from a combination of various physical processes such as the longitudinal density gradient (Hansen and Rattray 1965), cross-channel advection (Lerczak and Geyer 2004; Scully et al. 2009), and tidal asymmetries in vertical turbulent mixing (Stacey et al. 2001), but the associated salt flux F_E is generally directed up-estuary (MacCready and Banas 2011) and has been parametrized insightfully by Hansen and Rattray (1965), Monismith et al. (2002) and MacCready (2004) to name a few.

The third term F_T represents the cross-correlation of the velocity and salinity field at tidal and higher frequencies, and has been traditionally parametrized as a Fickian diffusion

process (Hansen and Rattray 1965):

$$F_T = -K_H \frac{\partial s_0}{\partial x} \tag{1.5}$$

where $\partial s_0/\partial x$ is the along-estuary gradient of the tidally-averaged and sectionally-averaged salinity and K_H is a longitudinal dispersion parameter. This parameter K_H accounts for diverse physical processes such as steady and oscillatory shear dispersion (Taylor 1953; Fischer et al. 1979). Horizontal shears typically result from changes in coastline (e.g. flow separation behind a headland) or bathymetry (e.g. shoal-channel interface) and have been rather extensively studied (Signell and Geyer 1991; Li and O'Donnell 1997; Valle-Levinson and Atkinson 1999), but mixing processes across these shear zones are still poorly characterized and a general theory for horizontal dispersion in estuaries remains far ahead (MacCready and Banas 2011).

Transport across the shoal-channel interface

In shoal-channel estuaries, the transport within the shoals and along the estuary is defined by large scale circulation but transport across the shoal-channel interface is governed by smaller scale dynamics. These local processes are crucial to the basin-scale transport of sediment and other scalars because the length scale of the tidal excursion and thus longitudinal transport is much greater in the channel than in the shoals (Lucas et al. 1999).

Transverse flows in regions of sloping bathymetry have long been studied and typically involve a transverse circulation with lateral currents flowing in different directions at different depths. Various mechanisms driving these circulations have been identified: Nunes and Simpson (1985) found that the transverse density gradient created by differential advection of the longitudinal density gradient acts as the dominant mechanism in the Conwy river, UK. The process of differential advection is linked to the transverse shear that develops in a region of laterally-changing bathymetry: the effect of bed friction increases with decreasing depth such that tidal currents are typically slower over the shoals than in the channel. As a result freshwater during the ebb or ocean water during the flood is advected faster in the channel than over the shoal. Huzzey and Brubaker (1988) reached a similar conclusion in their study of the York river, Virginia, USA, a more typical shoal-channel estuary, and found that the shoal-channel geometry accentuates differential advection. Chen et al. (2009) showed recently that axial winds could also drive differential advection.

Other mechanisms driving lateral circulations include channel curvature (Geyer 1993; Lacy and Monismith 2001), non-linear tidal propagation in an estuary with transverse variations in bathymetry (Li and O'Donnell 1997), tidal phase lag between channel and shoals (Valle-Levinson et al. 2000), Coriolis forcing in boundary and interfacial Ekman layers (Ott and Garrett 1998; Ott et al. 2002) and cross-channel density gradients in a diffusive boundary layer over a sloping bottom (Garrett et al. 1993). More recently, Cheng et al. (2009) identified lateral variations in vertical mixing between the thalweg and the shoal as the dominant mechanism producing a lateral density gradient in the lower Passaic river, New Jersey, USA.

The effects of transverse flows on longitudinal dispersion rates have been recognized early (Erdogan and Chatwin 1967; Smith 1976): the transverse circulation circles water throughout the cross-section and therefore decreases the characteristic timescale of transverse mixing. In oscillatory flows, this timescale is of crucial importance in quantifying longitudinal dispersion: if the lateral mixing timescale is much smaller than the tidal period, shear dispersion will operate similarly as in a steady flow, whereas shear dispersion will be minimal if the lateral mixing timescale is much larger than the tidal period (Fischer et al. 1979).

The effects of the lateral circulation on sediment transport have received increasing attention recently. Observations by Fugate et al. (2007) in the upper reach of Chesapeake Bay, USA, revealed a net (tidally-averaged) sediment flux directed towards the left slope (looking seaward). However, the authors pointed out that this result is not consistent with the local geomorphology (wider shoal on the right side) which suggests that the net sediment transport over longer timescales should be directed towards the right slope. Recent idealized numerical simulations have showed similarly that within the salt intrusion, net sediment transport is directed towards the right side of the estuary (Chen and Sanford 2008; Huijts et al. 2011) in the absence of wind. When axial wind forcing is important, Chen et al. (2009) showed that the net sediment flux (integrated the duration of the wind event, a few days in their case) is symmetrical and directed from channel to shoals for down-estuary winds and from shoals to channel for up-estuary winds. Despite this recent progress, our understanding of sediment transport across the shoal-channel interface and the associated geomorphological implications remains largely incomplete.

Vertical turbulent mixing at the shoal-channel interface

Velocity $\underline{u} = (u, v, w)$ and density ρ in turbulent flows can be decomposed as the sum of a mean and fluctuating component (Pope 2000):

$$(u, v, w) = (\overline{u}, \overline{v}, \overline{w}) + (u', v', w') \tag{1.6}$$

$$\rho = \overline{\rho} + \rho' \tag{1.7}$$

where (u', v', w') and ρ' represent the turbulent fluctuations and $(\overline{u}, \overline{v}, \overline{w})$ and $\overline{\rho}$ are the Reynolds averaged velocity and density. In practice, these Reynolds averaged quantities are usually estimated with a temporal average over a period much longer than the largest turbulent timescale (which is typically smaller than a few minutes in estuaries) (Fischer et al. 1979) but much smaller than the characteristic timescale of the mean flow evolution (Stacey et al. 2012), for instance the M2 tidal period (12.4 hours). The turbulent kinetic energy (TKE):

$$q^2 = \overline{u'^2} + \overline{v'^2} + \overline{w'^2} \tag{1.8}$$

is produced by the interaction of turbulent motions with spatial variations of the mean velocity field. This source of TKE is called shear production and writes (Kundu and Cohen 2008):

$$P = -\overline{u_i' u_j'} \frac{\partial \overline{u_i}}{\partial x_j} \tag{1.9}$$

In practice, vertical shears $\partial\overline{u}/\partial z$ and $\partial\overline{v}/\partial z$ dominate shear production such that (4.4) simplifies to (Stacey et al. 2012):

$$P \simeq -\overline{u'w'}\frac{\partial\overline{u}}{\partial z} - \overline{v'w'}\frac{\partial\overline{v}}{\partial z} \tag{1.10}$$

In a stratified turbulent flow, TKE can be lost locally to viscous dissipation quantified by the TKE dissipation rate (Kundu and Cohen 2008):

$$\epsilon = \frac{1}{2}\nu\overline{\left(\frac{\partial u_i'}{\partial x_j} + \frac{\partial u_j'}{\partial x_i}\right)^2} \tag{1.11}$$

or conversion to potential energy through the mixing of the density field, a process quantified by the buoyancy flux (Turner 1973):

$$B = -\frac{g}{\rho}\overline{\rho'w'} \tag{1.12}$$

The opposite roles of shear production (source of TKE) and buoyancy flux (sink of TKE in a stably stratified fluid) highlight the competition between shear and stratification which is frequently parametrized using the gradient Richardson Number (Turner 1973):

$$\mathrm{Ri_g} = \frac{N^2}{S^2} = \frac{-\frac{g}{\rho_0}\frac{\partial\overline{\rho}}{\partial z}}{\left(\frac{\partial\overline{u}}{\partial z}\right)^2 + \left(\frac{\partial\overline{v}}{\partial z}\right)^2} \tag{1.13}$$

For small values of $\mathrm{Ri_g}$, shear overcomes stratification and turbulence develops as the flow becomes unstable, whereas for large values of $\mathrm{Ri_g}$ stratification overcomes shear and the flow will remain stable. A frequently assumed critical value is $\mathrm{Ri_g} = 1/4$ (Miles 1961; Geyer et al. 2008).

Our understanding of turbulence in partially-stratified estuaries has improved considerably with the recent development of new observational techniques. Reynolds stresses are usually estimated locally from the covariance of the different components of the velocity fluctuations (Trowbridge et al. 1999) or remotely from the variances of the along-beam velocity fluctuations measured by an Acoustic Doppler Current Profiler (ADCP) (Lohrmann et al. 1990; Stacey et al. 1999a). The Reynolds stresses can be combined with collocated velocity shears to yield the turbulent kinetic energy (TKE) shear production (Stacey et al. 1999b; Lu and Lueck 1999). This beam variance method has also been extended by Stacey (2003) to estimate the vertical turbulent diffusion of TKE from the third moments of an ADCP's along-beam velocity fluctuations. Various methods have been used to measure TKE dissipation rates in inland and coastal waters: estimates from microstructure shear profilers (Rippeth et al. 2001), from pulse-coherent ADCPs using the inertial dissipation method (Lorke and Wuest 2005) or from standard ADCPs using the structure function method (Wiles et al. 2006) to name a few. Buoyancy fluxes are usually estimated by quantifying the vertical

spreading of a deliberate tracer (Chant et al. 2007), or through the covariance of collocated and simultaneous point measurements of velocity and salinity (Kawanisi and Yokosi 1994), density (Gargett and Moum 1995) or speed of sound (Shaw et al. 2001). Although care is required when interpreting these in-situ observations as they can be noisy and often rely on simplifying assumptions such as steady, isotropic and homogeneous turbulence (Ivey et al. 2008), they have enabled us to identify the important turbulent processes at play in partially-stratified estuaries and coastal waters.

In the absence of wind, turbulence in estuaries typically develops as a result of the no-slip boundary condition at the bed (Peters 1999; Peters and Bokhorst 2000). The first comprehensive description of the vertical variability of TKE budget in a partially-stratified estuary has been given by Stacey et al. (1999b). In the bottom boundary layer, turbulence is largely unaffected by density stratification as suggested by gradient Richardson numbers smaller than the critical value of one fourth and shear production is greater than the buoyancy flux and the dissipation rate combined, suggesting a negative or upward turbulent vertical diffusion of TKE. Above the boundary layer sits a transition region where local shear production approximately balances local destruction of TKE through buoyancy flux and viscous dissipation, and turbulent mixing of density is maximally efficient. Further up near the surface local shear production is smaller than local destruction of TKE and the deficit is supplied by the upward turbulent vertical diffusion of TKE from the boundary layer. This synoptic description and especially the importance of the vertical turbulent diffusion has been supported and complemented by observations from Shaw et al. (2001) and Stacey (2003) and numerical simulations from Li et al. (2010). A few studies have also explored the temporal variability of turbulent mixing. Among the most commonly observed feature is the ebb-flood vertical mixing asymmetry in presence of a longitudinal density gradient: observations from Rippeth et al. (2001) and Stacey and Ralston (2005) and numerical simulations from Simpson et al. (2002) reveal a cycle of increasing stratification and decreasing TKE in the surface layer during the ebb in contrast with increasing mixing during the flood further accelerated by convective mixing at the end of the flood.

Although the interactions of bottom-generated turbulence and density straining in partially-stratified estuaries have been the focus of most analyses, a growing number of studies have been reporting new mechanisms and interactions. Simpson et al. (1996) and Burchard et al. (1998) suggested that parametrization of internal waves should be included in turbulent closure schemes to better predict TKE dissipation rates in coastal seas. Stacey et al. (1999b) also suggested that internal waves might interact with the mean shear to trigger shear instabilities and increase local shear production during the decelerating phase of the tide in a partially-stratified estuary. The development of transverse circulations in regions of collocated transverse density and velocity gradients can also impact the turbulence dynamics: in a system with a complex geometry Lacy et al. (2003) observed increased density stratification at the end of the flood as a result of a density-driven lateral circulation; on the contrary, Farmer et al. (2002) observed turbulent mixing intensified by the density-driven tilting of the transverse shear in the wake of a headland. The shoal-channel interface in drowned-river estuaries is also a region where significant vertical and transverse density and

velocity gradients as well as transverse circulations can develop (Valle-Levinson et al. 2003; Cheng et al. 2009) but their effects on turbulence dynamics are still poorly characterized.

Horizontal mixing at the shoal-channel interface

At its core, the lateral structure of flow in a shoal-channel estuary resembles a shear layer. Early analyses of shear flows have focused on simplified problems such as the linear stability analysis of an inviscid and unstratified hyperbolic tangent profile by Michalke (1964). More recently, increasing computing resources have enabled scientists to address more realistic problems. For instance, the direct numerical simulation of an infinite stratified horizontal shear layer by Basak and Sarkar (2006) provides new insights in the dynamics of such complex flows. They found that in the case of a vertically stratified but horizontally sheared flow, an organized vorticity field emerges, characterized by the formation of dislocated lattices of vertical vortex cores. The persistence of vertical vortices is a consequence of the stratification suppressing horizontal vorticity. The size of the vortex columns is limited by stratification and well predicted by a simple balance between the centrifugal acceleration and the pressure gradient. In the wake of Basak and Sarkar (2006), Deloncle et al. (2007) investigated the linear stability of a stratified horizontal shear layer, especially the behavior of three-dimensional instabilities. Among others, these studies have shown that stratification stabilizes vertical shear but destabilizes horizontal shear flows, which suggests that in many cases a stratified shear flow is more sensitive to horizontal shear than vertical shear.

The shallow nature of shoal-channel estuaries means that bed friction will affect the dynamics of lateral shear layers. Linear stability analyses of shallow mixing layers by Van-Prooijen and Uijttewaal (2002) and Socolofsky and Jirka (2004) have shown that bed friction generally has a stabilizing effect. Ozkan-Haller and Kirby (1999) presented simulations and observations of shear instabilities generated by transverse shear of the along-shore current in the surf zone. They found in this case that transverse mixing due to the presence of these instabilities is dominant over other mixing mechanisms such as bottom-generated turbulence, and that the propagation speed of instabilities, the strength of the mean current, and the kinetic energy of the instabilities increase with decreasing bed friction.

A few approaches are traditionally used to quantify horizontal mixing in the ocean. Dye studies involve releasing dye as a point or line source and tracking the evolution of the spatial distribution of dye concentration. Clarke et al. (2007) fitted solutions of advection-diffusion equations to dye concentration profiles to estimate horizontal mixing coefficients in the surfzone. Assuming the dye dispersion to be governed by Fickian-like processes, horizontal diffusivities can be also inferred by taking the time derivative of the second moment of dye concentration profiles (Fong and Stacey 2003). Another common experimental method relies on GPS-tracked drifters. Dispersion coefficients can be estimated from various statistical methods reviewed by LaCasce (2008), such as single-particle Lagrangian statistics which were used by Spydell et al. (2009) to quantify surfzone dispersion. Banas et al. (2009) combined a numerical model of the Columbia river plume with Lagrangian particle tracking and found that the plume increases cross-shelf dispersion in the area.

Quantifying the lateral mixing coefficient at the shoal-channel interface is of fundamental importance for modeling plankton dynamics in estuaries. For instance Lucas et al. (2009) found that under conditions typical of early spring, a phytoplankton bloom occurs in the shoal but not in the channel in South San Francisco Bay if the lateral mixing across the shoal-channel interface is not included. However, if shoal-channel exchange is activated (by choosing a non-zero lateral diffusivity), a phytoplantkon bloom occurs both in the channel and in the shoal. This study highlights the pressing need for an insightful parametrization or model for transverse mixing at the shoal-channel interface.

1.2 South San Francisco Bay

South San Francisco Bay (SSFB) is defined as the Southern reach of San Francisco Bay (Figure 1.1), with a wetted surface area of approximately $550\,\mathrm{km}^2$ and an average depth of 3.4 m at mean lower low water (MLLW - the average of the lower low water height of each tidal day observed over the National Tidal Datum Epoch). The bathymetry in SSFB is characterized by a navigation channel of depth $h > 10\,\mathrm{m}$ and about 2000 m wide in the central region, flanked by broad shallow shoals (about 2-3 m deep).

Direct freshwater inflows in SSFB are dominated by waste water discharge ($1.3\,\mathrm{km}^3\,\mathrm{year}^{-1}$) with only $0.1\,\mathrm{km}^3\,\mathrm{year}^{-1}$ coming from local tributaries (Cheng and Gartner 1985), although most of the river inflow occurs during the winter months (typically November-April). Typical meteorological conditions in SSFB are characterized by prevailing westerly or north-westerly winds from late spring through early fall, reinforced in the summer by a sea breeze resulting from solar heating inland. In the winter, winds are more variable but frequently influenced by storm systems to the South driving easterly or south-easterly winds locally.

At a given location, the evolution of the free surface elevation $\eta(t)$ due to tides can be decomposed as a sum of tidal harmonic constituents:

$$\eta(t) = \eta_0 + \sum_i \eta_i \cos(\omega_i t + \phi_i) \tag{1.14}$$

where η_0 is the mean water level and η_i, ω_i and ϕ_i are the amplitude, pulsation and phase of the i-th tidal constituent. In SSFB, tides are dominated by the semi-diurnal M2 and diurnal K1 constituents (Table 1.1). The M2 tide behaves closely to a standing wave (approximately 1 hour lag between free surface elevation η and currents local acceleration $\partial u/\partial t$) and is amplified by a factor of about 1.5 between the Northern and Southern end of SSFB (Cheng and Gartner 1985). This amplification is a consequence of the specific geometry of SSFB and its impact on tidal propagation.

1.3 Research Questions

Our limited understanding of intratidal transport and mixing processes at the shoal-channel interface in a partially-stratified estuary motivated this work. Using field observations de-

scribed in chapter 2, the following questions are addressed.

Question 1: What processes control the transverse flow at the shoal-channel interface?

A lateral circulation usually develops during each tide in regions of sloping bathymetry, but it can be driven by various mechanisms such as lateral density gradients, Earth's rotation, or lateral variations in vertical mixing for instance. The objectives of chapter 3 are to identify which of these processes drive the lateral circulation at the shoal-channel interface in SSFB, characterize their evolution throughout a tidal cycle and assess their sensitivity to changes in tidal amplitude and stratification.

Question 2: What are the interactions between the longitudinal flow, the transverse circulation and turbulence dynamics at the shoal-channel interface?

On the shoal, tidal flows are characterized by a bottom boundary layer extending all the way to the surface. In the channel, the boundary layer is usually capped by a stable pycnocline, except in the later part of the flood when it might also extend to the surface. However on the slope, the vertical structure of turbulent quantities is not as well characterized because the interactions between the lateral circulation and the longitudinal flow and their impacts on turbulence dynamics are still poorly understood. The objective of chapter 4 is to assess how turbulence dynamics on the slope differ from the dynamics in the channel and on the shoals by identifying these interactions and their impacts.

Question 3: What processes drive lateral mixing at the shoal-channel interface, and how important are they for long-term dispersion?

Lateral mixing at the shoal-channel interface can result from various intratidal processes, such as vertical shear in the bottom boundary layer, lateral shear between the channel and shoal, or shear dispersion associated with the lateral circulation, although their relative importance is unknown. The objective of chapter 5 is to estimate the relevant mixing coefficients associated with these different processes.

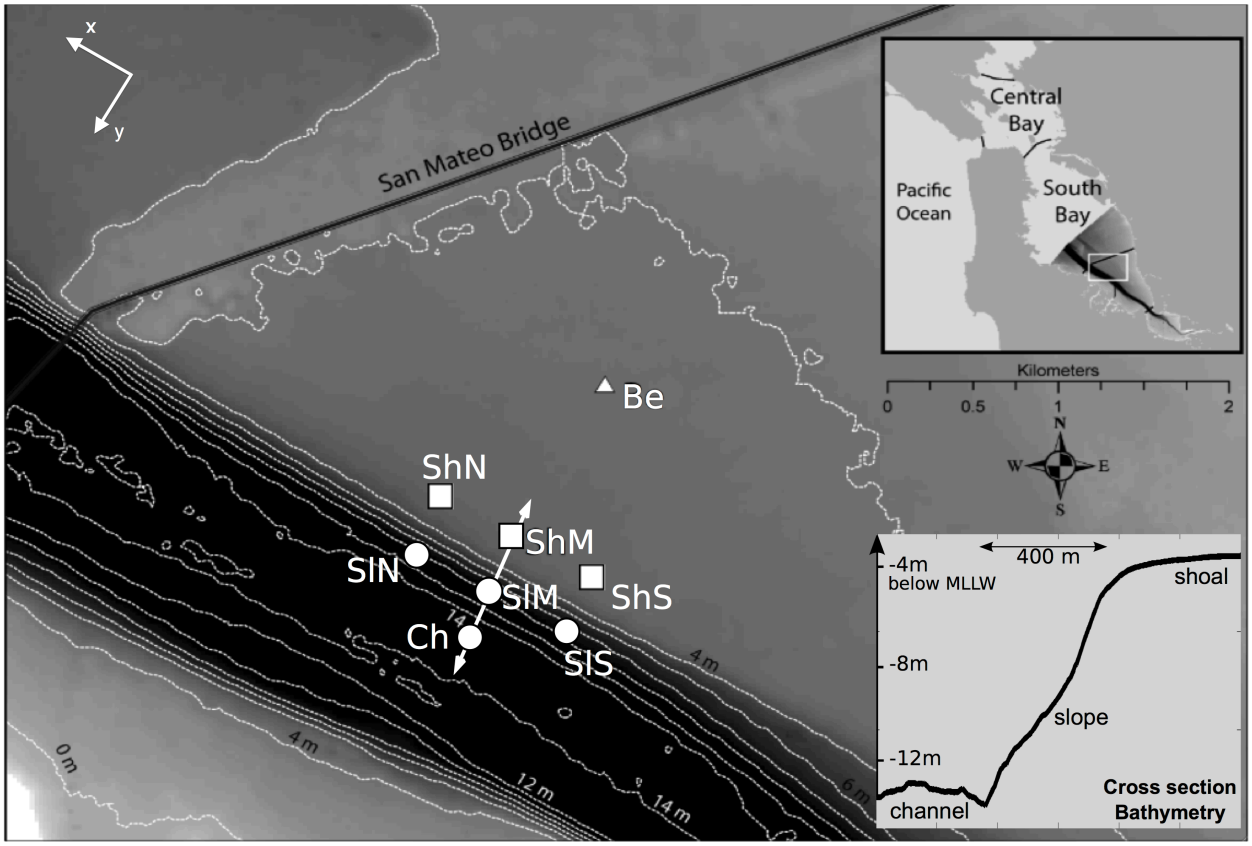

Figure 1.1: Map of the field site in South San Francisco Bay: location of the moorings (white disks, squares and triangle) and transect path (double arrow). Contours represent the isobaths, defined as the distance of the bed below MLLW. The lower right insert displays the bathymetry profile along the transect path.

Table 1.1: Typical periods and amplitudes of the five dominant tidal harmonic constituents in South San Francisco Bay (Cheng and Gartner 1985).

Tidal harmonics	Period $2\pi/\omega_i$	Amplitude η_i
M2	12.42 hours	$57.8 - 90.8$ cm
K1	23.93 hours	$36.7 - 40.6$ cm
O1	25.82 hours	$22.0 - 24.0$ cm
S2	12.00 hours	$13.5 - 23.1$ cm
N2	12.66 hours	$9.6 - 18.6$ cm

Chapter 2

Experimental Design

This research is based on data collected during two identical experiments conducted in 2009, in collaboration with Dr. Jessie Lacy and the staff from the US Geological Survey's Pacific Coastal and Marine Science Center in Santa Cruz, CA. These experiments were designed to address three research questions:

1. what is the dominant exchange mechanism between water masses with differential fraction (e.g. channel and shoal) and what is the resulting timing and magnitude of this mechanism?

2. how do sediment resuspension, active layer depth and bed particle size distribution vary with depth, wind forcing, fetch, spring-neap and annual cycles?

3. how do the dynamics of shoal-channel exchange influence estuarine dynamics and sediment transport at the scale of the estuary?

As outlined in Chapter 1, my contribution focuses on the first of these three research questions and relies on velocity and salinity measurements from the winter experiment, during which South San Francisco Bay was partially stratified. To address this question, the two experiments were designed to meet the following scientific requirements:

1. capture variability over a broad range of timescales, from turbulent fluctuations ($<$ 100 s) to neap-spring (14 days) and seasonal cycles (6 months).

2. capture vertical variability from the largest turbulent lengthscales ($\sim 0.5 - 1$ m) to the water depth ($\sim 3 - 15$ m).

3. capture horizontal variability over lengthscales relevant to the shoal-channel interface (~ 500 m in the streamwise x-direction and $\sim 50 - 500$ m in the transverse y-direction).

Tidal and meteorological conditions during the two experiments are described in sections 2.1 and 2.2. Velocity and salinity measurements and sampling strategies are described in

details in section 2.3, along with a brief description of the other measurements for completeness. Pre-processing of raw measurements is described in section 2.4. Section 2.5 summarizes the chapter.

2.1 Winter 2009 Experiment

The winter 2009 experiment took place between day 54 (February 24th) and 74 (March 16th). This period was chosen because it corresponds to the rainy season in California, and freshwater inflows in San Francisco Bay are maximal. It is therefore the best time of the year to study the effects of stratification on estuarine dynamics. During this period, the main meteorological event was a two day storm which spanned from day 60 to 61. This storm generated precipitation between 30 mm and 40 mm in the area and discharge peaks in the streams flowing into South San Francisco Bay (Figure 2.1e). The dominant wind direction during the storm was from the South. The beginning and end periods of the experiment were characterized by symmetrical tidal cycles dominated by the semi-diurnal constituent (Figure 2.1a):

- large range: $2 - 2.5\,\mathrm{m}$
- ebb and flood tides are approximately symmetrical

while the middle of the experiment was characterized by asymmetrical tidal cycles dominated by both semi-diurnal and diurnal constituents:

- first ebb has a small range: $0.5 - 1\,\mathrm{m}$
- first flood has a medium range: $1 - 1.5\,\mathrm{m}$
- second ebb has a large range: $2 - 2.5\,\mathrm{m}$
- second flood has a medium range: $1 - 1.5\,\mathrm{m}$

the asymmetry being most pronounced on day 62 (Figure 2.1a). From this point, we'll refer to the symmetrical tidal cycles as spring tides and to the asymmetrical tidal cycles as neap tides. Three transect surveys were conducted during this experiment:

1. the first survey took place from day 57.65 to day 58.1 and spanned over a flood tide and halfway through the following ebb (Figure 2.2a). The flood sampled had a 1.9 m range and the ebb had a 2 m range. Nineteen transects were conducted during this survey. The wind was weak ($0 - 4\,\mathrm{m\,s^{-1}}$) and predominantly from the NW (Figure 2.2d,g).
2. the second survey took place from day 63.7 to day 64.1 and spanned over half an ebb and halfway through the successive flood (Figure 2.2b). The ebb sampled had a 2.3 m range and the flood had a 1.9 m range. Eighteen transects were conducted during this

survey. The wind was weak ($0 - 6\,\mathrm{m\,s^{-1}}$) predominantly from the SE during the first seven transects and from the NW afterwards (Figure 2.2e,h).

3. the third survey took place between day 67.7 and 68.05 and spanned over the end of a flood and through the successive ebb (Figure 2.2c). The sampled ebb had a 2.8 m range. Fifteen transects were conducted during this survey. The wind was strong ($4 - 8\,\mathrm{m\,s^{-1}}$) and from the NW (Figure 2.2f,i).

Datasets collected during the first and second transect surveys were the most used in this work because they captured the system shortly before and after the main rainstorm (days 60-61) and therefore revealed the sensitivity of the system to an increase in density stratification associated with the peak freshwater inflows in South San Francisco Bay.

2.2 Summer 2009 Experiment

The second deployment took place during summer 2009 between day 251 (September 9th) and day 272 (September 30th). This period corresponds to the dry season in California, and freshwater inflows in San Francisco Bay were minimal (Figure 2.1f). It is therefore an appropriate time to study the estuarine dynamics with minimized stratification effects. This period of the year is also characterized by consistent afternoon sea breezes from the NW in South San Francisco Bay (Figure 2.1d). The beginning and end periods of the summer experiment were characterized by asymmetrical neap tidal cycles while the middle period was characterized by symmetrical spring tidal cycles (Figure 2.1b) similar to those described in section 2.1. Three transect surveys were conducted during this experiment:

1. the first survey took place from day 253.65 to day 254.05 and spanned over the end of an ebb tide and through the following flood (Figure 2.3a). The ebb sampled had a 0.7 m range and the flood had a 1.3 m range. Sixteen transects were conducted during this survey. The wind was weak ($0 - 4\,\mathrm{m\,s^{-1}}$) and predominantly from the NW (Figure 2.3d,g).

2. the second survey took place from day 257.65 to day 258 and spanned over the end of a flood and through the successive ebb (Figure 2.3b). The ebb sampled had a 1.5 m range. Fifteen transects were conducted during this survey. The wind was weak during the first four transects ($0 - 3\,\mathrm{m\,s^{-1}}$) but increased to $5 - 8\,\mathrm{m\,s^{-1}}$ from the NW as the sea-breeze developed (Figure 2.3e,h).

3. the third survey took place between day 260.65 and 261.05 and spanned over the later half of a flood and through most of the successive ebb (Figure 2.3c). The sampled flood had a 1.6 m range and the ebb had a 1.4 m range. Sixteen transects were conducted during this survey. The wind was weak during the first eight transects ($0 - 2\,\mathrm{m\,s^{-1}}$) but increased to $4 - 6\,\mathrm{m\,s^{-1}}$ from the NW as the sea-breeze developed (Figure 2.3f,i).

2.3 Instruments and Sampling

Measurements of currents velocities, water temperature, salinity and turbidity were made at eight different locations across and along the shoal-channel interface in South San Francisco Bay (Figure 1.1): one mooring was located in the channel, three on the slope, three on the shoal near the slope and one on the shoal further away from the slope. In addition to these point-measurements, transect surveys were conducted across the shoal-channel interface to capture simultaneously the temporal and cross-sectional variability of these same variables. Conductivity measurements are converted directly by the instruments to salinity expressed in practical salinity units (1 psu $\simeq$ 1 g salt/1 kg seawater). Optical backscatter measurements are converted directly by the instruments to turbidity expressed in Nephelometric Turbidity Unit (NTU).

The channel mooring was deployed about 200 m away from the slope at a mean-low depth of about 15 m (Figure 1.1, labeled ch). The instruments on this mooring are described in Table 2.3. The North, Mid and South slope moorings were deployed halfway up the slope at a mean-low depth of about 8.5 m (Figure 1.1, labeled SlN, SlM and SlS). The instruments on these moorings are described in Table 2.4-2.6. The North, Mid and South shoal moorings were deployed about 200 m away from the slope at a mean-low depth of about 3.5 m (Figure 1.1, labeled ShN, ShM and ShS). The instruments on these moorings are described in Table 2.7-2.10. The benthic mooring was deployed on the shoal, about 1 km North-East from the ShM mooring (Figure 1.1, labeled Be). The instruments on the Benthic mooring are described in Table 2.11-2.12.

The transects, which extended from at least 200 m into the channel, over the slope and about 400 m onto the shoals, were between 1000 m and 1200 m long (Figure 1.1) and repeated approximately every 30 minutes. One way was dedicated to velocity measurements with a downward-facing, boat-mounted Acoustic Doppler Current Profiler (Table 2.13). The return was dedicated to five vertical profiles of salinity, temperature, and turbidity, equally spaced along the transect path with a conductivity/temperature/depth/turbidity sensor (Table 2.13). The first one was over the shoal about 200 m from the edge, the second was at the edge of the shoal, the third was at the middle of the slope, the fourth was at the edge of the channel and the last one was over the channel about 200 m from the slope.

The missing parts of this dataset and associated failures are described in Table 2.14. The measurement uncertainties are listed in Tables 2.3-2.13 for each instrument.

2.4 Data processing

To compare measurements by different instruments, a general coordinate system (x, y, z, t) is defined as follow:

- time t is expressed in days, with $t = 0$ being 0000 UTC 1 January 2009 and $t = 63.5$ being 1200 UTC 5 March 2009.

- the coordinate x is defined as the along-isobath coordinate (Figure 1.1), positive in the North-West direction (also ebb direction). The velocity component in this direction is u. The origin $x = 0$ is defined at the location of the channel mooring (note that the SlM and ShM are also on the $x = 0$ line).

- the coordinate y is defined as the across-isobath coordinate (Figure 1.1), perpendicular to the x-axis and positive in the South-West direction. The velocity component in this direction is v. The origin $y = 0$ is defined at the edge of the channel, at the lower end of the slope.

- the vertical coordinate z is defined positive upward. The vertical velocity component is w. The origin $z = 0$ is defined as the bed elevation, at the location of the channel mooring.

The horizontal velocity data measured by the Acoustic Doppler Current Profilers (ADCPs) at the channel and slope moorings was decomposed in principal components $(\tilde{u}, \tilde{v})$, $\tilde{u}$ being velocity in the direction $\tilde{x}$ of maximal variance of the depth-averaged velocity and $\tilde{v}$ the velocity in the direction $\tilde{y}$ perpendicular to the $\tilde{x}$-axis and positive in the South-West direction. The angle between the along-isobath direction x and the direction of maximal variance $\tilde{x}$ was about 2° at the slope moorings and about 5° at the channel mooring. Those values are smaller than the uncertainty of the ADCPs compass measurements, such that we assume $(x, y) = (\tilde{x}, \tilde{y})$ and $(u, v) = (\tilde{u}, \tilde{v})$. The horizontal velocity data measured at the shoal and benthic moorings and during the transect surveys were rotated from (North, East, Vertical) components to along/across-isobath/vertical components (u, v, w).

The vertical conductivity/salinity/temperature/turbidity/pressure profiles collected during the transect surveys were interpolated on the same (y, z) grid as the transect velocity measurements to get cross-sectional distributions of salinity, temperature and turbidity. A cubic interpolation method was used to ensure continuity of the scalar fields and their vertical and lateral derivatives.

Water density ρ depends on pressure p, temperature T and salinity s as defined by the equation of state $\rho = \rho(s, T, p)$. For simplicity, the linearized version of the equation of state (Vallis 2006) is used here:

$$\rho = \rho_0 \left[1 - \alpha(T - T_0) + \beta(s - s_0) - \gamma(p - p_0)\right] \tag{2.1}$$

where $\rho_0 = 1028\,\mathrm{kg\,m^{-3}}$ is the density of seawater at $p_0 = 1.01\,10^5\,\mathrm{Pa}$, $T_0 = 283\,\mathrm{K}$, $s_0 = 35\,\mathrm{psu}$ and $\alpha = 1.7\,10^{-4}\,\mathrm{K^{-1}}$ is the coefficient of thermal expansion, $\beta = 7.6\,10^{-4}\,\mathrm{psu^{-1}}$ is the coefficient of saline contraction and $\gamma = 4.1\,10^{-10}\,\mathrm{Pa}$ is the coefficient of compressibility. The error associated with the linearized expression (2.1) is less than $0.03\,\mathrm{kg\,m^{-3}}$ for the 98% range of values in the ocean (Gill 1982), which includes temperature and salinity values in South San Francisco Bay. In most shoal-channel estuaries including South San Francisco Bay, density variations are typically dominated by salinity and variations in temperature and pressure are not dynamically important. In the case of South San Francisco Bay, the pressure

contribution to density $\gamma(p - p_0) = \mathrm{O}(10^{-5})$ is much smaller than the the contribution of temperature $\alpha(T - T_0) = \mathrm{O}(10^{-4})$ and salinity $\beta(s - s_0) = \mathrm{O}(10^{-4} - 10^{-3})$ because the depth does not exceed 15 m. As a result, compressibility effects are neglected and a simplified equation of state is used in this work :

$$\rho = \rho_0 \left[1 - \alpha(T - T_0) + \beta(s - s_0)\right] \tag{2.2}$$

2.5 Summary

The dataset used for this work was collected during two identical interdisciplinary experiments in February-March and September-October 2009 in South San Francisco Bay. Each experiment involved moored instruments and transect surveys to measure currents velocities and water properties such as conductivity (from which was inferred salinity), temperature, pressure and turbidity (from which was inferred suspended sediment concentrations). The analyses presented in the following chapters are based exclusively on velocity, temperature and salinity measurements at the channel, slope and shoal moorings and from the transect surveys.

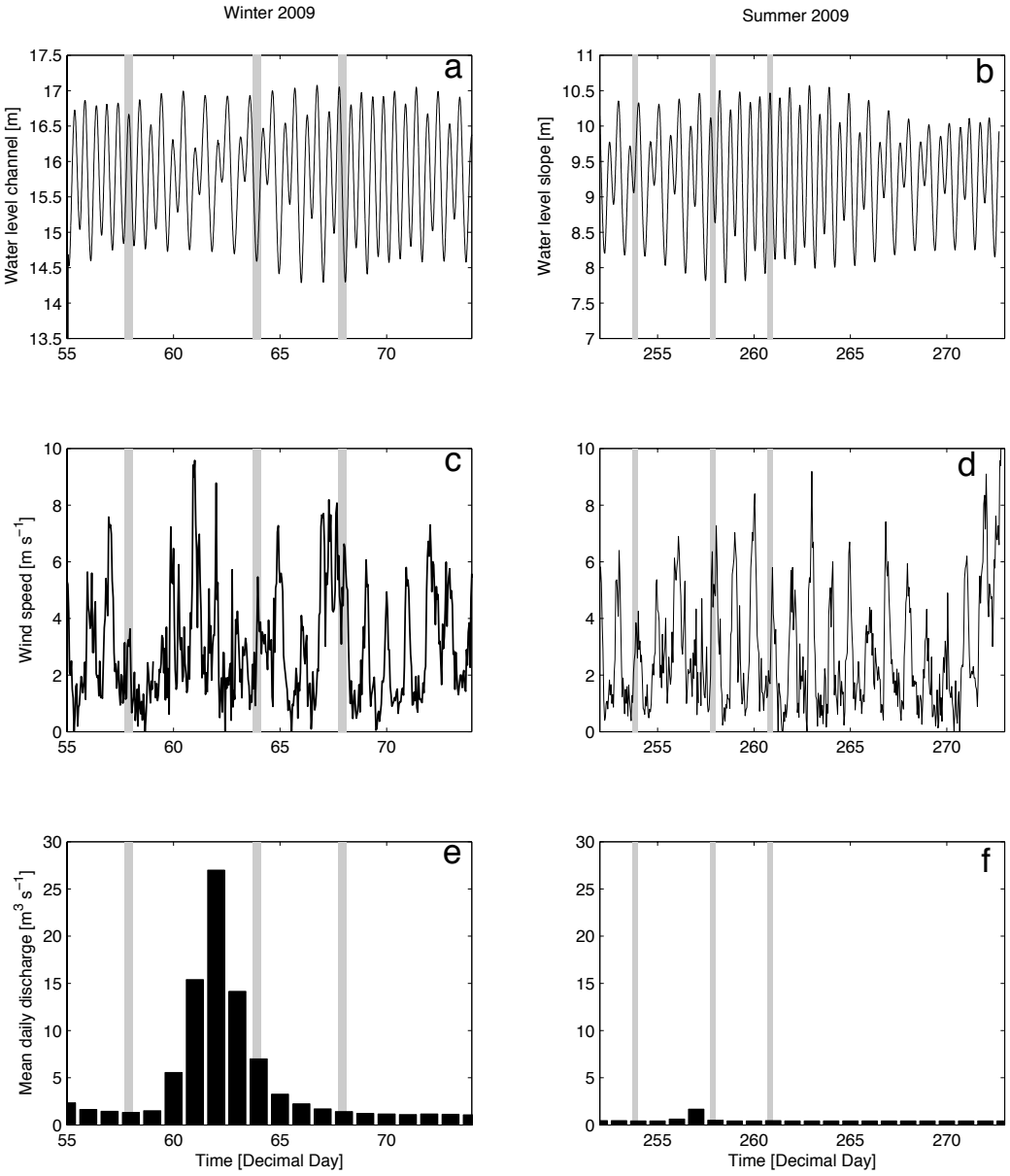

Figure 2.1: Tidal and meteorological conditions in South San Francisco Bay during the two deployments: water level (a: winter - b: summer), wind speed from NOAA's Redwood City station (c: winter - d: summer), and mean daily discharge of Guadalupe river in South San Francisco Bay from USGS (e: winter - f: summer). Shaded areas represent the dates of the transect surveys.

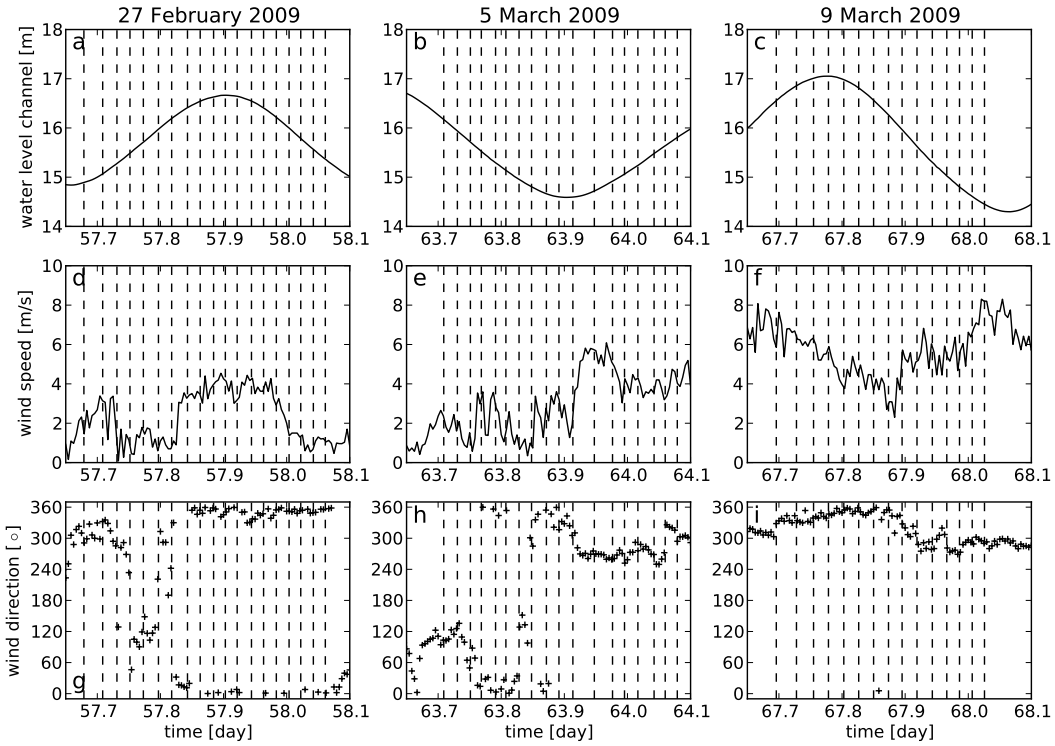

Figure 2.2: Tidal and meteorological conditions in South San Francisco Bay during the three winter transect surveys: water level in the channel (a, b, c), wind speed (d, e, f) and wind direction from NOAA's Redwood City station (g, h, i). The dashed lines represent the starting date of individual transects.

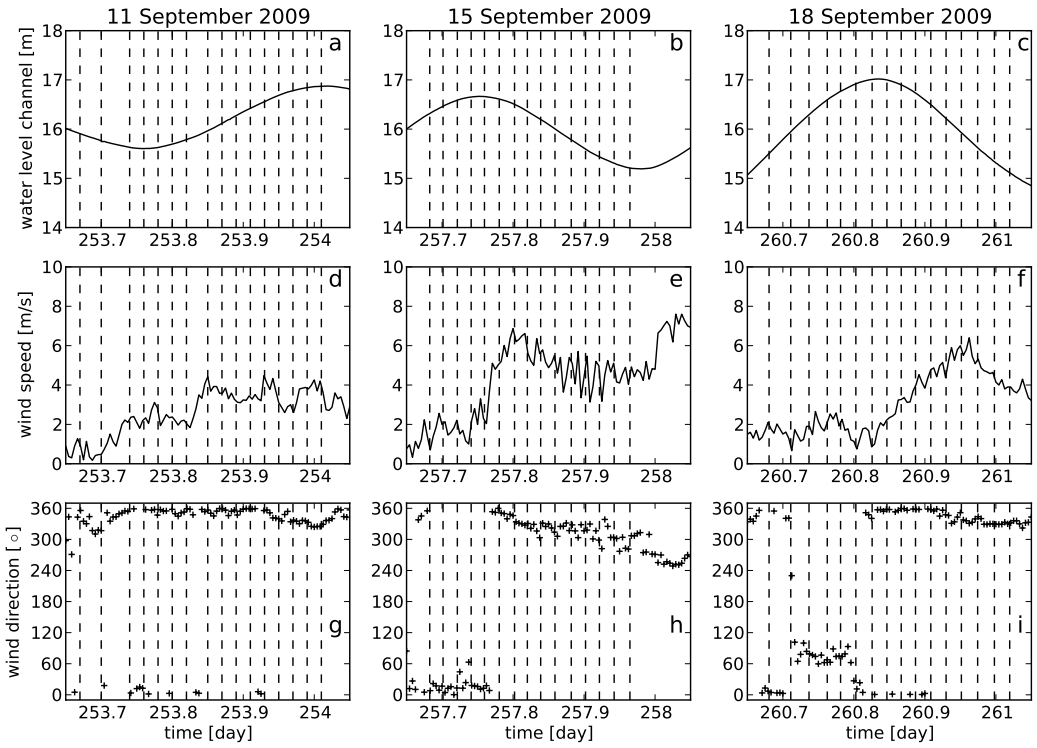

Figure 2.3: Tidal and meteorological conditions in South San Francisco Bay during the three summer transect surveys: water level in the channel (a, b, c), wind speed (d, e, f) and wind direction from NOAA's Redwood City station (g, h, i). The dashed lines represent the starting date of individual transects.

Table 2.1: Winter 2009 deployment and transect surveys: summary

	Day Start	Day End	Tides	Atmospheric Forcing
Moorings	54	74	spring-neap-spring	rainstorm (days 60-61)
Transect survey 1	57.65	58.1	flood-ebb	weak wind ($< 5\,\mathrm{m\,s^{-1}}$)
Transect survey 2	63.7	64.1	ebb-flood	weak wind ($< 5\,\mathrm{m\,s^{-1}}$)
Transect survey 3	67.7	68.05	ebb	NW wind ($5 - 8\,\mathrm{m\,s^{-1}}$)

Table 2.2: Summer 2009 deployment and transect surveys: summary

	Day Start	Day End	Tides	Atmospheric Forcing
Moorings	251	272	neap-spring-neap	daily NW winds ($5-9\,\mathrm{m\,s^{-1}}$)
Transect survey 1	253.65	254.05	ebb-flood	weak wind ($<5\,\mathrm{m\,s^{-1}}$)
Transect survey 2	257.65	258	ebb	NW wind ($5-8\,\mathrm{m\,s^{-1}}$)
Transect survey 3	260.65	261.05	flood-ebb	NW wind ($5-6\,\mathrm{m\,s^{-1}}$)

Table 2.3: Instruments at the channel mooring.

Instrument	Location	Manufacturer/Model	Sampling	Uncertainty	Vertical profiles
600 kHz ADCP[a]	0.4 m a.b.[b]	Teledyne RDI Workhorse Monitor	1 Hz	$\epsilon = \pm 6.95\,\mathrm{cm\,s^{-1}}$	number of bins: 40 bin size: 0.5 m lowest bin: 1.88 m a.b.
CTD[c]	0.4 m a.b.	RBR XR-420	every 6 min	$\epsilon_T = \pm 0.002^\circ$ C $\epsilon_S = \pm 0.0025$ psu	
CTD	2 m b.s.[d]	RBR XR-420	every 3 min	$\epsilon_T = \pm 0.002^\circ$ C $\epsilon_S = \pm 0.0025$ psu	
OBS[e]	0.4 m a.b.	D&A Instruments	every 6 min	unknown	
OBS	2 m b.s.	D&A Instruments	every 3 min	unknown	

[a] Acoustic Doppler Current Profiler
[b] meters above bed
[c] Conductivity Temperature Depth sensor
[d] meters below surface
[e] Optical Backscatter sensor

Table 2.4: Instruments at the slope North (SlN) mooring.

Instrument	Location	Manufacturer/Model	Sampling	Uncertainty	Vertical profiles
1200 kHz ADCP[a]	0.2 m a.b.[b]	Teledyne RDI Workhorse Sentinel	1 Hz	$\epsilon = \pm 13.64\,\mathrm{cm\,s^{-1}}$	number of bins: 48 bin size: 0.25 m lowest bin: 0.86 m a.b.
CTD[c]	0.5 m a.b.	RBR XR-620	every 3 min	$\epsilon_T = \pm 0.002^\circ$ C $\epsilon_S = \pm 0.0025$ psu	
OBS[d]	0.18 m a.b.	Seapoint	every 3 min	$\lvert\epsilon\rvert < 0.1$ NTU	
CTD	1 m b.s. [e]	RBR	every 6 min	$\epsilon_T = \pm 0.002^\circ$ C $\epsilon_S = \pm 0.0025$ psu	
OBS	1 m b.s.	D&A Instruments	every 6 min	unknown	

[a] Acoustic Doppler Current Profiler
[b] meters above bed
[c] Conductivity Temperature Depth sensor
[d] Optical Backscatter sensor
[e] meters below surface

Table 2.5: Instruments at the slope Mid (SlM) mooring.

Instrument	Location	Manufacturer/Model	Sampling	Uncertainty	Vertical profiles
1200 kHz ADCP[a]	0.72 m a.b.[b]	Teledyne RDI Workhorse Sentinel	1 Hz	$\epsilon = \pm 13.64\,\mathrm{cm\,s^{-1}}$	number of bins: 48 bin size: 0.25 m lowest bin: 1.48 m a.b.
CTD[c]	0.54 m a.b.	RBR	every 6 min	$\epsilon_T = \pm 0.002^\circ$ C $\epsilon_S = \pm 0.0025$ psu	
CT[d]	0.72 m a.b.	Seabird Electronics Seacat	every 3 min	$\epsilon_T = \pm 0.005^\circ$ C $\epsilon_S = \pm 0.004$ psu	
OBS[e]	0.43 m a.b.	Seapoint	every 3 min	$\lvert\epsilon\rvert < 0.1$ NTU	
CTD	3 m b.s. [f]	RBR XR-420	every 3 min	$\epsilon_T = \pm 0.002^\circ$ C $\epsilon_S = \pm 0.0025$ psu	
OBS	3 m b.s.	D&A Instruments	every 3 min	unknown	
CTD	0.6 m b.s.	RBR XR-420	every 6 min	$\epsilon_T = \pm 0.002^\circ$ C $\epsilon_S = \pm 0.0025$ psu	
OBS	0.6 m b.s.	D&A Instruments	every 6 min	unknown	

[a] Acoustic Doppler Current Profiler
[b] meters above bed
[c] Conductivity Temperature Depth sensor
[d] Conductivity Temperature sensor
[e] Optical Backscatter sensor
[f] meters below surface

Table 2.6: Instruments at the slope South (SlS) mooring.

Instrument	Location	Manufacturer/Model	Sampling	Uncertainty	Vertical profiles
1200 kHz ADCP[a]	0.45 m a.b.[b]	Teledyne RDI Workhorse Monitor	1 Hz	$\epsilon = \pm 13.64\,\mathrm{cm\,s^{-1}}$	number of bins: 48 bin size: 0.25 m lowest bin: 1.21 m a.b.
CTD[c]	1 m b.s. [d]	RBR XR-420	every 6 min	$\epsilon_T = \pm 0.002^\circ$ C $\epsilon_S = \pm 0.0025$ psu	
OBS[e]	1 m b.s.	D&A Instruments	every 6 min	unknown	

[a] Acoustic Doppler Current Profiler
[b] meters above bed
[c] Conductivity Temperature Depth sensor
[d] meters below surface
[e] Optical Backscatter sensor

Table 2.7: Instruments at the shoal North (ShN) mooring.

Instrument	Location	Manufacturer/Model	Sampling	Uncertainty	Vertical profiles
PCADP[a]	1.61 m a.b.[b]	Sontek	10 min bursts at 1 Hz every 12 min	unknown	number of bins: 15 bin size: 9.4 cm lowest bin: 1.98 m a.b.
ADV[c]	0.52 m a.b.	Sontek / Hydra	8 min bursts at 4 Hz every 12 min	$\epsilon = \pm 1\% \pm 0.5\,\mathrm{cm\,s^{-1}}$	
CT[d]	0.72 m a.b. (C) 0.65 m a.b. (T)	Seabird Electronics Microcat	every 12 min	$\epsilon_T = \pm 0.002^\circ$ C $\epsilon_S = \pm 0.0025$ psu	
OBS[e]	0.5 m a.b.	D&A Instruments	every 12 min	unknown	
Pressure	1.38 m a.b.	ParoScientific	every 12 min	$\epsilon = \pm 0.01\%$	
Pressure	1.24 m a.b.	ParoScientific	every 12 min	$\epsilon = \pm 0.01\%$	

[a] Pulse Coherent Acoustic Doppler Profiler
[b] meters above bed
[c] Acoustic Doppler Velocimeter
[d] Conductivity Temperature sensor
[e] Optical Backscatter sensor

Table 2.8: Instruments at the shoal Mid (ShM) mooring.

Instrument	Location	Manufacturer/Model	Sampling	Uncertainty	Vertical profiles
PCADP[a]	1.61 m a.b.[b]	Sontek	10 min bursts at 1 Hz every 12 min	unknown	number of bins: 15 bin size: 9.4 cm lowest bin: 1.98 m a.b.
ADV[c]	0.36 m a.b.	Sontek / Hydra	10 min bursts at 8 Hz every 60 min	$\epsilon = \pm 1\% \pm 0.5\,\mathrm{cm\,s^{-1}}$	
ADV	0.7 m a.b.	Nortek / Vector	10 min bursts at 8 Hz every 60 min	$\epsilon = \pm 0.5\% \pm 0.1\,\mathrm{cm\,s^{-1}}$	

[a] Pulse Coherent Acoustic Doppler Profiler
[b] meters above bed
[c] Acoustic Doppler Velocimeter

Table 2.9: Instruments at the shoal Mid (ShM) mooring (continued).

Instrument	Location	Manufacturer/Model	Sampling	Uncertainty	Vertical profiles
CTD[a]	1.66 m a.b.	Seabird Electronics Microcat	every 3 min	$\epsilon_T = \pm 0.002°$ C $\epsilon_S = \pm 0.0025$ psu	
CTD	0.47 m a.b.	RBR XR-420	every 3 min	$\epsilon_T = \pm 0.002°$ C $\epsilon_S = \pm 0.0025$ psu	
OBS[b]	0.26 m a.b.	D&A Instruments	every 3 min	unknown	
OBS	0.72 m a.b.	D&A Instruments	every 3 min	unknown	
OBS	0.47 m a.b.	D&A Instruments	every 3 min	unknown	
Pressure	1.4 m a.b.	ParoScientific	every 3 min	$\epsilon = \pm 0.01\%$	

[a] Conductivity Temperature Depth sensor
[b] Optical Backscatter sensor

Table 2.10: Instruments at the shoal South (ShS) mooring.

Instrument	Location	Manufacturer/Model	Sampling	Uncertainty	Vertical profiles
ADV[a]	0.25 m a.b.	Sontek / Hydra	10 min bursts at 8 Hz every 60 min	$\epsilon = \pm 1\% \pm 0.5\,\mathrm{cm\,s^{-1}}$	
ADV	0.5 m a.b.	Nortek / Vector	10 min bursts at 8 Hz every 60 min	$\epsilon = \pm 0.5\% \pm 0.1\,\mathrm{cm\,s^{-1}}$	
CTD[b]	0.5 m a.b.	Seabird Electronics Microcat	every 12 min	$\epsilon_T = \pm 0.002^\circ$ C $\epsilon_S = \pm 0.0025$ psu	
OBS[c]	0.5 m a.b.	D&A Instruments	every 12 min	unknown	

[a]Acoustic Doppler Velocimeter
[b]Conductivity Temperature Depth sensor
[c]Optical Backscatter sensor

Table 2.11: Instruments at the benthic (Be) mooring.

Instrument	Location	Manufacturer/Model	Sampling	Uncertainty	Vertical profiles
ADV[a]	0.72 m a.b.[b]	Sontek / Hydra	8 min bursts at 10 Hz every 12 min	$\epsilon = \pm 1\% \pm 0.5\,\mathrm{cm\,s^{-1}}$	
ADV	0.36 m a.b.	Sontek / Hydra	8 min bursts at 10 Hz every 12 min	$\epsilon = \pm 1\% \pm 0.5\,\mathrm{cm\,s^{-1}}$	
LISST[c]	0.55 m a.b.	Sequoia Scientific 100 Type B	2 min bursts at 1 Hz every 12 min	unknown	
Imaging sonar	0.3 m a.b.	Imagenex	3×4 min scans every hour 2×10 min scans every 6 hours	unknown	
Profiling sonar	1.5 m a.b.	Imagenex	3×4 min scans every hour	unknown	

[a] Acoustic Doppler Velocimeter
[b] meters above bed
[c] Laser In-Situ Scattering and Transmissometry sensor

Table 2.12: Instruments at the benthic (Be) mooring (continued).

Instrument	Location	Manufacturer/Model	Sampling	Uncertainty	Vertical profiles
OBS[a]	0.36 m a.b.[b]	D&A Instruments	every 12 min	unknown	
OBS[c]	0.72 m a.b.	D&A Instruments	every 12 min	unknown	
CTD[d]	1.58 m a.b.	Seabird Electronics Seacat	every 3 min	$\epsilon_T = \pm 0.005°$ C $\epsilon_S = \pm 0.004$ psu	
CT[e]	0.73 m a.b.	Seabird Electronics Microcat	every 12 min	$\epsilon_T = \pm 0.002°$ C $\epsilon_S = \pm 0.0025$ psu	

[a]Optical Backscatter sensor
[b]meters above bed
[c]Optical Backscatter sensor
[d]Conductivity Temperature Depth sensor
[e]Conductivity Temperature sensor

Table 2.13: Instruments used during the transect surveys.

Instrument	Location	Manufacturer/Model	Sampling	Uncertainty	Vertical profiles
1200 kHz ADCP[a]	0.5 m b.s. [b]	Teledyne RDI Workhorse Monitor	1 Hz or 0.12 Hz [c]	$\epsilon = \pm 7.68\,\mathrm{cm\,s^{-1}}$ or $\epsilon = \pm 6.27\,\mathrm{cm\,s^{-1}}$	number of bins: 79 bin size: 0.25 m highest bin: 1.2 m b.s.
CTD[d]		Seabird Electronics Seacat Profiler	4 Hz	$\epsilon_T = \pm 0.005°$ C $\epsilon_S = \pm 0.004$ psu	

[a] Acoustic Doppler Current Profiler
[b] meters below surface
[c] used in wavy condition
[d] Conductivity Temperature Depth sensor

Table 2.14: Missing data and associated failures.

Instrument	Location	Manufacturer/Model	Missing period	Failure
600 kHz ADCP	Ch	Teledyne RDI Workhorse Monitor	winter experiment day 64.22 to 74	instrument's electronics
1200 kHz ADCP	SlN	Teledyne RDI Workhorse Sentinel	winter experiment day 54 to 60.16	unknown
1200 kHz ADCP	SlM	Teledyne RDI Workhorse Sentinel	winter experiment day 64.56 to 74	unknown
1200 kHz ADCP	SlS	Teledyne RDI Workhorse Monitor	winter experiment day 54 to 74	unknown
ADV	ShM 0.36 m a.b.	Sontek Hydra	winter experiment day 54 to 74	unknown
CTD	Transect survey 3	Seabird Electronics Seacat Profiler	winter experiment day 67.7 to 68.05	battery
CTD	Ch 2 m b.s.	RBR XR-420	summer experiment day 251 to 272	instrument lost
LISST	Be	Sequoia Scientific 100 Type B	winter experiment day 69 to 74	biofouling
			summer experiment day 256 to 272	biofouling

Chapter 3

Lateral Circulation and Fronts

This chapter addresses the first research question described in section 1.3. The processes controlling the lateral circulation dynamics are identified and compared using the observations. The intratidal variations of the lateral circulation are the main focus of this chapter, although the sensitivity to subtidal changes in tidal amplitude (neap-spring cycle) and stratification (changes in river discharge) is briefly discussed at the end.

3.1 Observations

The work presented here is based mostly on the data from the 5 March 2009 transect survey, which showed the strongest density gradients and lateral circulation of all the transect surveys as a result of the 2/3 March 2009 storm. On that day, seventeen transects were performed between 0900 PST and 1800 PST (between decimal days 63.7 and 64.1). The first transect was conducted early in the ebb, about two hours and forty minutes after high water and the last transect was conducted midway in the successive flood, about three hours and twenty minutes before the following high water (Figure 2.2b). The sampled ebb had a 2.5 m amplitude and spanned over seven hours eighteen minutes between higher high and lower low waters. The successive flood had a 2 m amplitude and spanned over seven hours thirty-six minutes between lower low and lower high waters. The wind direction over South San Francisco Bay was predominantly from the Northeast in the morning and from the Northwest in the afternoon (see Figure 2.2h). The wind speed was about $1-4\,\mathrm{m\,s^{-1}}$ in the morning and $3-6\,\mathrm{m\,s^{-1}}$ in the afternoon, as measured by adjacent NOAA weather station in Redwood City, CA (Figure 2.2e).

The low-pass filtered horizontal velocity measurements $(\widehat{u},\widehat{v})$ from the seventeen transects (referred to as T1-T17) are presented in Figure 3.1 along with the cross-sectional distributions of salinity. Raw velocity measurements (u,v) were filtered with a moving average filter with window size of 100 m in the lateral direction y and 1 m in the vertical direction z. From these measurements we computed lateral density gradient $\partial\rho/\partial y$, the buoyancy frequency squared $N^2=-(g/\rho_0)(\partial\rho/\partial z)$ and the lateral flow convergence $\partial\widehat{v}/\partial y$ (see Figure 3.2). The

contribution of salinity variations to density gradients is about one order of magnitude larger than the contribution of temperature variations, which we neglect from now on. The lateral and vertical derivatives were computed using a second order central finite difference.

Transects T1 and T2 take place during the accelerating phase of the ebb. The lateral velocity $\widehat{v}$ and lateral convergence $\partial\widehat{v}/\partial y$ are minimal. The salinity field is almost uniform in both transects therefore resulting in $N^2 \simeq 0\,\mathrm{s}^{-2}$, although a small lateral density gradient $\partial\rho/\partial y \simeq -1\times10^{-3}\,\mathrm{kg\,m}^{-4}$ develops in T2.

Transect T3 also takes place during the accelerating phase of the ebb. The lateral flow shows a convergence $\partial\widehat{v}/\partial y \simeq -1\times10^{-3}\,\mathrm{s}^{-1}$ developing at the edge of the shoal associated with a clockwise circulation (when looking down-estuary, i.e. in the positive x direction with the shoal on the right, which is the convention used throughout this article) over the slope: at the surface the lateral flow is directed toward the shoal at a speed $\widehat{v} \simeq -10\,\mathrm{cm\,s}^{-1}$ whereas at the bottom the lateral flow is directed toward the channel at a speed $\widehat{v} \simeq 5\,\mathrm{cm\,s}^{-1}$. The salinity field shows fresher water advected over the slope and channel, although N^2 remains small. However, the lateral density gradient strengthens at the edge of the shoal and reaches a value $\partial\rho/\partial y \simeq -2\times10^{-3}\,\mathrm{kg\,m}^{-4}$.

Transects T4 and T5 also take place during the accelerating phase of the ebb, and peak ebb (maximum longitudinal velocity $\widehat{u}$) over the shoal occurs around T5. These two transects show that the convergence of the lateral flow weakens and an anti-clockwise circulation develops over the slope: at the surface the lateral flow is directed toward the channel at a speed $\widehat{v} \simeq 5\,\mathrm{cm\,s}^{-1}$ whereas at the bottom the lateral flow is directed toward the shoal at a speed $\widehat{v} \simeq -5\,\mathrm{cm\,s}^{-1}$. Salinity observations show fresher water advected over the channel and slope and an increase of N^2 to a value $N^2 \simeq 5\times10^{-3}\,\mathrm{s}^{-2}$ at the surface over the slope on T4, which disappears on T5. The lateral density gradient also strengthens up to $\partial\rho/\partial y \simeq -4\times10^{-3}\,\mathrm{kg\,m}^{-4}$ over the shoal, but reverses over the slope where $\partial\rho/\partial y \simeq 3\times10^{-3}\,\mathrm{kg\,m}^{-4}$.

Transect T6 takes place at peak ebb in the channel and early in the decelerating phase on the shoal. The anti-clockwise lateral circulation over the slope strengthens: at the surface the lateral flow directed toward the channel speeds up to $\widehat{v} \simeq 10\,\mathrm{cm\,s}^{-1}$ and at the bottom the lateral flow directed toward the shoal also speeds up to $\widehat{v} \simeq -10\,\mathrm{cm\,s}^{-1}$. At the edge of the shoal, the lateral convergence is replaced by a lateral divergence $\partial\widehat{v}/\partial y \simeq 5\times10^{-4}\,\mathrm{s}^{-1}$. Salinity observations show a surface layer of fresher water appearing in the channel, as well as a decrease of salinity over the full depth on the shoal and the slope. N^2 increases again at the surface in the channel to $N^2 \simeq 5\times10^{-3}\,\mathrm{s}^{-2}$. The lateral density gradient on the slope decreases down to nearly zero, except at the surface where $\partial\rho/\partial y \simeq -5\times10^{-3}\,\mathrm{kg\,m}^{-4}$.

By the time of transect T7, the longitudinal velocity $\widehat{u}$ has decreased over the shoal but remains high in the channel. The anti-clockwise lateral circulation over the slope vanishes as the surface flow reverses toward the shoal. The salinity field shows that stable density stratification develops in the channel and over the slope, with N^2 reaching a maximum value $N^2 \simeq 10^{-2}\,\mathrm{s}^{-2}$ at the surface in the channel. The lateral density gradient is negative throughout the cross-section and reaches a peak value at the surface over the channel where $\partial\rho/\partial y \simeq -1\times10^{-2}\,\mathrm{kg\,m}^{-4}$.

During transects T8 and T9, the ebb keeps decelerating and the longitudinal velocity

on the shoal drops to $\widehat{u} \simeq 0\,\mathrm{cm\,s^{-1}}$. A lateral flow directed toward the channel at a speed $\widehat{v} \simeq 10\,\mathrm{cm\,s^{-1}}$ develops on the shoal. At the edge of the shoal a convergence front develops ($\partial\widehat{v}/\partial y \simeq -1 \times 10^{-3}\,\mathrm{s^{-1}}$) as the denser water mass flowing from the shoal plunges under a surface layer. This plunging is associated with a clockwise circulation over the slope: at the surface the lateral flow is directed toward the shoal at a speed $\widehat{v} \simeq -10\,\mathrm{cm\,s^{-1}}$ whereas at the bottom the lateral flow is directed toward the channel at a speed $\widehat{v} \simeq 15\,\mathrm{cm\,s^{-1}}$. The salinity observations show a salinity increase over the shoal and a salinity decrease over the full depth on the slope and in the channel. The salinity increase over the shoal is probably connected to lateral advection of saltier water from further up the shoal. N^2 remains high at the surface over the channel and the slope. A lateral density gradient $\partial\rho/\partial y \simeq 3 - 5 \times 10^{-3}\,\mathrm{kg\,m^{-4}}$ develops over the slope.

Transects T10 and T11 show the tide reversing on the shoal and at the bottom of the channel and slope whereas surface longitudinal velocity $\widehat{u}$ decreases over the slope and the channel. The observations of lateral velocity $\widehat{v}$ show that the plunging at the edge of the shoal and the clockwise lateral circulation over the slope weaken and are progressively replaced by an anti-clockwise circulation as the channel bottom water mass flows onto the slope toward the shoal at a speed $\widehat{v} \simeq -5\,\mathrm{cm\,s^{-1}}$. The salinity field shows that density stratification is restored over the channel and slope and extends onto the shoal. The lateral density gradient $\partial\rho/\partial y$ on the slope also decreases to nearly zero.

Finally, the flood accelerates during transects T12 to T17. The anti-clockwise lateral circulation weakens and eventually vanishes. The surface salinity increases uniformly and the density stratification and lateral density gradient decrease until T17 when the salinity field returns to a nearly homogeneous state.

To summarize, we observe high intratidal variability of the lateral velocity $\widehat{v}$ and salinity field s, especially during the ebb. The most striking features are the fluctuations of the lateral salinity gradient $\partial s/\partial y$ and lateral circulation over the slope and the formation of surface convergence fronts at the edge of the shoal on T3 and T8/T9. These features are analyzed and discussed in the following section.

3.2 Dynamics of the Lateral Density Gradient

To identify the processes involved in the dynamics of the lateral salinity gradient $\partial s/\partial y$, we start from the salt budget which can be written as an advection-diffusion equation:

$$\frac{\partial s}{\partial t} = -u\frac{\partial s}{\partial x} - v\frac{\partial s}{\partial y} - w\frac{\partial s}{\partial z} + \frac{\partial}{\partial z}\left(k_t\frac{\partial s}{\partial z}\right) \tag{3.1}$$

where k_t is a vertical turbulent diffusivity. Taking the lateral derivative of equation (3.1) reveals the different processes involved in the dynamics of the lateral salinity gradients:

$$\frac{\partial}{\partial t}\left(\frac{\partial s}{\partial y}\right) = -\frac{\partial}{\partial y}\left(u\frac{\partial s}{\partial x}\right) - \frac{\partial}{\partial y}\left(v\frac{\partial s}{\partial y}\right) - \frac{\partial}{\partial y}\left(w\frac{\partial s}{\partial z}\right) + \frac{\partial}{\partial y}\frac{\partial}{\partial z}\left(k_t\frac{\partial s}{\partial z}\right) \tag{3.2}$$

The term on the left hand side of equation (3.2) is the rate of change of the salinity gradient. The first term on the right hand side (r.h.s.) represents the process of differential advection first analyzed by Nunes and Simpson (1985) and Huzzey and Brubaker (1988). We expect this process to be the primary source of surface lateral density gradient at the slope-shoal interface during the ebb as freshwater is advected faster in the channel and over the slope than over the shoal. The second and third terms on the r.h.s. represent lateral and vertical advection and are likely to be important in areas of convergence or divergence. The fourth and last term on the r.h.s. represents lateral variations in vertical mixing, which were found to be predominant in the lower Passaic River, New Jersey by Cheng et al. (2009).

The rate of change $\partial/\partial t(\partial s/\partial y)$ and the lateral advection $-\partial/\partial y\,(v(\partial s/\partial y))$ terms can be estimated straightforwardly from the transect data, using the low-pass filtered velocity $(\widehat{u},\widehat{v})$. Since the salinity and velocity measurements were collected alternatively, we perform a linear interpolation in time of the salinity field to derive the salinity field and estimate the lateral advection term $-\partial/\partial y\,(v(\partial s/\partial y))$ at the times of the velocity transects. The time derivative of the lateral salinity gradient $\partial/\partial t(\partial s/\partial y)$ is estimated as a second-order centered finite difference of two successive $\partial s/\partial y$ transects, and therefore falls on the same timeline as the velocity transects.

The two resolved terms of equation (3.2) are of same order of magnitude (Figure 3.3). The rate of change $\partial/\partial t(\partial s/\partial y)$ displays large spatial and temporal variations throughout the period sampled. First, we observe a decrease of the lateral salinity gradient ($\partial/\partial t(\partial s/\partial y) \simeq -5\times10^{-6}\,\mathrm{psu\,m^{-1}\,s^{-1}}$) in the channel at the time of transect T6 (Figure 3.3a and Figure 3.2c between T6 and T7). This decrease is consistent with the process of differential advection (term $-(\partial/\partial y((u(\partial s/\partial x))$ in equation (3.2)) and lateral advection does not appear to contribute to this decrease. Another interesting feature emerging is the decrease of the lateral salinity gradient ($\partial/\partial t(\partial s/\partial y) \simeq -5\times10^{-6}\,\mathrm{psu\,m^{-1}\,s^{-1}}$) at the edge of the shoal at the time of transect T7 (Figure 3.3a and Figure 3.2c between T7 and T8). This feature appears to be driven primarily by the lateral advection term $-\partial/\partial y\,(v(\partial s/\partial y))$ (Figure 3.3b), although differential advection might also contribute at leading order. Another striking feature is the increase of the lateral salinity gradient ($\partial/\partial t(\partial s/\partial y) \simeq 2-5\times10^{-6}\,\mathrm{psu\,m^{-1}\,s^{-1}}$) on the slope at the time of transects T3 (Figure 3.3a and Figure 3.2c between T3 and T4) and T7 (Figure 3.3a and Figure 3.2c between T7 and T8). Estimates of the Gradient Richardson number

$$Ri_g = \frac{-\frac{g}{\rho_0}\frac{\partial\rho}{\partial z}}{\left(\frac{\partial u}{\partial z}\right)^2+\left(\frac{\partial v}{\partial z}\right)^2} \tag{3.3}$$

during transect T6 and T7 reveal a region over the slope characterized by $Ri_g \leq 1/4$ where the necessary condition for shear instability is met (Figure 3.4). However in the channel, most of the water column is characterized by $Ri_g \geq 1/4$ with the exception of the near-bed region. This suggests that vertical mixing is less inhibited by the stable density stratification over the slope than in the channel, and that lateral variation in vertical mixing (term $(\partial/\partial y)(\partial/\partial z\,(k_t(\partial s/\partial z)))$ in equation (3.2)) is driving this increase of $\partial s/\partial y$ over the slope.

To summarize, these observations suggest that all processes involved in the budget for the lateral salinity gradient (equation (3.2)), except for the vertical advection term $-\partial/\partial y\,(w(\partial s/\partial z))$ which could not be evaluated, contribute at leading order. During the ebb, the process of differential advection (term $-(\partial/\partial y((u(\partial s/\partial x)))$ sets a surface lateral density gradient at the shoal-channel interface. Lateral advection (term $-\partial/\partial y\,(v(\partial s/\partial y))$) resulting from the convergence front developing during transects T8/T9 sharpens then the lateral density gradient at the edge of the shoal. Lateral variations in vertical mixing between the slope and channel (term $(\partial/\partial y)(\partial/\partial z\,(k_t(\partial s/\partial z))))$ compete with the process of differential advection by creating a lateral density gradient of opposite sign over the slope.

3.3 Dynamics of the Lateral Circulation

In this system, the lateral circulation over the slope displays rich intratidal dynamics, reversing three times during the sampled ebb, around transects T4 and T7 (Figure 3.1b). To investigate the processes driving the dynamics of the lateral circulation, we set a budget for the longitudinal vorticity $\omega_x = \partial w/\partial y - \partial v/\partial z$ which quantifies the direction and strength of the lateral circulation. A clockwise lateral circulation corresponds to $\omega_x > 0$ while an anti-clockwise circulation corresponds to $\omega_x < 0$. From the continuity equation, we can scale the characteristic vertical velocity W as a function of the characteristic lateral velocity V, the characteristic lateral lengthscale $L \simeq 10^3\,\mathrm{m}$ (the width of the shoal-channel interface in this case) and the water depth $H \simeq 10\,\mathrm{m}$:

$$W \sim \frac{H}{L} V \sim 10^{-2} \times V \tag{3.4}$$

From this scaling we can infer:

$$\frac{\partial w}{\partial y} \sim \frac{W}{L} \sim \left(\frac{H}{L}\right)^2 \frac{V}{H} \sim 10^{-4} \times \frac{\partial v}{\partial z} \tag{3.5}$$

and simplify the longitudinal vorticity expression to $\omega_x \simeq -\partial v/\partial z$. In that simplified case, we can derive an equation for ω_x from the Reynolds-averaged lateral momentum budget:

$$\frac{\partial v}{\partial t} = -u\frac{\partial v}{\partial x} - v\frac{\partial v}{\partial y} - w\frac{\partial v}{\partial z} - fu - \frac{1}{\rho}\frac{\partial p}{\partial y} + \frac{\partial}{\partial z}\left(\nu_t \frac{\partial v}{\partial z}\right) \tag{3.6}$$

where ν_t is a vertical eddy viscosity and $f \simeq 8.9 \times 10^{-5}\,\mathrm{s}^{-1}$ is the Coriolis frequency at the latitude of the field site ($37°\,34'\,35''$N). Since the characteristic lateral lengthscale $L \simeq 10^3\,\mathrm{m}$ is much larger than the characteristic vertical lengthscale $H \simeq 10\,\mathrm{m}$ in this system, we use the hydrostatic approximation and write the lateral pressure gradient as the sum of a barotropic and baroclinic pressure gradients:

$$\frac{\partial p}{\partial y} = \frac{\partial}{\partial y}\left(\int_z^\eta g\rho(y,z)dz\right) = g\frac{\partial \eta}{\partial y}\rho(y,\eta) + \int_z^\eta g\frac{\partial \rho}{\partial y}dz \simeq \rho_0 g\frac{\partial \eta}{\partial y} + \int_z^\eta g\frac{\partial \rho}{\partial y}dz \tag{3.7}$$

Since lateral density variations result for the most part from salinity variations as mentioned earlier, we write the lateral density gradient as

$$\frac{\partial \rho}{\partial y} \simeq \rho_0 \beta \frac{\partial s}{\partial y} \tag{3.8}$$

where $\beta \simeq 7.6 \times 10^{-4}\,\mathrm{psu}^{-1}$ is the coefficient of saline contraction. Substituting (3.7) and (3.8) in (3.6) yields then:

$$\frac{\partial v}{\partial t} = -u\frac{\partial v}{\partial x} - v\frac{\partial v}{\partial y} - w\frac{\partial v}{\partial z} - fu - g\frac{\partial \eta}{\partial y} - g\beta \int_z^\eta \frac{\partial s}{\partial y} dz + \frac{\partial}{\partial z}\left(\nu_t \frac{\partial v}{\partial z}\right) \tag{3.9}$$

Finally, taking the vertical derivative of (3.9) yields a budget for the longitudinal vorticity ω_x:

$$\frac{\partial \omega_x}{\partial t} = \frac{\partial}{\partial z}\left(u\frac{\partial u}{\partial x}\right) + \frac{\partial}{\partial z}\left(v\frac{\partial v}{\partial y}\right) + \frac{\partial}{\partial z}\left(w\frac{\partial v}{\partial z}\right) + f\frac{\partial u}{\partial z} - g\beta\frac{\partial s}{\partial y} - \frac{\partial^2}{\partial z^2}\left(\nu_t \frac{\partial v}{\partial z}\right) \tag{3.10}$$

which does not involve the barotropic pressure gradient $g\partial\eta/\partial y$. This approach is similar to the absolute vorticity analysis developed by Valle-Levinson et al. (2003). The term on the left hand side of (3.10) is the rate of variation of the longitudinal vorticity ω_x. The first three terms on the r.h.s. represent the effects of longitudinal, lateral and vertical advection. The third term on the r.h.s. $f\partial u/\partial z$ represents the effects of rotation. In this system, the vertical shear is positive ($u > 0$; $\partial u/\partial z > 0$) during ebbs. The Coriolis acceleration forces then a negative lateral flow $v < 0$ (towards the shoal) stronger at the surface than at the bottom ($\partial v/\partial z < 0$). As a result rotation acts to develop positive longitudinal vorticity $\omega_x > 0$ during ebbs and negative longitudinal vorticity $\omega_x < 0$ during floods. The fourth term on the r.h.s. $-g\beta\partial s/\partial y$ represents the effects of the lateral salinity gradient. If the lateral salinity gradient is positive, the lateral baroclinic pressure gradient forces a negative flow $v < 0$ stronger at the bottom than at the surface ($\partial v/\partial z > 0$). As a result, positive salinity gradients act to develop negative longitudinal vorticity $\omega_x < 0$. The fifth and last term on the r.h.s. $-(\partial^2/\partial z^2)\,(\nu_t \partial v/\partial z)$ represents the effects of vertical variations in vertical mixing.

All terms of equation (3.10) except for the longitudinal and vertical advection terms and the vertical mixing term are estimated using the low-pass filtered velocities $(\widehat{u}, \widehat{v})$ from the transect data. The Coriolis term and the lateral advection term are linearly interpolated on the same timeline as the salinity transects and the lateral salinity gradient term. The time derivative $\partial\omega_x/\partial t$ is estimated with a second order centered finite difference between two successive ω_x transects and therefore falls on the same timeline as the salinity transects.

The variation rate of the longitudinal vorticity $\partial\omega_x/\partial t$ (Figure 3.5a) and the lateral salinity gradient term $-g\beta\partial s/\partial y$ (Figure 3.5d) appear as the dominant terms of the vorticity budget (3.10) during the ebb. More specifically, the reversals of the lateral circulation from clockwise to anti-clockwise around transects T3 and T4 is driven for the most part

by the lateral salinity gradient (see Table 3.1). The second reversal from anti-clockwise to clockwise around transects T7 is driven primarily by the lateral salinity gradient, but with a contribution at leading order of the Coriolis and advection terms (see Table 3.1). The third circulation reversal from clockwise to anti-clockwise at the end of the ebb is again driven primarily by the lateral salinity gradient, with a contribution at leading order of the Coriolis and lateral advection terms (see Table 3.1). The lateral advection term (Figure 3.5b) is smaller for most of the period sampled, except late in the ebb as a convergence front develops from transect T8 through T10. The Coriolis term is also smaller but not negligible during the ebb (Figure 3.5c) and might become predominant in the later part of the flood (transects T16 and beyond) as the lateral salinity gradient vanishes. The friction term $-(\partial^2/\partial z^2)\,(\nu_t \partial v/\partial z)$ and the longitudinal and vertical advection terms can not be estimated here and their role remain uncertain.

To summarize, the lateral circulation can be analyzed conveniently in terms of the longitudinal vorticity ω_x since the budget (3.10) does not involve the barotropic pressure gradient and most terms can be estimated from velocity and salinity transects. In this system, inertia and lateral salinity gradient emerge as the dominant terms of equation (3.10) during the ebb. The Coriolis and lateral advection terms are smaller but also contribute at leading order.

3.4 Implications for Convergence Fronts

Various convergence front formation (frontogenesis) mechanisms at the edge of a channel during ebb tides have been identified and analyzed in previous studies. The effect of Earth's rotation have been identified as a potential frontogenesis mechanism by Mied et al. (2000) and studied further by Handler et al. (2001), Mied et al. (2002) and Handler et al. (2009). Valle-Levinson et al. (2000) found that the coupling of the along-estuary divergence of the primary flow $\partial u/\partial x$, lateral bathymetry variations $\partial h/\partial y$ and the lateral convergence rate $\partial v/\partial y$ through the depth-averaged continuity equation could lead to formation of lateral convergence fronts at the edge of the channel during ebbs. Valle-Levinson et al. (2003) found that the coupling of the lateral shear of the primary flow $\partial u/\partial y$ and the lateral convergence rate $\partial v/\partial y$ through the budget for the absolute vorticity $\xi_a = f + \partial v/\partial x - \partial u/\partial y \simeq f - \partial u/\partial y$ could also lead to front formation at the shoal-channel interface during ebbs. While this dataset does not allow for an extensive analysis of frontogenesis at the shoal-channel interface in this system, it provides important clues about the effects of the lateral circulation on the convergence fronts. During the tidal cycle sampled on 5 March 2009, the development of a convergence front at the edge of the shoal is correlated with the direction of the lateral circulation on the slope. A convergence front develops briefly at the edge of the shoal early in the ebb (transects T2 and T3), while a clockwise circulation develops on the slope (Figure 3.6a). The front vanishes then for about two hours around peak ebb (transects T4 through T7), when an anti-clockwise circulation develops on the slope (Figure 3.6b), and appears again late in the ebb (transects T8 through T11) as the lateral circulation reverses to a clockwise direction (Figure 3.6c). It disappears again at the beginning of the successive flood

(transects T12 through T17) as the lateral circulation reverses again to an anti-clockwise direction (Figure 3.6d). These observations suggest therefore that the lateral circulation on the slope can greatly affect the strength of convergence fronts developing at the edge of the shoal during ebbs, strengthening them during the early and late ebb and weakening them during peak ebb in this system.

3.5 Sensitivity to Tidal and Stratification Conditions

Datasets from the moored instrument provide important clues about the repeatability of the patterns described and analyzed in sections 3a-3c under various tidal and stratification conditions. More specifically we focus on the depth-averaged longitudinal vorticity $\langle\omega_x\rangle$ and the surface-bottom density difference $\Delta\rho/\rho_0 = \beta(s_{surface} - s_{bottom})$ at the central mooring on the slope. As detailed in the section 3.b, the depth-averaged longitudinal vorticity $\langle\omega_x\rangle$ quantifies the direction and strength of the lateral circulation over the slope. The surface-bottom density difference $\Delta\rho/\rho_0 = \beta(s_{surface} - s_{bottom})$ provides information about vertical mixing on the slope: a small surface-bottom density difference suggests that the water column over the slope is partially mixed whereas large surface-bottom density differences suggest weak vertical mixing. $\langle\omega_x\rangle$ and $\Delta\rho/\rho_0$ are estimated over a ten days period (from decimal day 55 until decimal day 65) and interpolated on a 5 minutes resolution timeline and low-pass filtered with a moving average with window size of 30 minutes (Figure 3.7). This ten days period was selected because it displays variations in both tidal and stratification conditions.

The depth-averaged longitudinal vorticity $\langle\omega_x\rangle$ displays a repeatable pattern over the nine days preceding the 5 March transect survey (Figure 3.7b). During all ebb tides except for the four with the smallest amplitude ($\leq 1\,\mathrm{m}$), $\langle\omega_x\rangle$ increases at the beginning of the ebb, then decreases around peak ebb, then increases again at the end of the ebb. During some ebbs $\langle\omega_x\rangle$ decreases down to a negative value, corresponding to a circulation reversal around peak ebb, such as observed during the 5 March 2009 transect survey (Figure 3.6b). The periods when $\langle\omega_x\rangle$ decreases are also characterized by a decrease of the surface-bottom density difference $\Delta\rho/\rho_0$ (Figure 3.7c), most likely due to the intensification of turbulent vertical mixing on the slope around peak ebb. This reduction of density stratification over the slope is consistent with salinity transects T5 and T6 (Figures 3.1c and 3.6f) and is likely to be associated with the development of a positive lateral salinity gradient $\partial s/\partial y > 0$ over the slope because of lateral variations in vertical mixing as discussed in section 3a. This lateral density gradient is then the dominant mechanism driving the observed lateral circulation reversals as established in section 3c. These patterns were also observed at the other northernmost slope mooring (the ADCP on the southernmost slope mooring failed during the winter experiment) and other periods of the winter experiment.

The lateral circulation appears to be rather insensitive to stratification conditions. The peak surface-bottom density difference is quite steady around $\Delta\rho/\rho_0 \simeq -5\times10^{-4}$ during the first half of the record but triples to $\Delta\rho/\rho_0 \simeq -15\times10^{-4}$ over the last five days (Figure 3.7c)

as a result of the 2/3 March 2009 storm. Meanwhile the peak $\langle\omega_x\rangle$ does not show similar variations and remains between $\langle\omega_x\rangle \simeq 3 \times 10^{-2}\,\mathrm{s}^{-1}$ and $\langle\omega_x\rangle \simeq 5 \times 10^{-2}\,\mathrm{s}^{-1}$ (Figure 3.7b). The lateral circulation appears to be more sensitive to tidal amplitude as the four smallest ebbs are characterized by weak ($\langle\omega_x\rangle \leq 1 \times 10^{-2}\,\mathrm{s}^{-1}$) or non-existent lateral circulation (Figure 3.7b, non highlighted). These observations from moored instruments suggest therefore that the mechanisms identified in section 3a-3c are involved in all partially-stratified ebb tides in South San Francisco Bay, except for the smallest.

3.6 Summary

We have described and analyzed the intratidal dynamics of fronts and lateral circulation at the shoal-channel interface of a wide, straight and partially stratified drowned river estuary. During the ebb, a lateral density gradient develops at the interface and is characterized by high spatial and temporal variability resulting from the competition between differential advection, non-linear advection terms and lateral variations in vertical mixing. The effects of non-linear advection terms are strongest when a lateral convergence front develops at the edge of the shoal. During the ebb, the lateral circulation is driven for the most part by a balance between inertia and the lateral baroclinic pressure gradient, and reverses three times as a result of the temporal variations of the lateral density gradient on the slope. The lateral advection and Coriolis terms are smaller but non negligible and the roles of longitudinal and vertical advection and friction remain uncertain. The direction of the lateral circulation on the slope can greatly affect convergence fronts developing at the edge of the shoal during the ebb. In this system, a clockwise circulation (positive vorticity) strengthens convergence fronts whereas an anti-clockwise circulation (negative vorticity) weakens convergence fronts. Consequently, convergence fronts display a similar variability during the ebb, weakening around peak ebb and strengthening early and late in the ebb. Observations from moored instruments on the slope suggest that these processes are involved in all partially-stratified ebb tides in this system except for the smallest, and are more sensitive to tidal amplitude than density stratification.

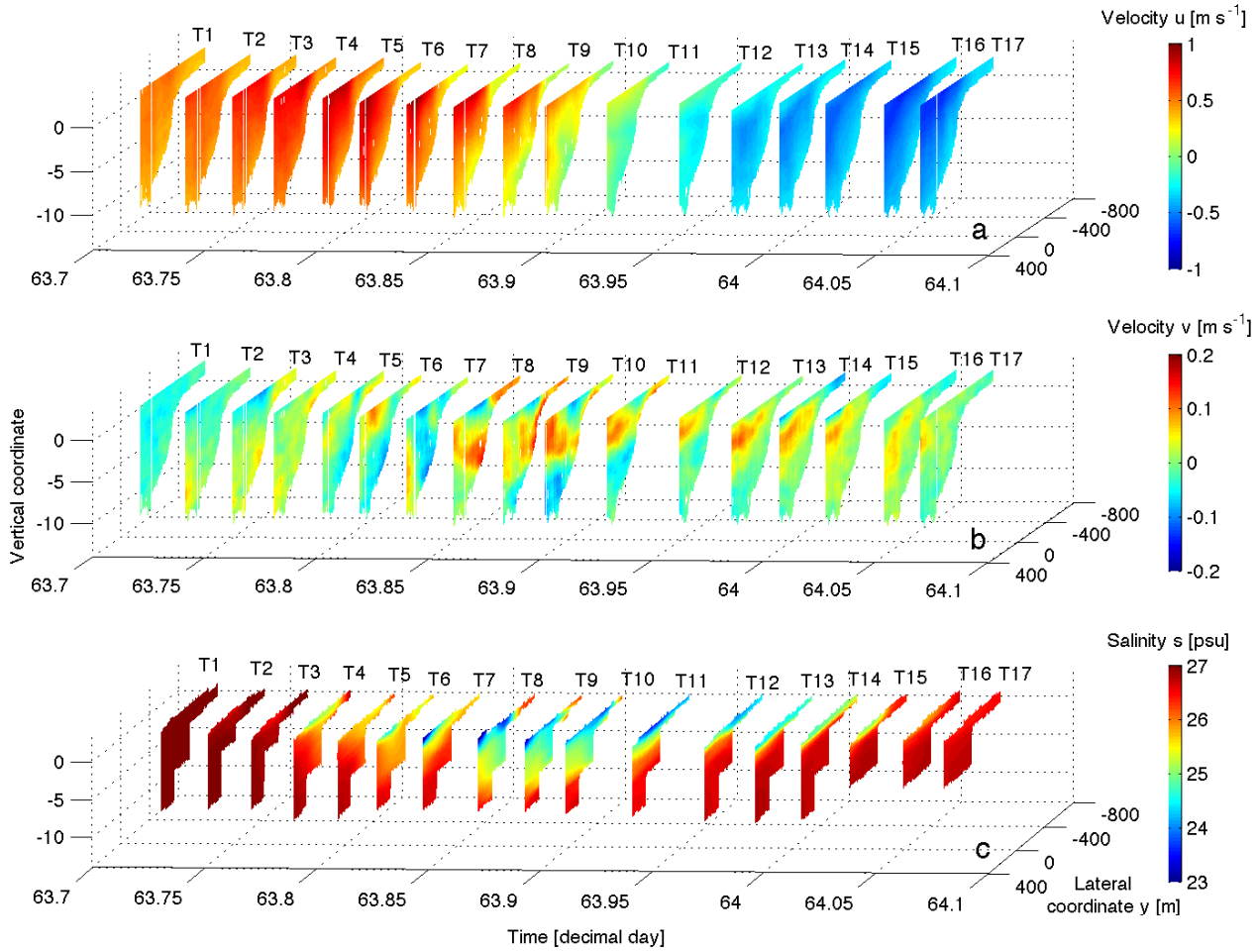

Figure 3.1: Transect observations of the low-pass filtered longitudinal velocity $\widehat{u}$ (a), low-pass filtered lateral velocity $\widehat{v}$ (b) and salinity (c). The time between two transects is about thirty minutes.

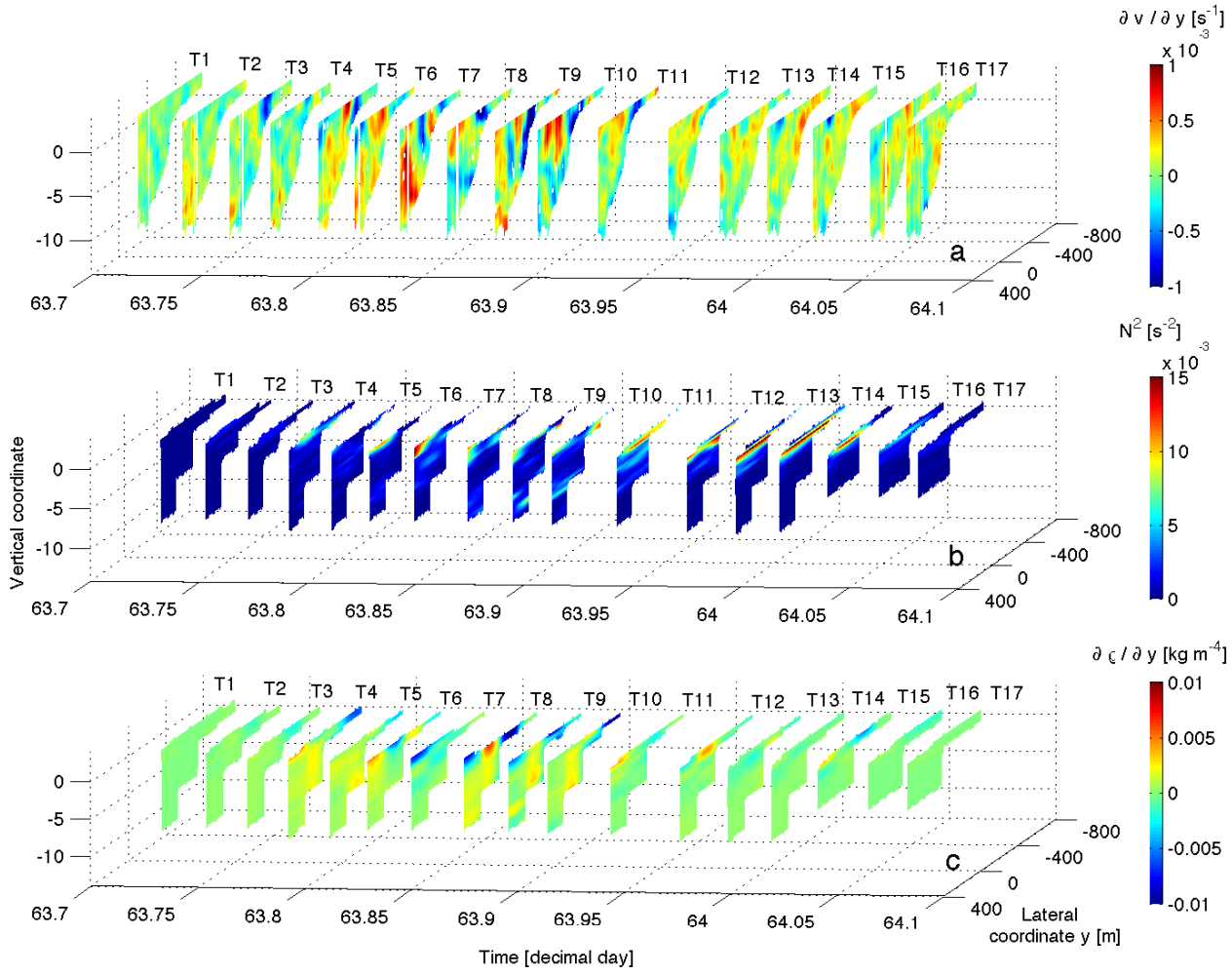

Figure 3.2: Transect observations of the lateral convergence $\partial\widehat{v}/\partial y$ (a), the Brunt-Vaisala frequency squared $N^2 = -(g/\rho_0)(\partial\rho/\partial z)$ (b) and the lateral density gradient $\partial\rho/\partial y$ (c). The time between two transects is about thirty minutes.

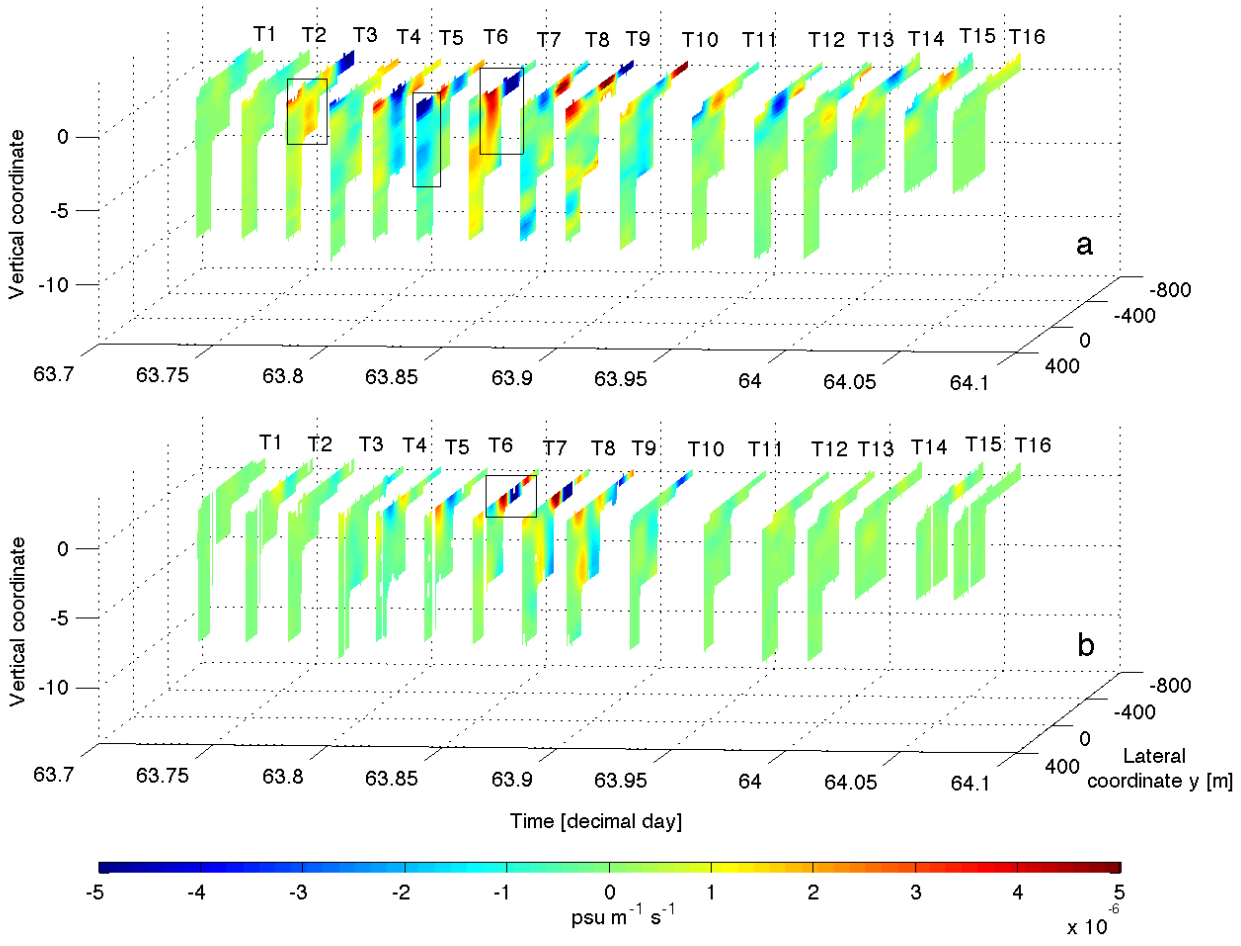

Figure 3.3: Contribution of lateral advection to the lateral salinity gradient budget: estimates of the rate of change $\partial/\partial t(\partial s/\partial y)$ (a) and the lateral advection term $-\partial/\partial y\,(v(\partial s/\partial y))$ (b). The rectangles highlight features discussed in the text.

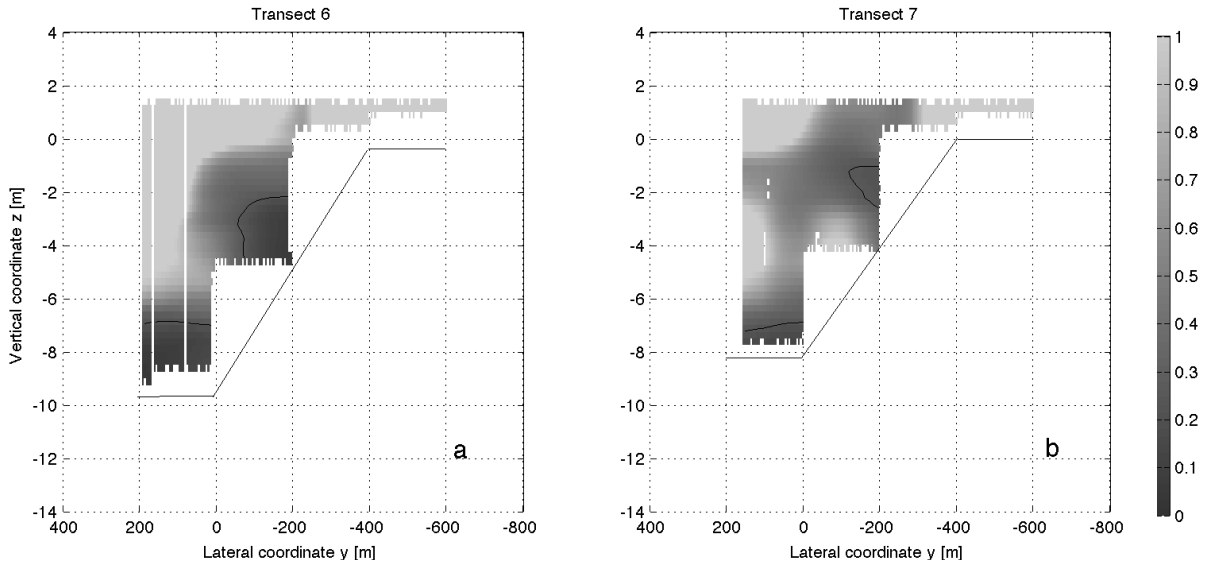

Figure 3.4: Gradient Richardson number distribution during transects T6 (a) and T7 (b). The black contours represent the threshold $Ri_g = 1/4$. The black solid line represents the approximate location of the bottom.

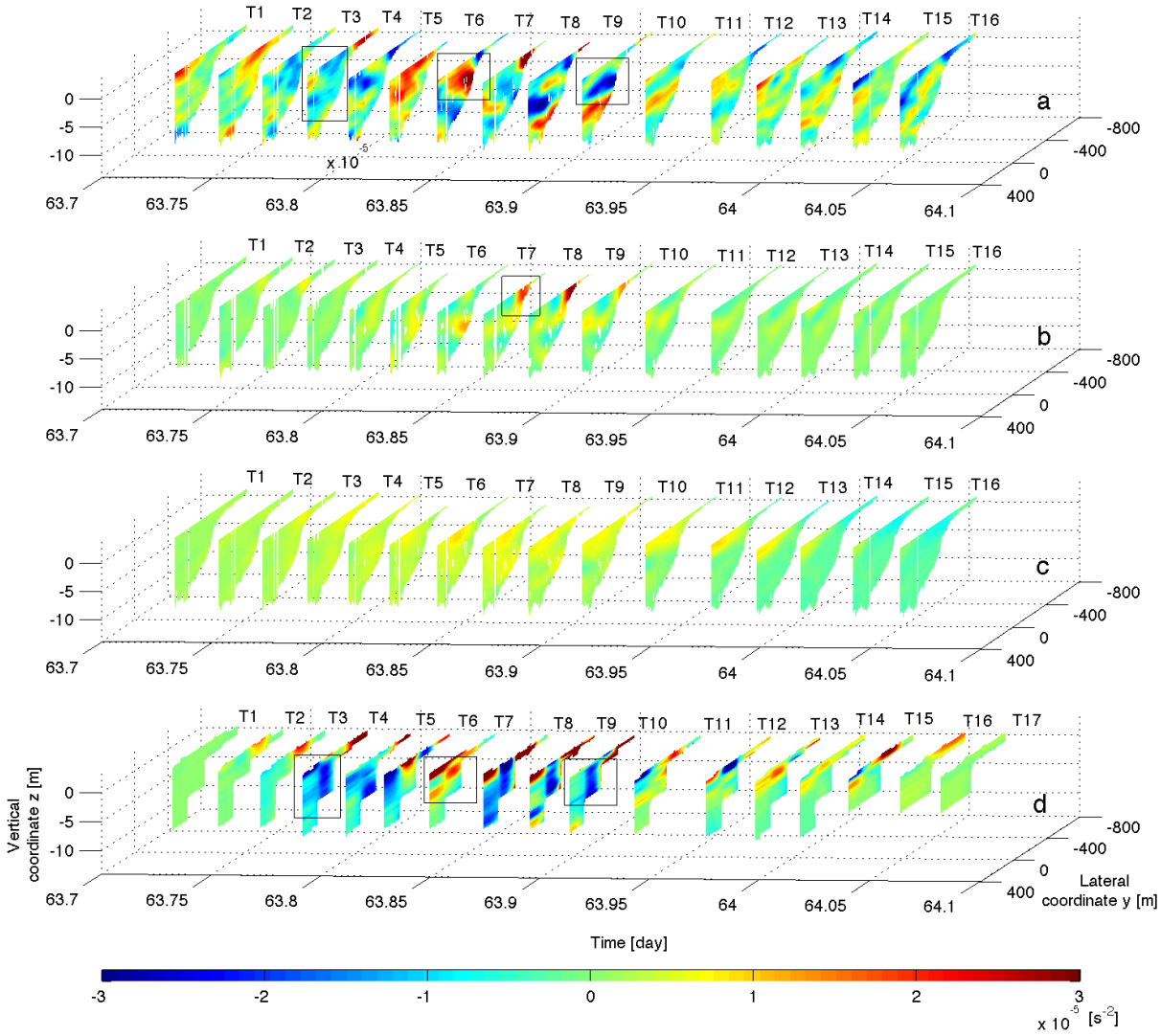

Figure 3.5: Budget of the longitudinal vorticity ω_x: estimates of the rate of change $\partial\omega_x/\partial t$ (a), lateral advection term $\partial/\partial z\,(v(\partial v/\partial y))$ (b), Coriolis term $f\partial u/\partial z$ (c) and lateral salinity gradient term $-g\beta\partial s/\partial y$ (d). The rectangles highlight features discussed in the text.

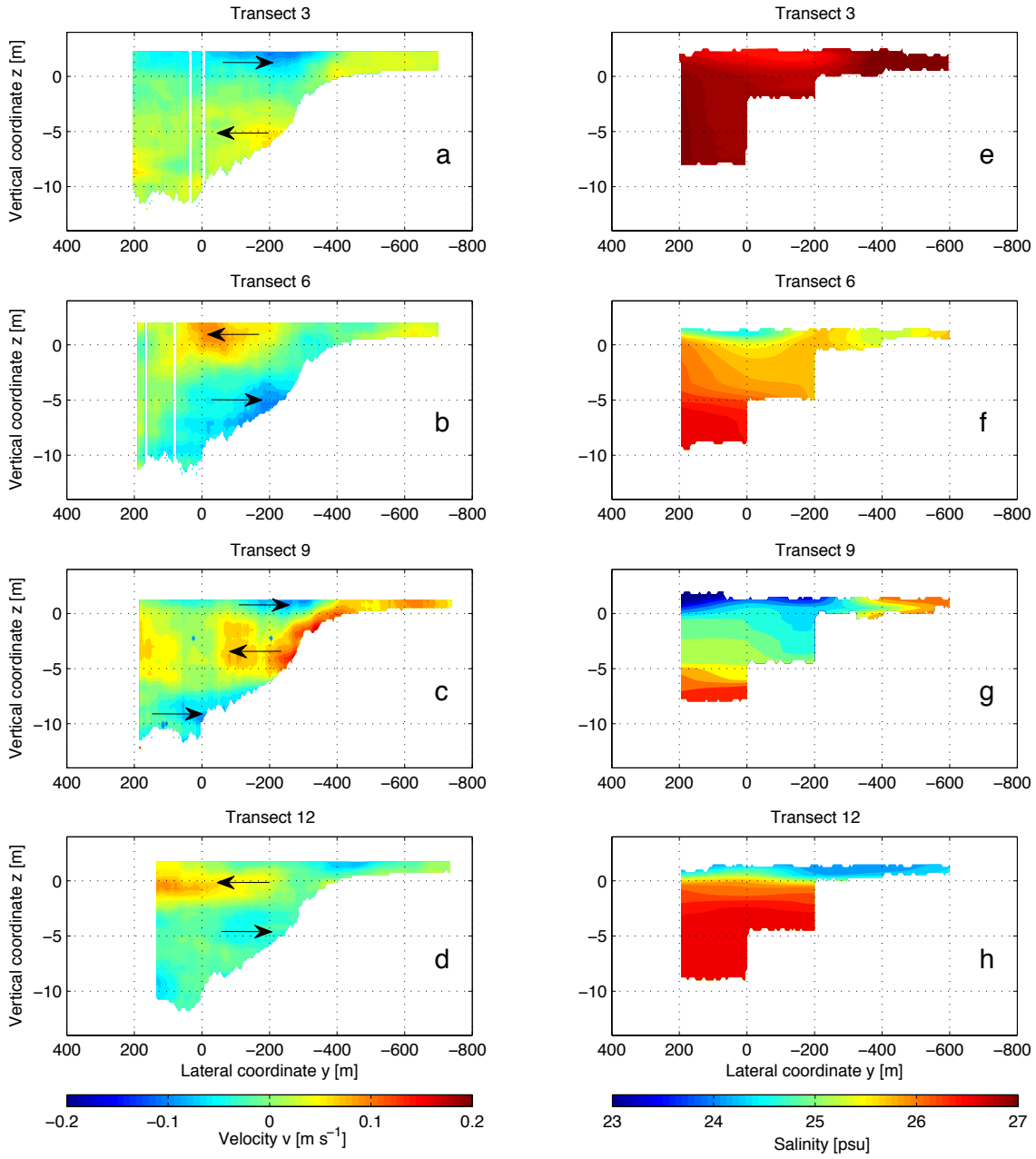

Figure 3.6: Low-pass filtered lateral velocity $\widehat{v}$ (a,b,c,d) and salinity (e,f,g,h) during transects T3 (a,e), T6 (b,f), T9 (c,g) and T12 (d,h). Arrows represent the direction of the lateral flow and highlight the circulation over the slope.

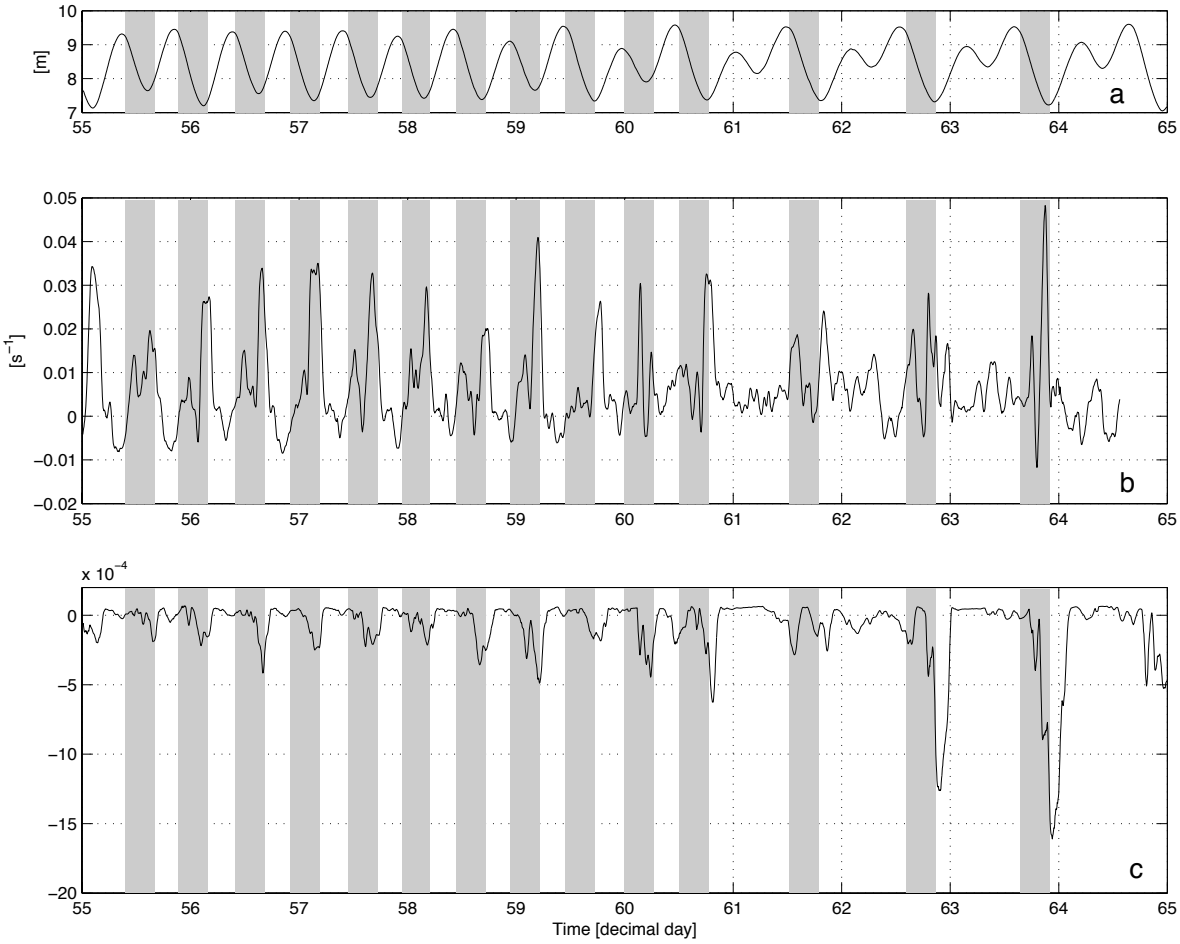

Figure 3.7: Long term records from the central mooring located halfway up the slope: water depth (a), depth-averaged longitudinal vorticity $\langle \omega_x \rangle$ (b) and surface-bottom density difference $\Delta\rho/\rho_0 = \beta(s_{surface} - s_{bottom})$ (c). The shaded areas highlight the ebb tides except for the four smallest. The 5 March 2009 transect survey corresponds to the last highlighted ebb and the early part of the successive flood (decimal days 63.7 to 64.1).

Table 3.1: Magnitude of the terms from the longitudinal vorticity budget (3.10) over the slope. The terms are given in $10^{-5}\,\mathrm{s}^{-2}$.

$Terms$		$T4$	$T7$	$T10$
$\partial\omega_x/\partial t$	$\simeq$	-1	2	-2
$\partial/\partial z\,(v\partial v/\partial y)$	$\simeq$	0.1	0.5	0.5
$f\partial u/\partial z$	$\simeq$	0.5	1	0.5
$-g\beta\partial s/\partial y$	$\simeq$	-2	2	-2

Chapter 4

Vertical Turbulent Mixing

This chapter addresses the second research question described in section 1.3. Turbulence dynamics are described by the TKE equation, an advection-diffusion equation with source and sink terms (Stacey et al. 2012):

$$\frac{\partial q^2}{\partial t} + \overline{u}\frac{\partial q^2}{\partial x} + \overline{v}\frac{\partial q^2}{\partial y} + \overline{w}\frac{\partial q^2}{\partial z} = \frac{\partial}{\partial x}\left(K_x\frac{\partial q^2}{\partial x}\right) + \frac{\partial}{\partial y}\left(K_y\frac{\partial q^2}{\partial y}\right) + \frac{\partial}{\partial z}\left(K_z\frac{\partial q^2}{\partial z}\right) + 2P + 2B - 2\epsilon \tag{4.1}$$

where q^2, P, B, ϵ are the TKE, TKE shear production, buoyancy flux and TKE dissipation rate introduced in section 1.1, equations (1.8)-(1.12). K_x, K_y and K_z are turbulent diffusion coefficients. The TKE shear production P, TKE dissipation rate ϵ and buoyancy flux B in the channel and on the slope are estimated and compared using the data from the channel (ch) and slope mid (slm) moorings (Figure 1.1) during the first nine days of the winter experiment ($t = 55$ days to $t = 64$ days), a period which captures both changes in tidal forcing (spring-neap transition) and freshwater inflows. This analysis also relies on the salinity and velocity profiles from the 5 March 2009 transect survey, which showed the strongest density gradients and lateral circulation of all the transect surveys as a result of the 2/3 March 2009 storm.

As discussed in chapter 3, the lateral circulation on the slope is the most prominent dynamical feature at the shoal-channel interface. The lateral circulation can have two effects on turbulence dynamics: it can directly impact (4.1) through the lateral advection term $\overline{v}\,(\partial q^2/\partial y)$, but it can also have indirect effects on the source term, the TKE shear production P. The objectives of this chapter are therefore to characterize turbulence dynamics at the shoal-channel interface and analyze the effects of the lateral circulation.

4.1 Mean flow observations

The velocity profiles are decomposed as the sum of a mean and a fluctuating component $u(z,t) = \overline{u}(z,t) + u'(z,t)$ where the mean component $\overline{u}(z,t)$ is computed by averaging 900 ensembles of raw velocity data in the channel and on the slope, which corresponds to a 15-min block-average in the channel and a 21-min block-average on the slope. This value of

900 ensembles is long enough to reduce the noise in the estimates of the turbulent quantities presented in section 4.2 but small enough to preserve the intratidal variability. In this system, salinity dominates density variations and the effects of temperature are neglected.

The first half of the record ($t = 55$ days to $t = 60$ days) was characterized by spring tides with an amplitude of about 1 m (2 m between high and low waters) and peak longitudinal velocities at the surface $|\overline{u}| \simeq 1\,\mathrm{m\,s^{-1}}$ in the channel and $|\overline{u}| \simeq 0.7\,\mathrm{m\,s^{-1}}$ on the slope (Figure 4.1a,b). During this period, the surface salinity in the channel and on the slope oscillates between $s \simeq 28$ psu at high slack water and $s \simeq 27$ psu at low slack water (Figure 4.1e,f). The second half of the record ($t = 60$ days to $t = 64$ days) was characterized by smaller floods and every other ebb tide. During these smaller floods, the peak longitudinal velocities at the surface were $|\overline{u}| \simeq 0.5\,\mathrm{m\,s^{-1}}$ in the channel and $|\overline{u}| \simeq 0.4\,\mathrm{m\,s^{-1}}$ on the slope (Figure 4.1a,b). During the smaller ebbs the peak longitudinal velocities at the surface were $\overline{u} \simeq 0.4\,\mathrm{m\,s^{-1}}$ in the channel and $\overline{u} \simeq 0.3\,\mathrm{m\,s^{-1}}$ on the slope (Figure 4.1a,b). As a result of the 2/3 March 2009 rainstorm, the surface salinity decreases to $s \simeq 27$ psu at high slack water and drops below $s \simeq 25$ psu in the channel and on the slope during the $t = 63.9$ days low slack water (Figure 4.1e,f). In the channel, the mean lateral velocity remains small ($\overline{v} < 0.1\,\mathrm{m\,s^{-1}}$) throughout most of this record (Figure 4.1c). On the slope, a lateral circulation develops during most of the ebbs on record as discussed in chapter 3, with peak lateral velocities at the end of the ebb around $\overline{v} \simeq 0.15\,\mathrm{m\,s^{-1}}$ near the bed and $\overline{v} \simeq -0.15\,\mathrm{m\,s^{-1}}$ near the surface (Figure 4.1d).

The 5 March transect survey spanned over four hours and forty minutes of a large ebb tide (2.5 m and seven hours eighteen minutes from higher high to lower low water) and over four hours and twenty minutes of the successive smaller flood tide (2 m and seven hours thirty-six minutes from lower low to lower high water). During the surveyed ebb, peak longitudinal velocities at the surface were $\overline{u} \simeq 1\,\mathrm{m\,s^{-1}}$ in the channel and $\overline{u} \simeq 0.9\,\mathrm{m\,s^{-1}}$ on the slope (Figure 4.2a,b). During the following flood, peak longitudinal velocities at the surface were $\overline{u} \simeq -0.8\,\mathrm{m\,s^{-1}}$ in the channel and $\overline{u} \simeq -0.8\,\mathrm{m\,s^{-1}}$ on the slope (Figure 4.2a,b). A lateral circulation develops and reverses three times during this period, with lateral velocities peaking on the slope at the end of the ebb ($t = 63.85$ days to $t = 63.90$ days) $\overline{v} \simeq 0.2\,\mathrm{m\,s^{-1}}$ near the bed and $\overline{v} \simeq -0.15\,\mathrm{m\,s^{-1}}$ near the surface (Figure 4.2d). In the channel, the salinity field was nearly homogeneous at the beginning of the survey, with partial stratification developing through the second half of the ebb (top to bottom density difference at the end of the ebb was $\Delta\rho \simeq 3\,\mathrm{kg\,m^{-3}}$) and vanishing progressively during the flood back to a nearly homogeneous salinity field at the end of the survey (Figure 4.2e). The salinity on the slope follows closely, except that the stratification during the ebb is weaker (top to bottom density difference at the end of the ebb was $\Delta\rho \simeq 2\,\mathrm{kg\,m^{-3}}$) than in the channel (Figure 4.2f).

Similarly to the lateral circulation, the vertical shear $\partial u/\partial z$ on the slope displays significant intratidal variability during the ebb: it increases at the beginning of the ebb from $t = 63.70$ days to $t = 63.77$ days as the tide is accelerating (Figure 4.2b), but decreases shortly after, from $t = 63.77$ days to $t = 63.79$ days, just as the circulation on the slope reverses ($\overline{v} > 0$ near the surface and $\overline{v} < 0$ near the bed, Figure 4.2d). It increases again toward the end of the ebb between $t = 63.80$ days and $t = 63.85$ days when the circulation on the slope reverses again ($\overline{v} < 0$ near the surface and $\overline{v} > 0$ near the bed, Figure 4.2d), even

though the flow is decelerating and the vertical shear $\partial u/\partial z$ is decreasing in the channel (Figure 4.2a).

To summarize, these observed mean velocities and salinity profiles highlight important differences between the slope and the channel. In particular, the vertical shear $\partial u/\partial z$ and density gradient $\partial \rho/\partial z$ display more intratidal variability on the slope than in the channel, especially during the ebb.

4.2 Turbulence observations

TKE shear production

The Reynolds stress profiles $\overline{u'w'}(z,t)$ and $\overline{v'w'}(z,t)$ are estimated using the beam velocities variance method introduced by Lohrmann et al. (1990). As mentioned in the previous section, we use 15-min averages in the channel and 21-min averages on the slope to compute the Reynolds averages. Following Stacey et al. (1999a), we evaluate the standard error in these Reynolds stress estimates to be $7.5\,\mathrm{cm^2\,s^{-2}}$ in the channel and $6.4\,\mathrm{cm^2\,s^{-2}}$ on the slope. The signal to noise ratio of the transverse Reynolds stress component $\overline{v'w'}$ was too small to be reliably used in this analysis and from here on we focus exclusively on the component $\overline{u'w'}$ aligned with the primary flow direction. To further reduce the noise, we filter the Reynolds stress profiles with a moving-average with window size $\Delta t = 45\,\mathrm{min} \times \Delta z = 2.5\,\mathrm{m}$ in the channel and $\Delta t = 60\,\mathrm{min} \times \Delta z = 2.25\,\mathrm{m}$ on the slope. A subset of $\overline{u'w'}(z,t)$ during the 5 March 2009 transect survey is presented in Figure 4.3a,b. As expected, we find the Reynolds stress $\overline{u'w'}$ to be of opposite sign compared to the mean primary flow velocity $\overline{u}$ ($\overline{u'w'} < 0$ and $\overline{u} > 0$ during the ebb; $\overline{u'w'} > 0$ and $\overline{u} < 0$ during the flood). During most of the record, the Reynolds stress magnitude $\left|\overline{u'w'}\right|$ is larger near the bed ($\left|\overline{u'w'}\right| \simeq 7\,\mathrm{cm^2\,s^{-2}}$ in the channel and $\left|\overline{u'w'}\right| \simeq 5\,\mathrm{cm^2\,s^{-2}}$ on the slope during peak ebb), except late in the ebb on the slope, when $\left|\overline{u'w'}\right|$ becomes larger ($\left|\overline{u'w'}\right| \simeq 5\,\mathrm{cm^2\,s^{-2}}$) halfway up the water column (Figure 4.3b, $t = 63.85\,\mathrm{days}$).

To estimate the TKE shear production:

$$P(z,t) = -\overline{u'w'}\frac{\partial \overline{u}}{\partial z} - \overline{v'w'}\frac{\partial \overline{v}}{\partial z} \tag{4.2}$$

we assume the eddy viscosity ν_t to be isotropic in the horizontal plane:

$$\nu_t = -\frac{\overline{u'w'}}{\partial \overline{u}/\partial z} = -\frac{\overline{v'w'}}{\partial \overline{v}/\partial z} \tag{4.3}$$

and substitute (4.3) in (4.4) to estimate the shear production P based on $\overline{u'w'}$, $\partial \overline{u}/\partial z$ and $\partial \overline{v}/\partial z$ only:

$$P(z,t) = -\overline{u'w'}\frac{\partial \overline{u}}{\partial z}\left[1 + \left(\frac{\partial \overline{v}/\partial z}{\partial \overline{u}/\partial z}\right)^2\right] \tag{4.4}$$

The mean vertical velocity gradients $\partial\overline{u}/\partial z$ and $\partial\overline{v}/\partial z$ are processed with a fifth-order spline operator to reduce the noise before substitution in (4.4). A subset of the resulting shear production profiles are presented over the same period as the Reynolds stresses in Figure 4.3c,d. Although the fraction in (4.4) results in increased noise especially when the tide reverses around $t = 63.9\,\text{days}$, the TKE shear production profiles $P(z,t)$ are similar to the Reynolds stress profiles $\overline{u'w'}(z,t)$: P is larger near the bed ($P \simeq 0.7\,\text{cm}^2\,\text{s}^{-3}$ in the channel and $P \simeq 0.4\,\text{cm}^2\,\text{s}^{-3}$ on the slope during peak ebb) except for the period late in the ebb when it becomes larger ($P \simeq 0.7\,\text{cm}^2\,\text{s}^{-3}$) in the upper half of the water column on the slope (Figure 4.3d, $t = 63.85\,\text{days}$). These results show that TKE shear production P in the channel is localized in the bottom boundary layer throughout the tidal cycle. On the slope, which defines the interface between channel and shoal, TKE shear production P is also localized in the bottom boundary layer for most of the tidal cycle, except late in the ebb when stronger vertical shears $\partial\overline{u}/\partial z$ and $\partial\overline{v}/\partial z$ develop in the upper half of the water column (Figure 4.2b,d).

To further investigate the contribution of bed friction to turbulence dynamics at the shoal-channel interface, we compare the observed depth-averaged TKE shear production $\langle P\rangle$ to the bottom-drag power $C_D\,|\langle\overline{u}\rangle|^3/H$. The bottom-drag power is a simple scaling for $\langle P\rangle$ in an unstratified channel flow: integrating shear production by part over depth yields:

$$\langle P\rangle = \frac{1}{H}\int_0^H -\overline{u'w'}\frac{\partial\overline{u}}{\partial z}dz = -\frac{1}{H}\left[\,\overline{u}\overline{u'w'}\,\right]_0^H + \frac{1}{H}\int_0^H \overline{u}\frac{\partial\overline{u'w'}}{\partial z}dz \tag{4.5}$$

which can then be simplified by assuming no surface stress:

$$\overline{u'w'}(z=H) = 0 \tag{4.6}$$

and a linear Reynolds stress profile combined with a quadratic drag law:

$$\frac{\partial\overline{u'w'}}{\partial z} = \frac{u*\,|u*|}{H} = \frac{C_D\,\langle\overline{u}\rangle\,|\langle\overline{u}\rangle|}{H} \tag{4.7}$$

Substituting (4.6) and (4.7) in (4.5) yields then:

$$\langle P\rangle = \frac{C_D\,\langle\overline{u}\rangle^2\,|\langle\overline{u}\rangle|}{H} = \frac{C_D\,|\langle\overline{u}\rangle|^3}{H} \tag{4.8}$$

Over the nine-day record available, we find the estimates of depth-averaged TKE shear production $\langle P\rangle$ and the bottom-drag power $C_D\,|\langle\overline{u}\rangle|^3/H$ to be strongly correlated both in the channel and on the slope (Table 4.1 and Figure 4.4), which supports the hypothesis that bed friction is the main process generating turbulence in this system (we blanked the periods when the wind speed was greater than $5\,\text{m}\,\text{s}^{-1}$ to minimize the risks of wave-contamination, although this had only a small impact on the correlation and drag coefficients in Table 4.1). However, this bottom-drag power scaling fails to reproduce the periods of large shear production $\langle P\rangle$ observed on the slope during some of the ebb tides (Figure 4.4b: highlighted

events), which suggests that turbulence is generated by a process other than bed friction during these periods. These results also show that this late-ebb peak in shear production first identified in Figure 4.3d is not an isolated event as it occurs during five out of the seventeen ebb tides sampled over the nine-day period analyzed in this work. The drag coefficients estimated through a linear regression between $\langle P \rangle$ and $|\langle \overline{u} \rangle|^3 / H$ are smaller than the canonical value $C_D = 2.5 \times 10^{-3}$ by a factor 3 in the channel and 5 on the slope (Table 4.1). This discrepancy can be explained partly by the long averaging periods used to compute the Reynolds averages (15 min in the channel and 21 min on the slope) and the moving average applied to Reynolds stresses to further reduce noise, which both act to smooth observations and therefore lead to underestimated Reynolds stresses and TKE shear production. Different bed properties at the location of the experiment might also contribute to this discrepancy.

TKE dissipation Rate

The TKE dissipation rate profiles $\epsilon(z,t)$ in the channel and on the slope are estimated following the structure function method presented by Wiles et al. (2006): the second order structure function of the ADCP along-beam velocities $D(z,r) = \overline{(u'(z) - u'(z+r))^2}$ is fitted to a model derived from Taylor's cascade theory:

$$D(z,r) = N + C_v^2 \epsilon^{2/3} r^{2/3} \tag{4.9}$$

where N is an offset due to uncertainty in the velocity measurements and $C_v^2 = 2.1$ is an empirical constant used in radar meteorology and adopted by Wiles et al. (2006). Similarly to the TKE shear production estimates, we used 15-min bins in the channel and 21-min bins on the slope to compute Reynolds averages, as well as vertical ranges $1\,\mathrm{m} \leq r \leq 3\,\mathrm{m}$ in the channel and $0.5\,\mathrm{m} \leq r \leq 2\,\mathrm{m}$ on the slope to fit the structure function $D(z,r)$ to the theoretical model (4.9). The lower bounds are set by twice the ADCP bin height because velocity measurements from adjacent bins are not independent, as explained in Wiles et al. 2006. Different values for the upper bounds were tested, ranging from 2 m to 5 m in the channel and from 1 m to 2.5 m on the slope. The upper bound values were selected qualitatively within these ranges: large enough to reduce noise but small enough to preserve vertical structure. For each time ensemble, this method yields a vertical profile of dissipation rate $\epsilon(z)$ for each of the four ADCP beams, which we logarithmically averaged to derive a single estimated profile of TKE dissipation rate. Finally, these dissipation rate profiles are multiplied by an empirical constant factor 1/0.68 used by Wiles et al. (2006) to match microstructure profiler measurements. Similarly to Wiles et al. (2006), our dissipation rate estimates of the upstream-facing ADCP beam were the largest of the four beams, while the estimates of the downstream-facing beam were the smallest. In stratified and partially-stratified flows additional constraints are imposed on this technique because the theoretical model (4.9) applies to turbulent motions in unstratified flows and for length scales r in the inertial subrange. More specifically, when density stratification is present, the upper

bound of the inertial subrange is set by the smallest of the following length scales: the water depth H or the Ozmidov scale $l_O = (\epsilon/N^3)^{1/2}$ where $N = [-(g/\rho)(\partial\rho/\partial z)]^{1/2}$ is the buoyancy frequency. The Ozmidov length scale can be thought of as the length scale at which buoyancy effects become comparable to inertia effects. Therefore, the vertical range used to fit the structure function $D(z,r)$ to the model (4.9) must not extend close to or beyond the water depth H or the Ozmidov scale l_O, i.e. $l_K \ll r \ll \min(H, l_O)$ where l_K is the Kolmogorov length scale. In this case, we combined the shear production estimates from the moored ADCPs with the density profiles from the 5 March 2009 transect survey to derive a similar length scale based on the TKE shear production P instead of the TKE dissipation rate ϵ:

$$l_N = \left(\frac{P}{N^3}\right)^{1/2} \tag{4.10}$$

as suggested in Stacey et al. (1999b).

Contours of the production-based Ozmidov scale l_N are presented during the period of the 5 March 2009 transect survey on Figure 4.5a,b. In the channel, this length scale remains greater than the mean channel depth $l_N > 15\,\mathrm{m}$ throughout the period sampled, which suggests that turbulence there is not affected by density stratification at the length scales $1\,\mathrm{m} \leq r \leq 3\,\mathrm{m}$ used to fit the structure function $D(z,r)$ to the model (4.9). On the slope, l_N drops below 5 m near the surface at the beginning of the flood (Figure 4.5b), and the range $0.5\,\mathrm{m} \leq r \leq 2\,\mathrm{m}$ used to fit the structure function $D(z,r)$ to the model (4.9) might not be appropriate at this period of the tidal cycle. Consequently, the structure function method is expected to yield reasonnable estimates of TKE shear production in this partially-stratified system except on the slope at the beginning of the flood. However, this issue does not affect the conclusions reached in this study as most of the following discussion focuses on the ebb tide.

The profiles of the TKE dissipation rates ϵ are presented during the same period on Figure 4.5a,b. In the channel, dissipation rates are maximum $\epsilon \simeq 0.1\,\mathrm{cm^2\,s^{-3}}$ during peak ebb and flood ($t \simeq 63.80\,\mathrm{days}$ and $t \simeq 64.05\,\mathrm{days}$) and minimum $\epsilon \simeq 0.03\,\mathrm{cm^2\,s^{-3}}$ at low water ($t \simeq 63.90\,\mathrm{days}$). On the slope, dissipation rates are maximum $\epsilon \simeq 0.15\,\mathrm{cm^2\,s^{-3}}$ late in the ebb ($t \simeq 63.85\,\mathrm{days}$) and minimum $\epsilon \simeq 0.03\,\mathrm{cm^2\,s^{-3}}$ early in the flood ($t \simeq 64.0\,\mathrm{days}$). Similarly to the shear production estimates presented in the previous section, these results highlight the late ebb as the period of peak turbulent dissipation on the slope.

The depth-averaged TKE dissipation rates $\langle\epsilon\rangle$ also compare favorably to the bottom drag power $C_D\,|\langle\overline{u}\rangle|^3/H$ over the nine-day record (Table 4.1 and Figure 4.6). As for the shear production, the periods when the wind speed was greater than $5\,\mathrm{m\,s^{-1}}$ were blanked. The bottom-drag scaling also failed here to reproduce the late-ebb peak in dissipation rate $\langle\epsilon\rangle$ on the slope (Figure 4.6b: highlighted events), which provides an additional evidence that a mechanism different than bed friction is driving turbulence dynamics at the shoal-channel interface during these periods. Four other late-ebb peaks in dissipation rate similar to the one identified in Figure 4.5b were observed throughout the nine-day period analyzed in this work, which provides additional evidences that this event is not isolated. The correlation and

drag coefficients estimated through a linear regression between $\langle\epsilon\rangle$ and $|\langle\overline{u}\rangle|^3/H$ are smaller than the canonical value $C_D = 2.5 \times 10^{-3}$ and those estimated from the shear production $\langle P\rangle$ (Table 4.1). These differences can be partially explained by the fact that dissipation rates might be further underestimated in this case than in Wiles et al. (2006) (therefore requiring a correction factor greater than 1/0.68 mentioned above), but also by the fact that in steady and homogeneous stratified turbulence not all TKE produced is dissipated as heat by viscosity since a fraction is converted to potential energy through mixing of the density field, i.e. $\langle\epsilon\rangle \leq \langle P\rangle$. This fraction is quantified by the buoyancy flux B.

Buoyancy flux

The buoyancy flux B introduced in (1.12) was estimated indirectly from the Reynolds stress $\overline{u'w'}$ because direct measurements of $\overline{\rho'w'}$ were not available. The vertical eddy diffusivity K_ρ is assumed equal to the vertical eddy viscosity ν_t:

$$K_\rho = \frac{-\overline{\rho'w'}}{\partial\overline{\rho}/\partial z} = \nu_t = \frac{-\overline{u'w'}}{\partial\overline{u}/\partial z} \tag{4.11}$$

which allows us to estimate the buoyancy flux B as:

$$B = -\frac{g}{\rho_0}\overline{\rho'w'} = -\frac{g}{\rho_0}\left(\frac{\overline{u'w'}}{\partial\overline{u}/\partial z}\right)\frac{\partial\overline{\rho}}{\partial z} = \left(\frac{\overline{u'w'}}{\partial\overline{u}/\partial z}\right)N^2 \tag{4.12}$$

where N^2 is the squared buoyancy frequency defined in section 1.1. The assumption (4.11) is also called the Reynolds analogy. In stably stratified flows, the turbulent Prandtl number is typically greater than one $\mathrm{Pr_t} = \nu_t/K_\rho > 1$ (Kundu and Cohen 2008), and as a result (4.12) can be interpreted as an upper-bound for B.

Vertical profiles of the buoyancy flux were estimated from density profiles collected during the 05 March 2009 transect survey and Reynolds stress and velocity profiles from the channel and slope mid ADCPs. The results are presented on Figure 4.7. In the channel, the buoyancy flux is negative during the ebb (sink of TKE) and positive during the flood (source of TKE). This pattern is consistent with the tidal straining mechanism previously discussed by Rippeth et al. (2001) and Stacey et al. (2012): during the ebb, the faster flow near the surface advects freshwater from up-estuary quicker than near the bottom which increases stable stratification and provides a sink for TKE; during the flood denser water is advected faster near the surface than near the bed which can drive unstable convection and provide a source of TKE. Such asymmetry is not observed on the slope (Figure 4.7b) where the buoyancy flux is negative throughout the period sampled. It also appears to be strongest late in the ebb and early in the flood, when the vertical density gradient is the strongest. The strong buoyancy flux late in the ebb (period $t \simeq 63.85$days) is a result of the strong TKE shear production events identified in the previous two subsections and shows that these events have important implications for vertical mixing on the slope.

To summarize, these observations of Reynolds stresses $\overline{u'w'}$, TKE shear production P, TKE dissipation rate ϵ and buoyancy flux B at the shoal-channel interface in partially-stratified conditions confirm the leading role of bed friction in generating turbulence, but also reveal the dominant contribution of mid-water column shear $\partial\overline{u}/\partial z$ and $\partial\overline{v}/\partial z$ at the end of the ebb. During this period, the dominant flow feature at the shoal-channel interface is the transverse circulation developing on the slope (Figure 4.2d, 63.85 days $\leq t \leq$ 63.90 days), which effects on vertical mixing are still poorly characterized. The following section proposes a theoretical framework to quantify and compare these effects.

4.3 Effects of the Lateral Circulation on Stability

Framework

In stratified and partially-stratified flows, the gradient Richardson number $\mathrm{Ri_g}$ introduced in (1.13) is the dimensionless number commonly used to assess the stability. The direction and magnitude of the lateral circulation is quantified by the streamwise vorticity $\omega_x = \partial\overline{w}/\partial y - \partial\overline{v}/\partial z$ which can be simplified to $\omega_x \simeq -\partial\overline{v}/\partial z$ in this shallow system because the characteristic horizontal length scale is much greater than the characteristic vertical length scale, as previously discussed in section 3.3. To assess how the lateral circulation affects the stability of the water column, the contributions of ω_x to changes in the gradient Richardson number $\partial\mathrm{Ri_g}/\partial t$ must be identified. Taking the time derivative of (1.13) yields:

$$\frac{\partial \mathrm{Ri_g}}{\partial t} = \frac{1}{S^2}\left[-\frac{g}{\rho_0}\frac{\partial}{\partial t}\left(\frac{\partial\overline{\rho}}{\partial z}\right) - 2\mathrm{Ri_g}\frac{\partial\overline{u}}{\partial z}\frac{\partial}{\partial t}\left(\frac{\partial\overline{u}}{\partial z}\right) - 2\mathrm{Ri_g}\frac{\partial\overline{v}}{\partial z}\frac{\partial}{\partial t}\left(\frac{\partial\overline{v}}{\partial z}\right)\right] \tag{4.13}$$

in which ω_x can be readily substituted:

$$\frac{\partial \mathrm{Ri_g}}{\partial t} = \frac{1}{S^2}\left[-\frac{g}{\rho_0}\frac{\partial}{\partial t}\left(\frac{\partial\overline{\rho}}{\partial z}\right) - 2\mathrm{Ri_g}\frac{\partial\overline{u}}{\partial z}\frac{\partial}{\partial t}\left(\frac{\partial\overline{u}}{\partial z}\right) - 2\mathrm{Ri_g}\omega_x\frac{\partial\omega_x}{\partial t}\right] \tag{4.14}$$

The two time derivatives on the right hand side (r.h.s.) of (4.14) can be related to vorticity ω_x by taking the vertical derivative $\partial/\partial z$ of the conservation of mass and longitudinal momentum equations. In an incompressible flow ($\mathrm{div}(\underline{u}) = 0$) the Reynolds-averaged conservation of mass writes as an advection-diffusion equation:

$$\frac{\partial\overline{\rho}}{\partial t} + \overline{u}\frac{\partial\overline{\rho}}{\partial x} + \overline{v}\frac{\partial\overline{\rho}}{\partial y} + \overline{w}\frac{\partial\overline{\rho}}{\partial z} = \frac{\partial}{\partial z}\left(K_t\frac{\partial\overline{\rho}}{\partial z}\right) \tag{4.15}$$

where K_t is the vertical eddy diffusivity. Under the Boussinesq approximation, the Reynolds-averaged longitudinal momentum equation writes:

$$\frac{\partial\overline{u}}{\partial t} + \overline{u}\frac{\partial\overline{u}}{\partial x} + \overline{v}\frac{\partial\overline{u}}{\partial y} + \overline{w}\frac{\partial\overline{u}}{\partial z} = -\frac{1}{\rho_0}\frac{\partial\overline{p}}{\partial x} + f\overline{v} + \frac{\partial}{\partial z}\left(\nu_t\frac{\partial\overline{u}}{\partial z}\right) \tag{4.16}$$

where $\overline{p}$ is the pressure, $f \simeq 8.9 \times 10^{-5}\,\mathrm{s}^{-1}$ is the Coriolis frequency at the latitude of the field site (37°34′35″N), and ν_t is the vertical eddy viscosity. Taking the vertical derivative $\partial/\partial z$ of (4.15) and (4.16) yields two equations:

$$\frac{\partial}{\partial t}\left(\frac{\partial \overline{\rho}}{\partial z}\right) = -\frac{\partial}{\partial z}\left(\overline{u}\frac{\partial \overline{\rho}}{\partial x}\right) - \frac{\partial}{\partial z}\left(\overline{v}\frac{\partial \overline{\rho}}{\partial y}\right) - \frac{\partial}{\partial z}\left(\overline{w}\frac{\partial \overline{\rho}}{\partial z}\right) + \frac{\partial^2}{\partial z^2}\left(K_t\frac{\partial \overline{\rho}}{\partial z}\right) \tag{4.17}$$

$$\frac{\partial}{\partial t}\left(\frac{\partial \overline{u}}{\partial z}\right) = -\frac{\partial}{\partial z}\left(\overline{u}\frac{\partial \overline{u}}{\partial x}\right) - \frac{\partial}{\partial z}\left(\overline{v}\frac{\partial \overline{u}}{\partial y}\right) - \frac{\partial}{\partial z}\left(\overline{w}\frac{\partial \overline{u}}{\partial z}\right) - \frac{1}{\rho_0}\frac{\partial}{\partial z}\left(\frac{\partial \overline{p}}{\partial x}\right) + f\frac{\partial \overline{v}}{\partial z} + \frac{\partial^2}{\partial z^2}\left(\nu_t\frac{\partial \overline{u}}{\partial z}\right) \tag{4.18}$$

in which the vorticity $\omega_x \simeq -\partial \overline{v}/\partial z$ can be isolated:

$$\frac{\partial}{\partial t}\left(\frac{\partial \overline{\rho}}{\partial z}\right) = \omega_x\frac{\partial \overline{\rho}}{\partial y} + R_\rho \tag{4.19}$$

$$\frac{\partial}{\partial t}\left(\frac{\partial \overline{u}}{\partial z}\right) = \omega_x\frac{\partial \overline{u}}{\partial y} - f\omega_x + R_u \tag{4.20}$$

where R_ρ and R_u are the remainder terms not involving the vorticity:

$$R_\rho = -\frac{\partial}{\partial z}\left(\overline{u}\frac{\partial \overline{\rho}}{\partial x}\right) - \overline{v}\frac{\partial}{\partial z}\left(\frac{\partial \overline{\rho}}{\partial y}\right) - \frac{\partial}{\partial z}\left(\overline{w}\frac{\partial \overline{\rho}}{\partial z}\right) + \frac{\partial^2}{\partial z^2}\left(K_t\frac{\partial \overline{\rho}}{\partial z}\right) \tag{4.21}$$

$$R_u = -\frac{\partial}{\partial z}\left(\overline{u}\frac{\partial \overline{u}}{\partial x}\right) - \overline{v}\frac{\partial}{\partial z}\left(\frac{\partial \overline{u}}{\partial y}\right) - \frac{\partial}{\partial z}\left(\overline{w}\frac{\partial \overline{u}}{\partial z}\right) - \frac{1}{\rho_0}\frac{\partial}{\partial z}\left(\frac{\partial \overline{p}}{\partial x}\right) + \frac{\partial^2}{\partial z^2}\left(\nu_t\frac{\partial \overline{u}}{\partial z}\right) \tag{4.22}$$

Finally, substituting (4.19) and (4.20) in (4.14) leads to

$$\frac{\partial \mathrm{Ri_g}}{\partial t} = \frac{1}{S^2}\left[\underbrace{\omega_x\left(-\frac{g}{\rho_0}\frac{\partial \overline{\rho}}{\partial y}\right)}_{density\ straining} + \underbrace{\omega_x\left(-2\mathrm{Ri_g}\frac{\partial \overline{u}}{\partial z}\frac{\partial \overline{u}}{\partial y}\right)}_{shear\ straining} + \underbrace{\omega_x\left(2\mathrm{Ri_g}\frac{\partial \overline{u}}{\partial z}f\right)}_{Coriolis} + \underbrace{\omega_x\left(-2\mathrm{Ri_g}\frac{\partial \omega_x}{\partial t}\right)}_{unsteadiness} + R\right] \tag{4.23}$$

with:

$$R = -\frac{g}{\rho_0}R_\rho - 2\mathrm{Ri_g}\frac{\partial \overline{u}}{\partial z}R_u \tag{4.24}$$

The first two terms on the r.h.s. of (4.23) represent the straining of lateral density and velocity gradients $\partial \overline{\rho}/\partial y$ and $\partial \overline{u}/\partial y$ by the lateral circulation. We expect these two terms to be important in this system, especially during the ebb when the lateral gradients at the shoal-channel interface $\partial \overline{\rho}/\partial y \leq 0$ (salinity lower in the channel than on the shoal) and $\partial \overline{u}/\partial y \geq 0$ (flow faster in the channel than on the shoal) are the strongest. The Coriolis term on the r.h.s. of (4.23) represents the conversion of shear in the lateral velocity component $\partial \overline{v}/\partial z$ to vertical shear in the longitudinal (primary) velocity component $\partial \overline{u}/\partial z$ by Earth's rotation. Finally, the unsteadiness term represents the effects of the temporal variations of

the lateral circulation: an accelerating circulation corresponds to an increasing magnitude of the vertical shear in the lateral velocity component $|\partial\overline{v}/\partial z|$, which then acts to decrease $\mathrm{Ri_g}$.

It is important to note that the terms and mechanisms associated with the lateral circulation and described in the previous paragraph do not act alone in controlling water column stability and some of the processes collapsed in the remainder term R might be equally or more important, such as vertical turbulent mixing generated by bed friction and the straining of the longitudinal density gradient $\partial\overline{\rho}/\partial x$ analyzed by Simpson et al. (1990) for instance. However discussing the role of these other processes is beyond the scope of this work. A method to assess the effects of the lateral circulation and the associated mechanisms independently of the remainder R is proposed in section 4.3.

Special Cases

To better illustrate the processes at play in this framework, two simple cases can be considered. The first case is a steady ($\partial\omega_x/\partial t = 0$), density-driven circulation in a non-rotating system ($f = 0$), illustrated in Figure 4.8a. In such case, the lateral circulation affects stability through the density and shear straining terms only:

$$\frac{\partial \mathrm{Ri_g}}{\partial t} = \frac{1}{S^2}\left[\underbrace{\omega_x\left(-\frac{g}{\rho_0}\frac{\partial\overline{\rho}}{\partial y}\right)}_{density\ straining} + \underbrace{\omega_x\left(-2\mathrm{Ri_g}\frac{\partial\overline{u}}{\partial z}\frac{\partial\overline{u}}{\partial y}\right)}_{shear\ straining} + R\right] \tag{4.25}$$

Consequently, the lateral circulation will have a destabilizing effect if:

$$\underbrace{\omega_x\left(-\frac{g}{\rho_0}\frac{\partial\overline{\rho}}{\partial y}\right)}_{density\ straining} < \underbrace{\omega_x\left(2\mathrm{Ri_g}\frac{\partial\overline{u}}{\partial z}\frac{\partial\overline{u}}{\partial y}\right)}_{shear\ straining} \tag{4.26}$$

In other words, the lateral circulation will act to decrease $\mathrm{Ri_g}$ if the conversion of lateral shear $\partial\overline{u}/\partial y$ to vertical shear $\partial\overline{u}/\partial z$ (shear straining term) occurs faster than the conversion of lateral density gradient $\partial\overline{\rho}/\partial y$ to density stratification $\partial\overline{\rho}/\partial z$ (density straining term). Furthermore, we can assume that $\omega_x(\partial\overline{\rho}/\partial y) < 0$ since in this case denser water always flows under lighter water, and write (4.26) in a dimensionless form:

$$\frac{1}{2\mathrm{Ri_g}} < \frac{\frac{\partial\overline{u}}{\partial z}\frac{\partial\overline{u}}{\partial y}}{-\frac{g}{\rho_0}\frac{\partial\overline{\rho}}{\partial y}} \tag{4.27}$$

In the situation illustrated in Figure 4.8a, the lateral circulation acts to increase vertical shear $\partial\overline{u}/\partial z$ on the slope by advecting slower shoal water under faster channel water. But the circulation also acts to increase density stratification $\partial\overline{\rho}/\partial z$ on the slope by advecting denser shoal water under lighter channel water. The density and shear straining mechanisms

therefore have competing effects on $\mathrm{Ri_g}$ and the destabilizing influence of shear straining will dominate in this example if (4.27) is verified.

The second case is a steady ($\partial\omega_x/\partial t = 0$), rotation-driven circulation without lateral density gradient ($\partial\overline{\rho}/\partial y = 0$), illustrated in Figure 4.8b. In such case, the lateral circulation affects stability through the shear straining and Coriolis terms only:

$$\frac{\partial \mathrm{Ri_g}}{\partial t} = \frac{1}{S^2}\left[\underbrace{\omega_x\left(-2\mathrm{Ri_g}\frac{\partial\overline{u}}{\partial z}\frac{\partial\overline{u}}{\partial y}\right)}_{shear\ straining} + \underbrace{\omega_x\left(2\mathrm{Ri_g}\frac{\partial\overline{u}}{\partial z}f\right)}_{Coriolis} + R\right] \tag{4.28}$$

from which it can be inferred that the lateral circulation will have a destabilizing effect if:

$$\underbrace{\omega_x\left(2\mathrm{Ri_g}\frac{\partial\overline{u}}{\partial z}f\right)}_{Coriolis} < \underbrace{\omega_x\left(2\mathrm{Ri_g}\frac{\partial\overline{u}}{\partial z}\frac{\partial\overline{u}}{\partial y}\right)}_{shear\ straining} \tag{4.29}$$

In this case, the lateral circulation will act to decrease $\mathrm{Ri_g}$ if the conversion of lateral shear $\partial\overline{u}/\partial y$ to vertical shear $\partial\overline{u}/\partial z$ (shear straining term) occurs faster than the conversion of the transverse component of the shear $\partial\overline{v}/\partial z$ to the longitudinal component of the shear $\partial\overline{u}/\partial z$ by rotation (Coriolis term). Furthermore, we can assume in this case that $\omega_x(\partial\overline{u}/\partial z) > 0$ in the Northern hemisphere since rotation acts to deflect flows toward the right, and write (4.29) in a dimensionless form:

$$f < \frac{\partial\overline{u}}{\partial y} \tag{4.30}$$

The example on Figure 4.8b illustrate an example of the opposite case: $f > 0 > \partial\overline{u}/\partial y$. In this example, the rotation-driven lateral circulation advects faster channel water below slower shoal water, which acts to reduce the vertical shear $\partial\overline{u}/\partial z$ on the slope and therefore increase $\mathrm{Ri_g}$.

Although these two limiting cases allow for consideration of specific thresholds, we've shown in chapter 3 that lateral density gradients, unsteadiness and Coriolis all contribute to the dynamics of the lateral circulation in this system, so that all four terms in (4.23) need to be accounted for. In the following discussion, this framework is applied to the observations from South San Francisco Bay in order to assess the effects of the lateral circulation on turbulence dynamics at this shoal-channel interface.

Discussion of observations

As mentioned in the previous sections, the lateral circulation is the dominant flow feature on the slope during the late ebb period (Figure 4.2d, 63.85 days $\leq t \leq$ 63.90 days). This circulation advects slower water from the shoal below faster water from the channel and as a result increases the vertical shear $\partial\overline{u}/\partial z$ (shear straining term in equation 4.23), but it

also increases the density stratification $\partial\overline{\rho}/\partial z$ as salinity is higher over the shoal than at the surface in the channel (density straining term in equation 4.23). In such a situation (Figure 4.9), these two mechanisms have therefore competing effects on the stability. To determine the net effect of this late-ebb circulation on $\mathrm{Ri_g}$, and assess if it really impacts stability, the four terms identified in (4.23) and associated with the circulation can be compared directly to the residual term. However, this residual term is hard to estimate in practice because of the spatial derivatives and eddy viscosities and diffusivities involved in (4.24), and we propose here an alternate approach. Four timescales characteristic of the four processes identified in (4.23) can be estimated and compared:

$$\tau_\rho = \frac{S^2}{\omega_x \left(-\frac{g}{\rho_0}\frac{\partial\overline{\rho}}{\partial y}\right)} \tag{4.31}$$

$$\tau_u = \frac{S^2}{\omega_x \left(-2\mathrm{Ri_g}\frac{\partial\overline{u}}{\partial z}\frac{\partial\overline{u}}{\partial y}\right)} \tag{4.32}$$

$$\tau_f = \frac{S^2}{\omega_x \left(2\mathrm{Ri_g}\frac{\partial\overline{u}}{\partial z}f\right)} \tag{4.33}$$

$$\tau_t = \frac{S^2}{\omega_x \left(-2\mathrm{Ri_g}\frac{\partial\omega_x}{\partial t}\right)} \tag{4.34}$$

These timescales are defined positive if the associated mechanism acts to increase $\mathrm{Ri_g}$ (stabilizing effect) or negative if it acts to decrease $\mathrm{Ri_g}$ (destabilizing effect). Furthermore, their magnitude provides a way to estimate the strength of their associated mechanisms: a small timescale (e.g. $\tau \ll T_{M2}/2 \simeq 6.2\,\mathrm{hours}$) suggests that the associated mechanism is important whereas a large timescale (e.g. $\tau \gg T_{M2}/2$) suggests that the associated mechanism acts too slowly to impact stability over the duration of a single tide. In essence, this approach is similar to comparing the four terms associated with the lateral circulation in (4.23) with the term $\partial\mathrm{Ri_g}/\partial t$ instead of the remainder R and assuming that in partially-stratified shoal-channel estuaries, the gradient Richardson number $\mathrm{Ri_g}$ is typically close to one, while the timescale characteristic of its fluctuations is close to the duration of a tide, i.e. half the M2 tidal period $T_{M2}/2$.

These four timescales are estimated at the middle of the slope from the velocity and density profiles collected during the 5 March transect survey. More precisely, the vertical gradients $\partial\overline{u}/\partial z$, $\partial\overline{v}/\partial z$ and $\partial\overline{\rho}/\partial z$ are estimated at the middle of the slope with centered finite differences. The lateral gradients $\partial\overline{u}/\partial y$ and $\partial\overline{\rho}/\partial y$ are estimated at the same location with centered finite differences of the velocity and density profiles in the channel and on the shoal:

$$\left(\frac{\partial\overline{u}}{\partial y}\right)_{slope}(z,t) \simeq \frac{\overline{u}_{channel}(z,t) - \overline{u}_{shoal}(z,t)}{\Delta y} \tag{4.35}$$

$$\left(\frac{\partial\overline{\rho}}{\partial y}\right)_{slope}(z,t) \simeq \frac{\overline{\rho}_{channel}(z,t) - \overline{\rho}_{shoal}(z,t)}{\Delta y} \tag{4.36}$$

where $\Delta_y = 800\,\mathrm{m}$. We expect these finite differences to underestimate the lateral gradients because Δ_y is most likely greater than the actual lengthscale characteristic of lateral variations, which is set by the width of the shoal-channel interface $W = \Delta_y/2 = 400\,\mathrm{m}$. Consequently, this method most likely yields upper bounds for the timescales τ_u and τ_ρ, which is not an issue in this case because the timescales τ_ρ, τ_u, τ_f and τ_t are well separated, as described below. To focus on the temporal variability, equations (4.31)-(4.34) were depth-averaged and the results are presented in Figure 4.10b, along with the profiles $\mathrm{Ri_g}(z,t)$ (Figure 4.10a) during the 5 March 2009 transect survey. During the first six transects ($63.72\,\mathrm{days} \leq t \leq 63.82\,\mathrm{days}$), $\mathrm{Ri_g}$ appears to be smaller near the bed (Figure 4.10a), which is consistent with maximal TKE shear production in this region. Only the shear straining mechanism appears to be important during this period as only $\tau_u < T_{M2}/2$ for most of these first six transects. During the late ebb period ($63.85\,\mathrm{days} \leq t \leq 63.90\,\mathrm{days}$), the estimated profiles of $\mathrm{Ri_g}$ suggest that the middle of the water column on the slope is unstable ($\mathrm{Ri_g} < 1/4$) while the near-bed and near-surface region appear to be stably stratified ($\mathrm{Ri_g} > 1/4$). During that same period, only the shear straining and density straining timescales τ_u and τ_ρ are significantly smaller than $T_{M2}/2 \simeq 6.2$ hours, τ_u being negative and τ_ρ positive (Figure 4.10b). Furthermore, $|\tau_u(t = 63.89\,\mathrm{days})| \simeq 0.3\,\mathrm{hours} < |\tau_\rho(t = 63.89\,\mathrm{days})| \simeq 1.2\,\mathrm{hours}$, which suggests that the destabilizing influence of the straining of the lateral shear overcomes the stabilizing influence of the straining of the lateral density gradient by the late-ebb lateral circulation. At the beginning of the flood ($63.99\,\mathrm{days} \leq t \leq 64.01\,\mathrm{days}$), the four timescales become positive and smaller than $T_{M2}/2$, which suggests that the lateral circulation contributes through all four mechanisms to the increase in stratification occurring at this time (Figure 4.10a).

These timescales suggest therefore that the lateral circulation developing on the slope late in the ebb has a net destabilizing effect, by converting the lateral shear at the shoal-channel interface $\partial\overline{u}/\partial y$ to vertical shear $\partial\overline{u}/\partial z$ faster than it converts the lateral density gradient $\partial\overline{\rho}/\partial y$ to stratification $\partial\overline{\rho}/\partial z$. These results support the hypothesis that the lateral circulation is driving the observed peaks of TKE shear production P and dissipation rate ϵ described in sections 4.24.2 and 4.24.2. We expect a similar domination of shear straining in regions of strong lateral shear and weak lateral density gradient, such as areas of sharp bathymetric variations or in the wake of headlands (Farmer et al. 2002) in partially stratified estuaries.

4.4 Modeling Turbulence Dynamics

It was shown in previous sections 4.2 and 4.3 that the lateral circulation has a strong indirect effect on turbulence dynamics at the shoal-channel interface through the destabilizing increase of vertical shear, which results in enhanced TKE shear production P late in the ebb on the slope. To assess the direct effect of the lateral circulation on the TKE equation (4.1) through the lateral advection term $\overline{v}\,(\partial q^2/\partial y)$, knowledge of the TKE q^2 in the channel and on the slope is required. While q^2 has been previously estimated from ADCP

data (Stacey et al. 1999a; Stacey et al. 1999b), the assumptions used in these studies are valid for unstratified channel flows and cannot be used reliably in this system because of the stratification and strong transverse flows. To estimate q^2, we use instead the General Ocean Turbulence Model (GOTM), a water-column (1D) numerical model with state-of the art turbulence closure schemes (Umlauf et al. 2007).

Model parameters

Turbulence at the channel and slope mid moorings are modeled with GOTM: at each location the model is forced with the mean observed profiles of velocities $(\overline{u}(z,t), \overline{v}(z,t))$ from the moored ADCPs and density $\overline{\rho}(z,t)$ from the CTD profiles collected during the 05 March 2009 transect survey. At each timestep, the model uses these mean profiles to solve for various turbulent quantities. The model outputs used are the TKE shear production P for validation and the TKE q^2 for estimating lateral advection of TKE.

The mean observed velocity and density profiles are first pre-processed before forcing the model:

1. **Mapping**: observed mean velocity profiles $(\overline{u}(z,t), \overline{v}(z,t))$ from the moored Ch and SlM ADCPs and observed mean density profiles $\overline{\rho}(z,t)$ from the CTD profiles collected during the 05 March 2009 transect survey are mapped to the same vertical coordinate system, defined by $z = 0$ at the bed at the channel mooring and increasing z in the upward direction.

2. **Splining**: observed mean profiles $(\overline{u}(z,t), \overline{v}(z,t))$ and $\overline{\rho}(z,t)$ are smoothed in the vertical direction using a 5th order spline operator. The vertical gradients of the observed mean profiles, used by the model to estimate TKE shear production P, Richardson Gradient Number $\mathrm{Ri_g}$, are polluted by high wavenumber noise. The spline operator filters out this noise and keeps the large-scale (low wavenumber) vertical gradients intact.

3. **Extrapolation**: observed mean velocity profiles $(\overline{u}(z,t), \overline{v}(z,t))$ do not extend all the way to the bed because of instrument limitations, and therefore the lower part of the bottom boundary layer is not observed (about 1.8 m in the channel and 1.5 m on the slope). However, this region is critical to turbulence dynamics because most of the TKE shear production occurs there, and the observations must then be extrapolated to this near bed region. The velocity profiles are extrapolated with second-order polynomial functions $U(z) = az^2 + bz + c$, where the coefficients a, b and c are defined by the following boundary conditions: $U = 0$ at $z = z_{bed}$ (no-slip at the bed); $U = \overline{u}_{observed}$ and $dU/dz = \partial \overline{u}_{observed}/\partial z$ at $z = z_1$, the height where the first observation is available (continuous velocity profile and vertical gradient).

All the model runs are set up as follow:

1. **Boundary conditions**: no-slip at the bottom, free-slip (no momentum flux) at the surface, no buoyancy flux at the bottom and the surface boundaries.

2. **Discretization**: vertical grid resolution $\Delta z = 1\,\text{cm}$, time step $\Delta t = 10\,\text{s}$. The time stepping scheme is implicit and unconditionally stable. The time step was chosen small enough so as to keep the spin-up time of turbulent quantities small ($< 15\,\text{min}$).

3. **Simulated periods**: the 05 March 2009 ($t = 63.7 - 64.1$ days) transect survey.

In GOTM, vertical turbulent fluxes of momentum $\overline{u'w'}$ and $\overline{v'w'}$ and density $\overline{\rho'w'}$ are computed as diffusive, down-gradient fluxes:

$$\overline{u'w'} = -\nu_t \frac{\partial \overline{u}}{\partial z} \tag{4.37}$$

$$\overline{v'w'} = -\nu_t \frac{\partial \overline{v}}{\partial z} \tag{4.38}$$

$$\overline{\rho'w'} = -\nu_t^B \frac{\partial \overline{\rho}}{\partial z} \tag{4.39}$$

The turbulent diffusivities of momentum ν_t and density ν_t^B are then computed as the products of a dimensionless coefficient called stability function, a velocity scale, typically the square root of TKE q and a lengthscale l:

$$\nu_t = c_\mu q l \tag{4.40}$$

$$\nu_t^B = c'_\mu q l \tag{4.41}$$

The depth and time-varying velocity and length scales $q(z,t)$ and $l(z,t)$ are computed from dynamical equations while the stability functions $c_\mu(z,t)$ and $c'_\mu(z,t)$ are computed from algebraic empirical relations. It is important to note that GOTM is a 1D model and as result it is assumed that velocities $(\overline{u}, \overline{v})$ and turbulent quantities are homogeneous horizontally, or more realistically that the horizontal advection terms in the TKE equation (4.1) are negligible compared to the local shear production P and dissipation rate ϵ. This assumption will be justified a-posteriori in the following subsections.

Comparison of model outputs and observations

Four cases (A-D) were run (Table 4.2), each with a different set of stability function, TKE equation and lengthscale equation, to test the sensitivity of the model to the choice of turbulence closure. The modeled TKE shear production P_{model} is compared to the observation P_{obs} at the channel and slope mid locations in Figures 4.11-4.14. We find that the model is only weakly sensitive to the choice of turbulence closure as P_{model} is almost identical in the four cases.

The modeled shear production P_{model} is about four times larger than the observed value P_{obs}. The smallest P_{model} was found in case C (Figure 4.13) and the largest P_{model} in case

B (Figure 4.12). A few explanations for the discrepancy between the magnitude of P_{model} and P_{obs} can be proposed. First, the observations P_{obs} are likely to under-estimate P by a factor 3 in the channel and 5 on the slope because of the averaging involved in the data processing, as mentioned previously in section 4.2. It is also possible that the model over-estimates P because the shear in the near-bed region is different in reality from the quadratic extrapolation described above, but also because stable stratification damps turbulence more in reality than in the model.

The vertical and temporal structure of P_{model} is reasonably close to the structure of P_{obs}, except for the end of the simulated period ($t > 64.05$ days). In particular, the model reproduces well the evolution of P during the late ebb period on the slope: like the observations, P_{model} displays large values in the upper half of the water column from $t = 63.85$ days to $t = 63.87$ days when the lateral circulation is the strongest.

To summarize, the model reproduces the main features of the turbulence dynamics at the shoal-channel interface, which suggests that the TKE q^2 computed by the model can be used reliably to estimate the lateral advection term of (4.1).

Lateral advection of TKE

Vertical profiles of TKE $q^2(z,t)$ at the channel and slope mid locations are computed for the period of the 05 March 2009 transect survey using the turbulence closure models of case D (Table 4.2). The lateral advection term of the TKE equation (4.1) is estimated on the slope as a finite difference:

$$\overline{v}\frac{\partial q^2}{\partial z}(z,t) \simeq \left(\frac{\overline{v}_{ch}(z,t) + \overline{v}_{slm}(z,t)}{2}\right)\left(\frac{q^2_{ch}(z,t) - q^2_{slm}(z,t)}{\Delta y}\right) \tag{4.42}$$

where $\Delta y = 333\,\mathrm{m}$ is the distance between the channel and slope mid moorings. This approach yields an estimate of the lateral advection term of order $10^{-2}\,\mathrm{cm^2\,s^{-1}}$, smaller then the TKE shear production P by a factor 10-100 (Figure 4.15). This result is consistent with the a priori assumption that horizontal advection is negligible compared to TKE shear production and dissipation rates.

4.5 Summary

Vertical profiles of TKE shear production $P(z,t)$, TKE dissipation rate $\epsilon(z,t)$ and buoyancy flux $B(z,t)$ were estimated at the channel and slope mid location using observations from the moored ADCPs and the CTD profiles performed during the 05 March 2009 transect survey. TKE is generated in the bottom boundary layer as a result of the no-slip condition at the bed, except for occasional bursts of TKE shear production, dissipation rate and buoyancy flux observed on the slope late in the ebb. These events are associated with enhanced vertical shear in the upper half of the water column, away from the bottom boundary.

The connections between these events and the lateral circulation developing at the same period are explored by assessing the effects of the lateral circulation the vertical stability of the flow. It is found in this case that the lateral circulation strains transverse velocity $\partial\overline{u}/\partial y$ and density $\partial\overline{\rho}/\partial y$ gradients and converts them to vertical gradients $\partial\overline{u}/\partial z$ and $\partial\overline{\rho}/\partial z$. The net effect is dominated by the straining of the lateral velocity gradient, such that the lateral circulation has a net destabilizing effect in this system. This result supports the hypothesis that the lateral circulation is responsible for the late ebb intensification of turbulence on the slope.

The role of lateral advection of TKE is explored using a 1D water column numerical model. The model is forced with the observed velocity $(\overline{u}(z,t), \overline{v}(z,t))$ and density profiles $\overline{\rho}(z,t)$ which are then used to compute turbulent quantities. The model is found to reproduce reasonably the main features of the flow at the channel and slope mid locations. The TKE profiles computed by the model are used to estimate the lateral advection term $\overline{v}\,(\partial q^2/\partial y)$ of the TKE equation (4.1), which is found to be 10-100 times smaller than the TKE shear production and TKE dissipation rate.

To conclude, the lateral circulation developing during the ebb at the shoal-channel interface has an indirect impact on turbulence dynamics and vertical mixing on the slope: through the straining of the transverse gradients, it increases vertical shear faster than vertical stratification, such that local TKE shear production is enhanced. However, the direct impact quantified by the lateral advection term is found to be small.

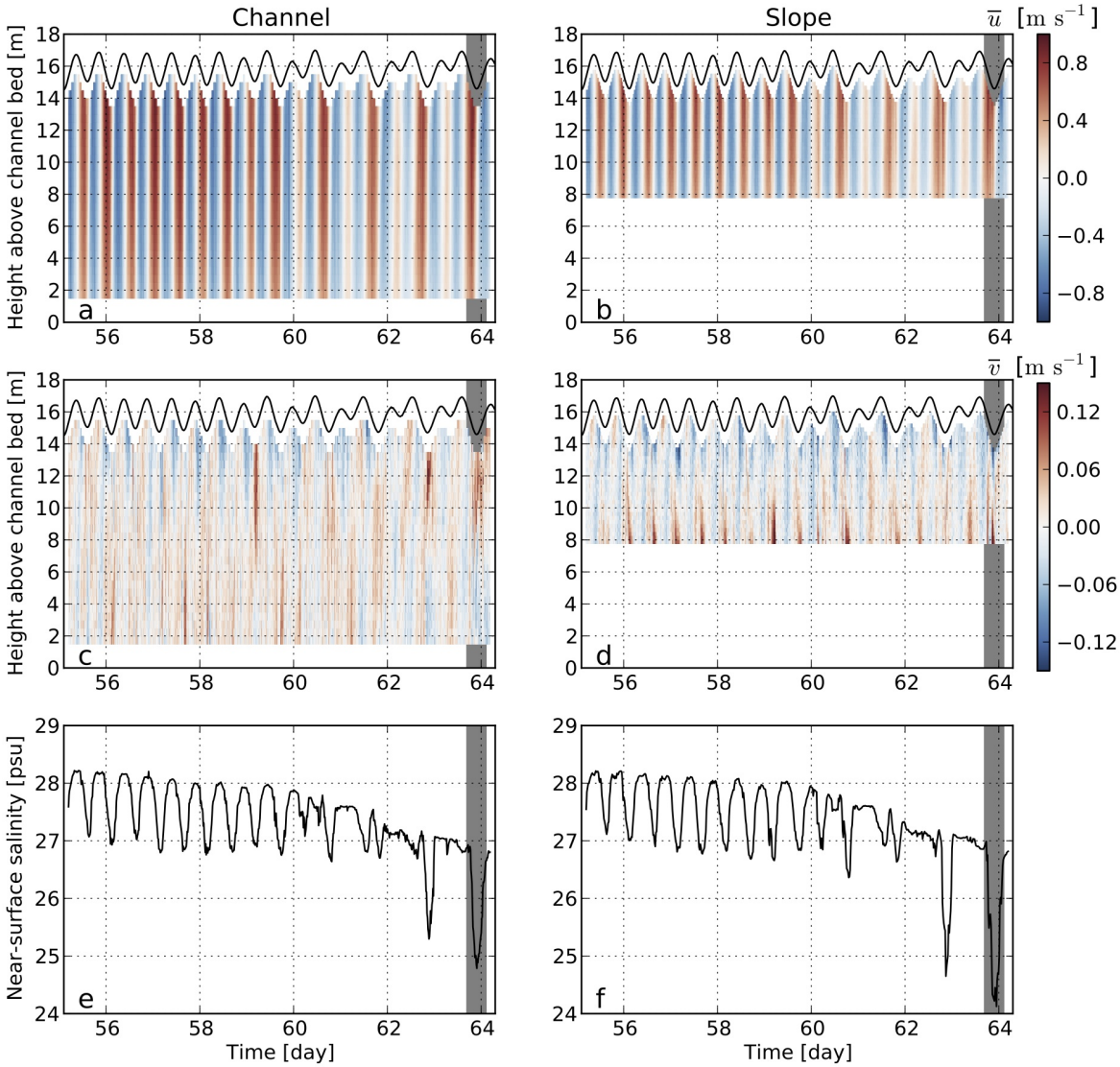

Figure 4.1: Mean flow observations during the first half of the winter experiment: longitudinal velocity $\overline{u}$ in the channel (a) and on the slope (b), lateral velocity $\overline{v}$ in the channel (c) and on the slope (d), near-surface salinity in the channel (e) and on the slope (f). The shaded areas highlight the period of the 5 March 2009 transect survey analyzed in this work. The black lines represent the surface elevation.

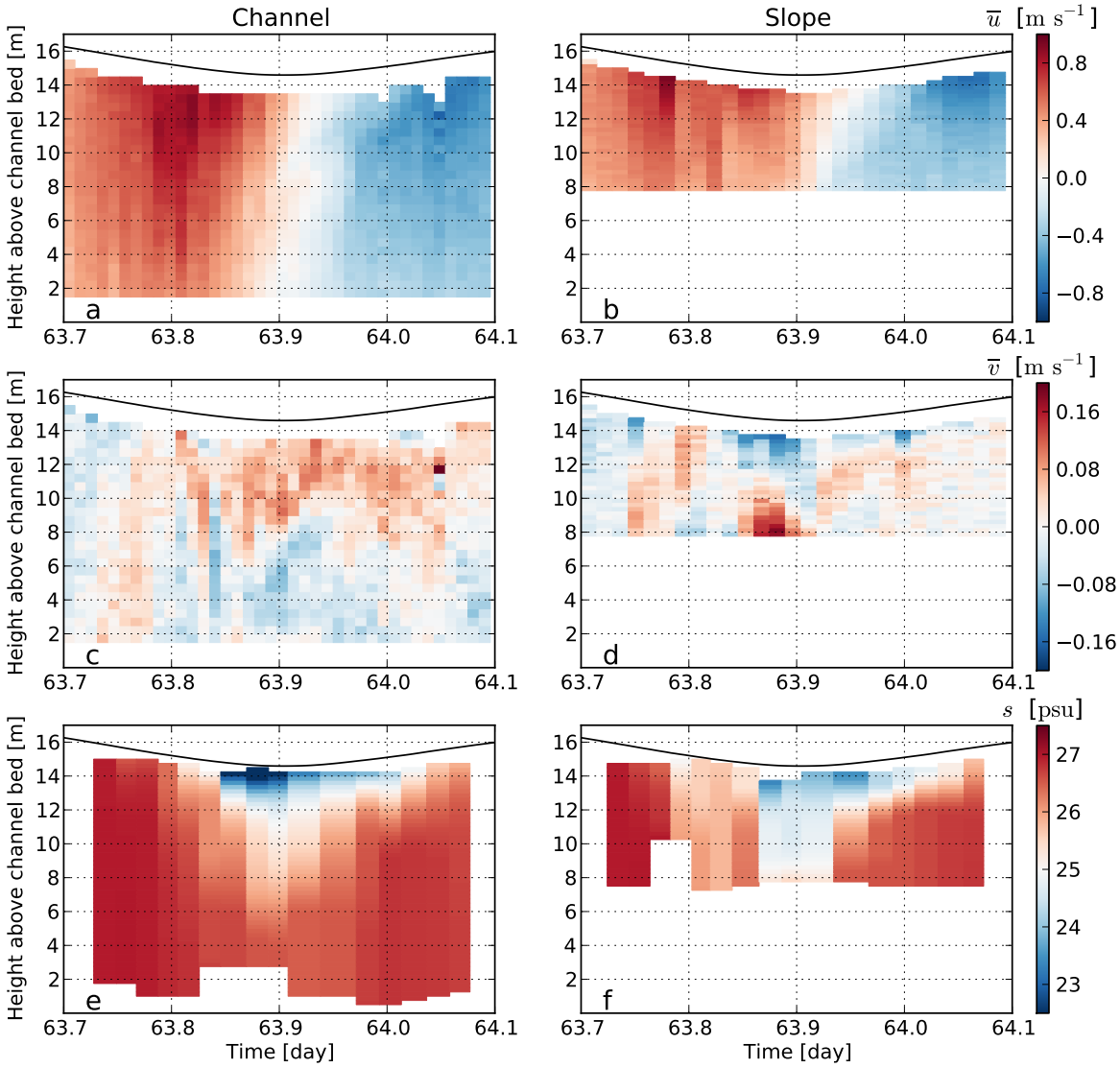

Figure 4.2: Mean flow observations during the 5 March 2009 transect survey: longitudinal velocity $\overline{u}$ from the moored ADCP in the channel (a) and on the slope (b), lateral velocity $\overline{v}$ from the moored ADCP in the channel (c) and on the slope (d), salinity profiles from the transect survey in the channel (e) and on the slope (f). The black lines represent the surface elevation.

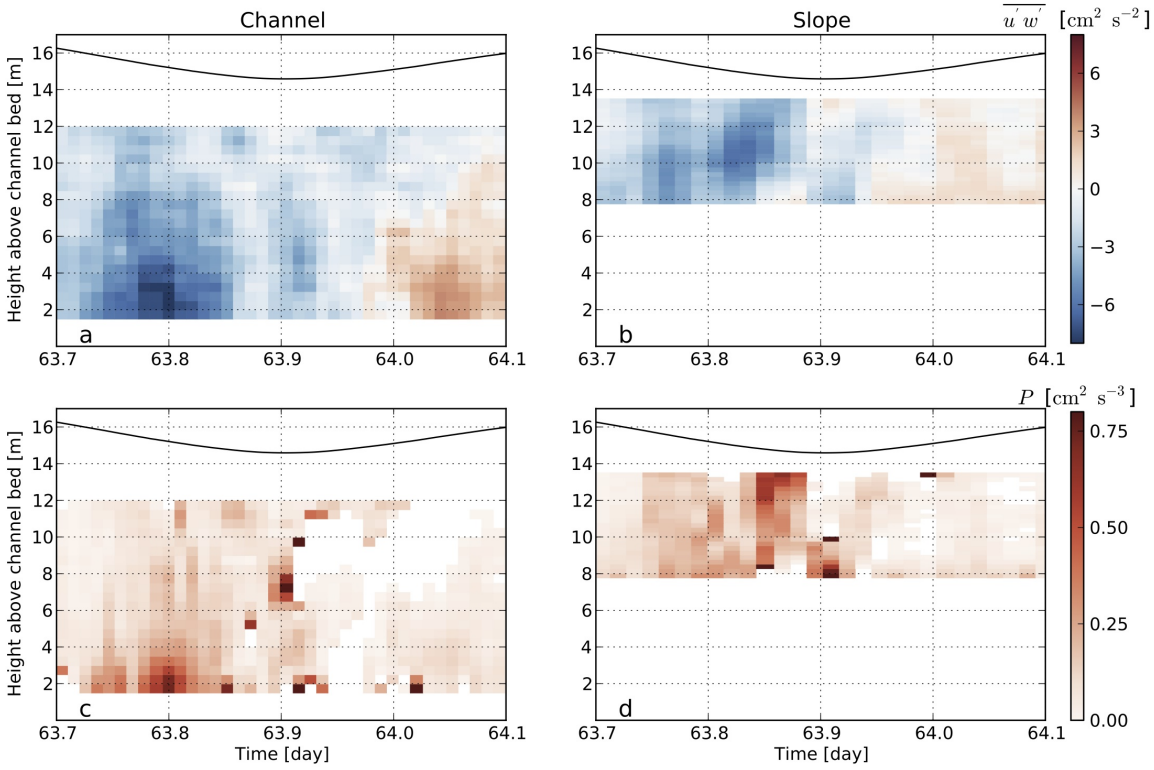

Figure 4.3: Estimates of Reynolds Stresses $\overline{u'w'}$ in the channel (a) and on the slope (b) and TKE shear production P in the channel (c) and on the slope (d) during the 5 March 2009 transect survey. The black lines represent the surface elevation.

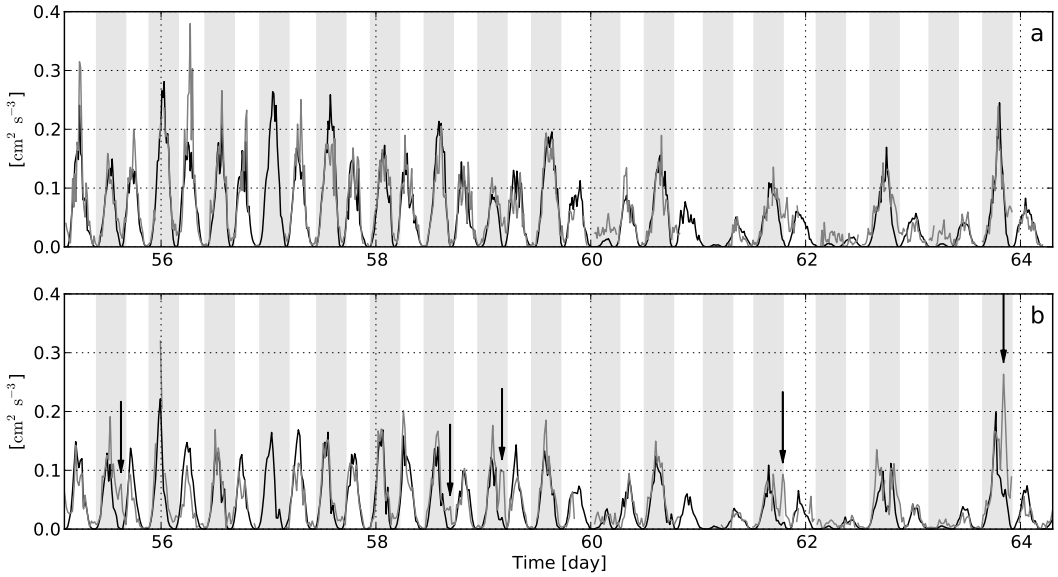

Figure 4.4: Depth-averaged TKE shear production $\langle P \rangle$ (gray lines) and bottom-drag power $C_D \left| \langle \overline{u} \rangle \right|^3 / H$ (black lines) in the channel (a) and on the slope (b) during the first half of the winter experiment. Missing values of $\langle P \rangle$ correspond to periods when the wind speed was greater than $5\,\mathrm{m\,s^{-1}}$. The shaded areas highlight the ebb tides. The arrows highlight events discussed in the text. The 5 March 2009 transect survey spans through half of the last highlighted ebb and half of the successive flood.

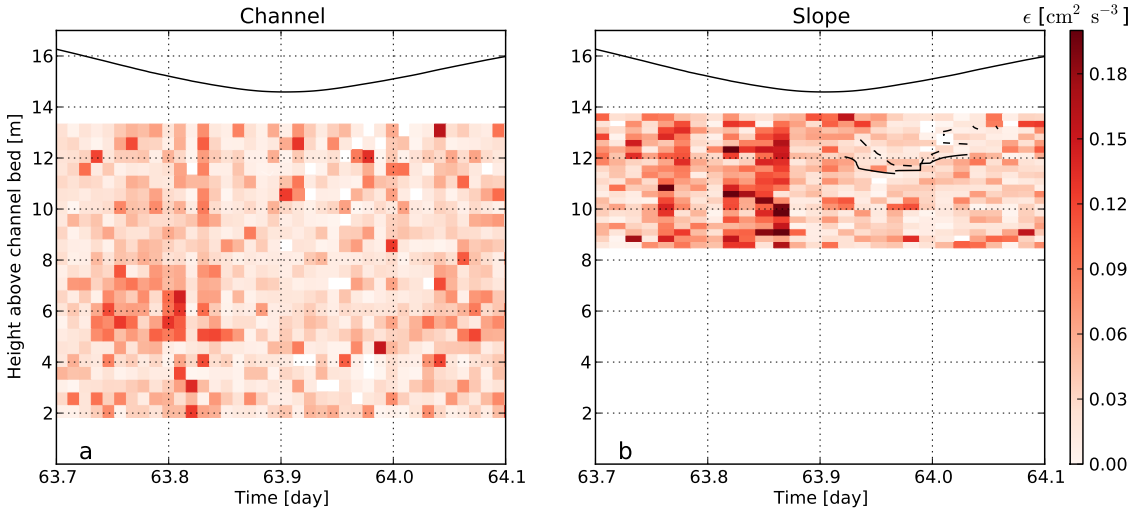

Figure 4.5: Estimates of the TKE dissipation rate ϵ in the channel (a) and on the slope (b) during the 5 March 2009 transect survey. The black contours represent the points where $l_N = 10\,\mathrm{m}$ (solid) and $l_N = 5\,\mathrm{m}$ (dashed). The black lines represent the surface elevation.

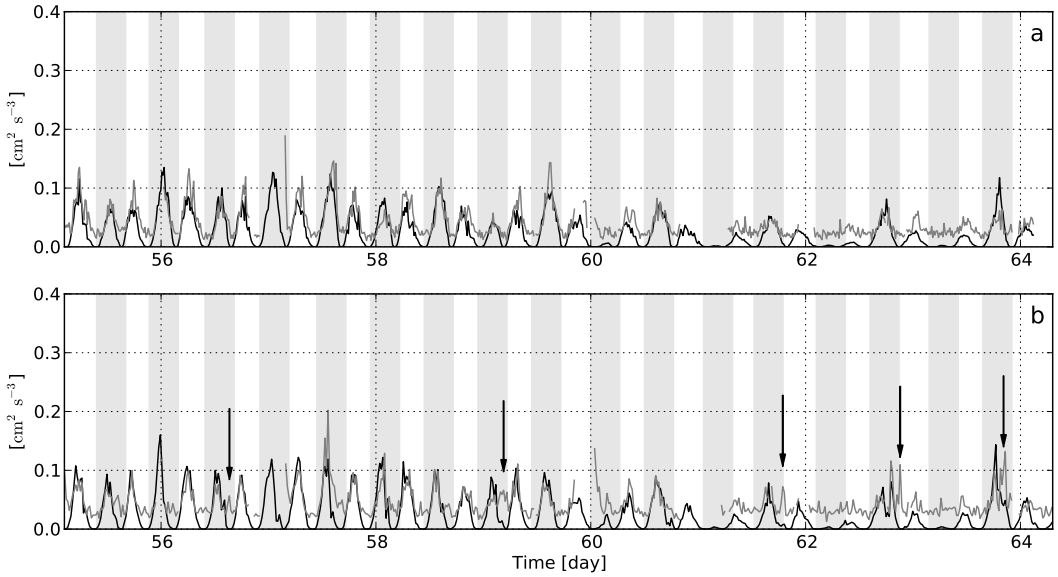

Figure 4.6: Depth-averaged TKE dissipation rate $\langle\epsilon\rangle$ (gray lines) and bottom-drag power $C_D\left|\langle\overline{u}\rangle\right|^3/H$ (black lines) in the channel (a) and on the slope (b) during the first half of the winter experiment. Missing values of $\langle\epsilon\rangle$ correspond to periods when the wind speed was greater than $5\,\mathrm{m\,s^{-1}}$. The shaded areas highlight the ebb tides. The arrows highlight events discussed in the text. The 5 March 2009 transect survey spans through half of the last highlighted ebb and half of the successive flood.

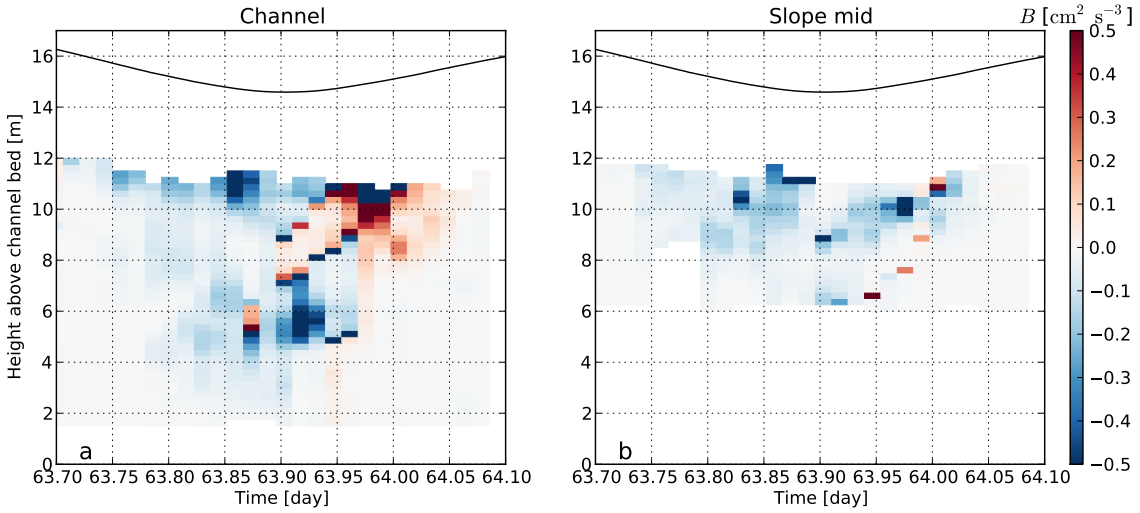

Figure 4.7: Estimates of the buoyancy flux B in the channel (a) and on the slope (b) during the 5 March 2009 transect survey. The black lines represent the surface elevation.

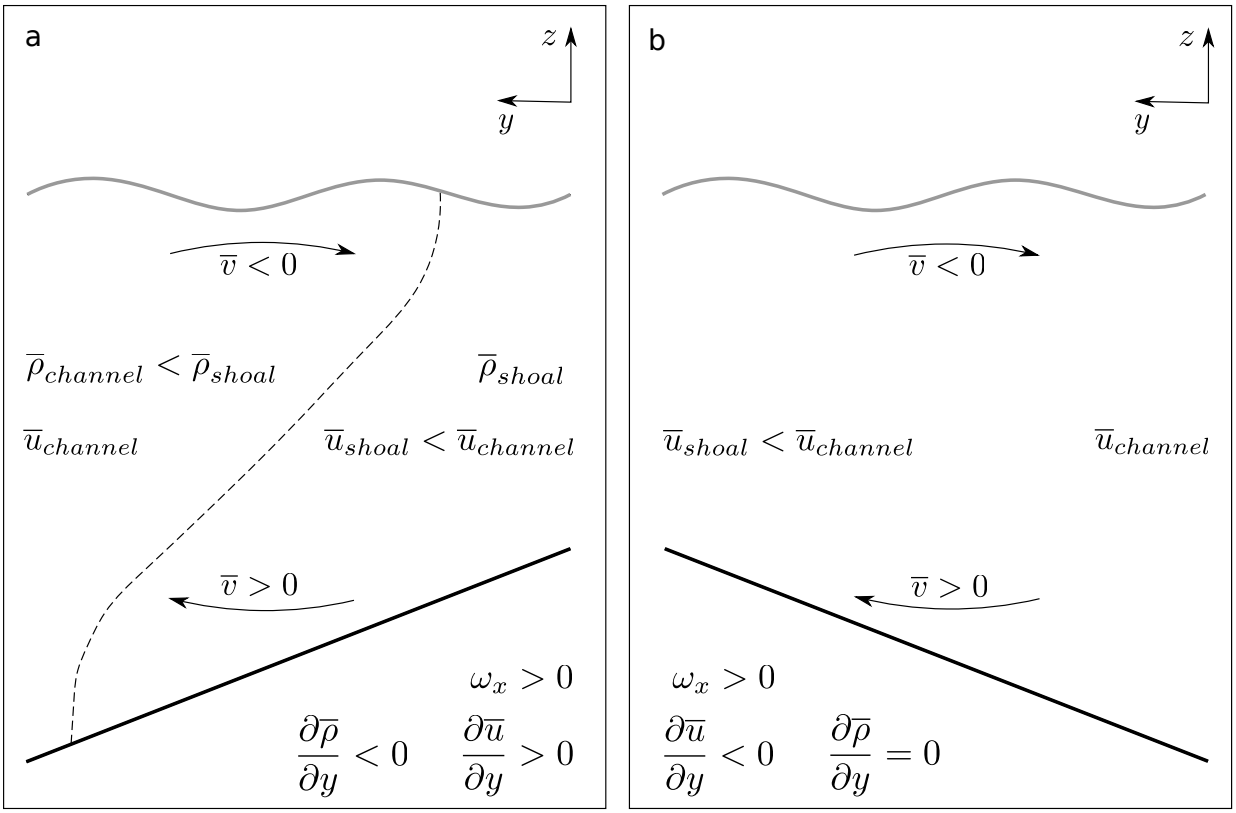

Figure 4.8: Examples of steady, density-driven (a) and rotation-driven (b) transverse circulations. The solid black lines represent the bed, the solid gray lines represent the surface and the dashed line represents the density interface. The arrows represent the direction of the lateral flow and circulation.

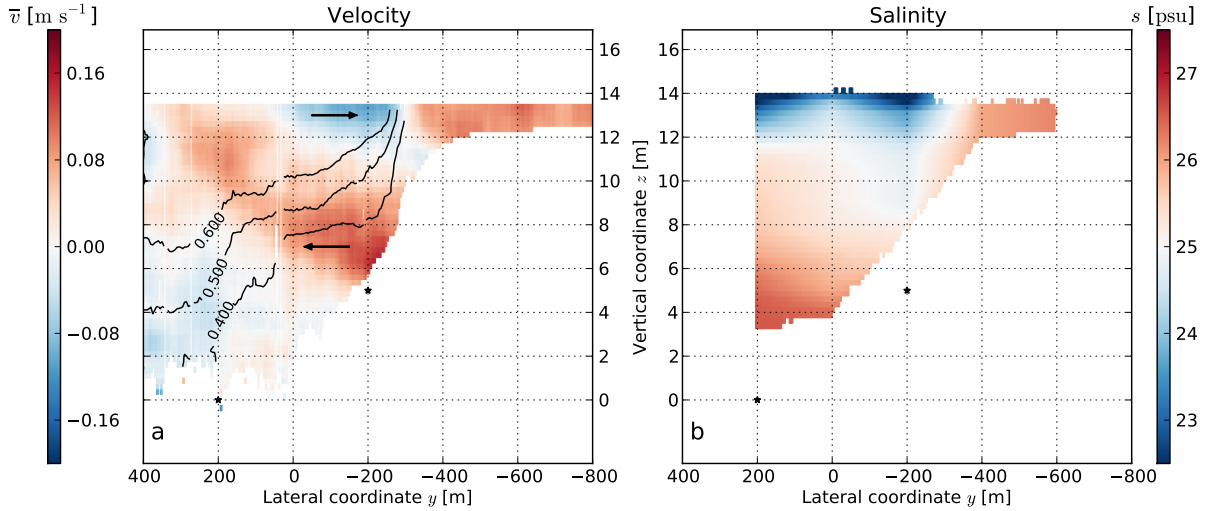

Figure 4.9: The late ebb circulation: lateral velocity $\overline{v}$ and longitudinal velocity $\overline{u}$ (contours) at the shoal-channel interface (a) and salinity s (b) measured during the eighth transect of the 5 March 2009 survey (63.85 days $\leq t \leq$ 63.87 days). The arrows highlight the direction of the lateral flow on the slope. The star symbols represent the approximate locations of the channel and slope moorings.

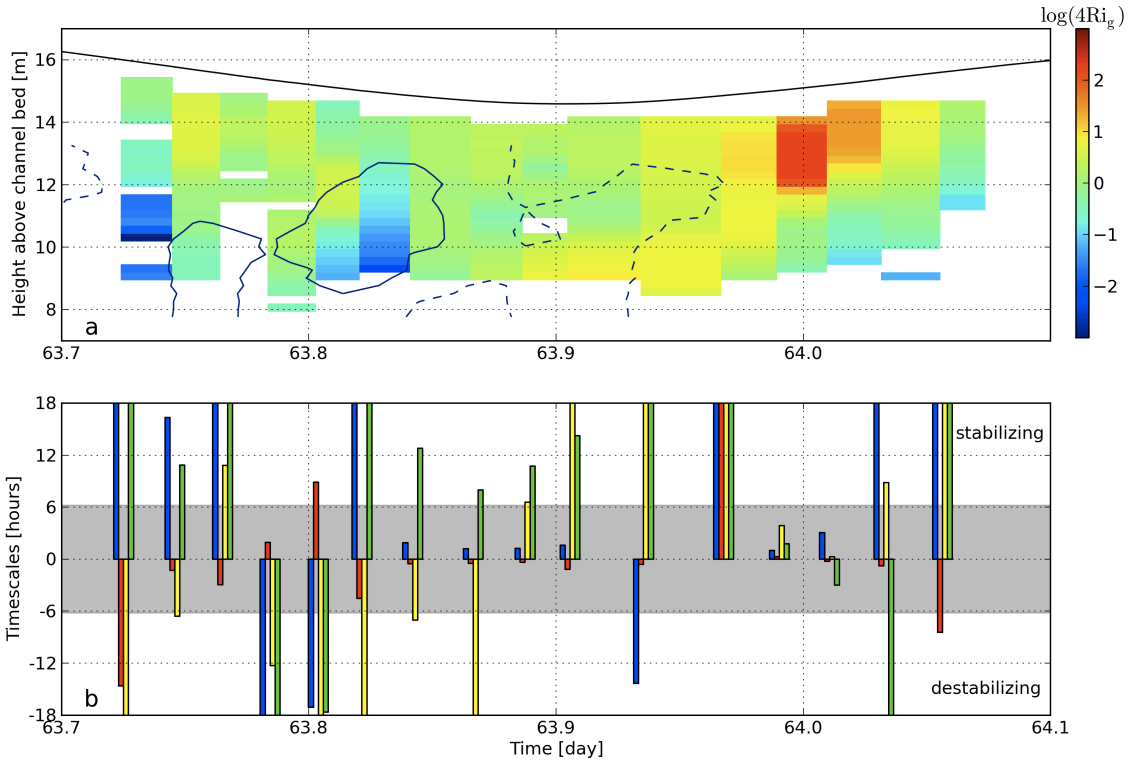

Figure 4.10: Profiles of $\log(4\mathrm{Ri}_g)$ on the slope during the 5 March 2009 transect survey (a) and characteristic timescales (b) of the four mechanisms representing the effects of the lateral circulation on stability defined in (4.31)-(4.34): density straining timescale τ_ρ (blue), shear straining timescale τ_u (red), rotation timescale τ_f (green) and unsteadiness timescale τ_t (yellow). A positive timescale represents a stabilizing effect, i.e. the associated mechanism acts to increase Ri_g. The black contours show the points where the Reynolds stress $\overline{u'w'} = -4\,\mathrm{cm}^2\,\mathrm{s}^{-2}$ (solid) and $\overline{u'w'} = -1\,\mathrm{cm}^2\,\mathrm{s}^{-2}$ (dashed). The shaded areas highlight timescales smaller than half the M2 tidal period (6.2 hours).

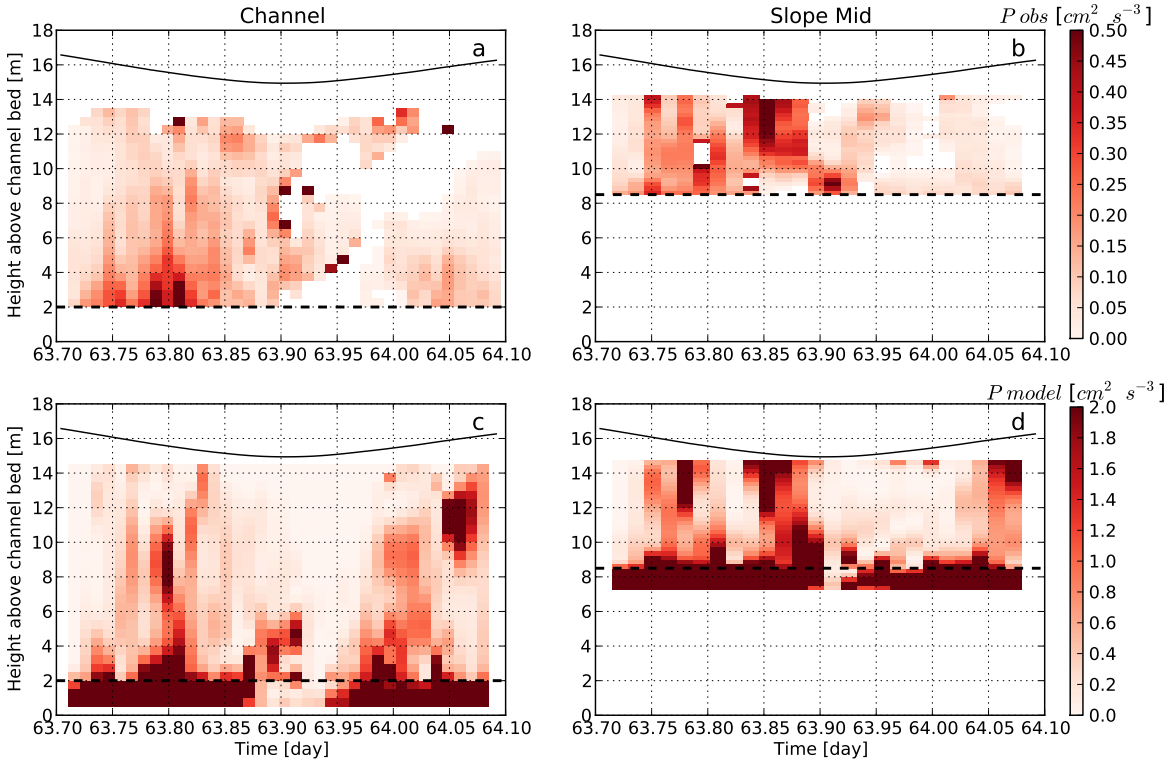

Figure 4.11: TKE shear production P during the 05 March 2009 transect survey: observations in the channel (a) and on the slope (b), and model outputs (case A) in the channel (c) and on the slope (d). The model case A is described in Table 4.2. The black solid line represents the surface elevation. The black dashed line represents the elevation of the lowest observation available.

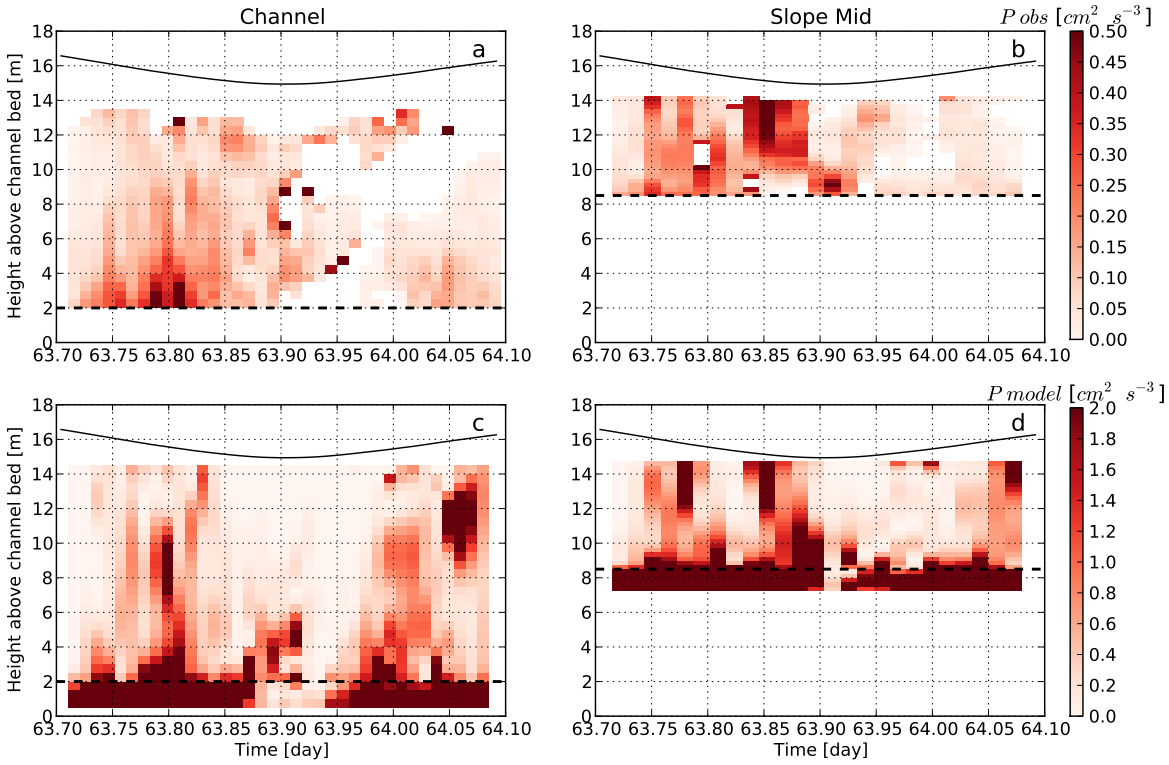

Figure 4.12: TKE shear production P during the 05 March 2009 transect survey: observations in the channel (a) and on the slope (b), and model outputs (case B) in the channel (c) and on the slope (d). The model case B is described in Table 4.2. The black solid line represents the surface elevation. The black dashed line represents the elevation of the lowest velocity observation available.

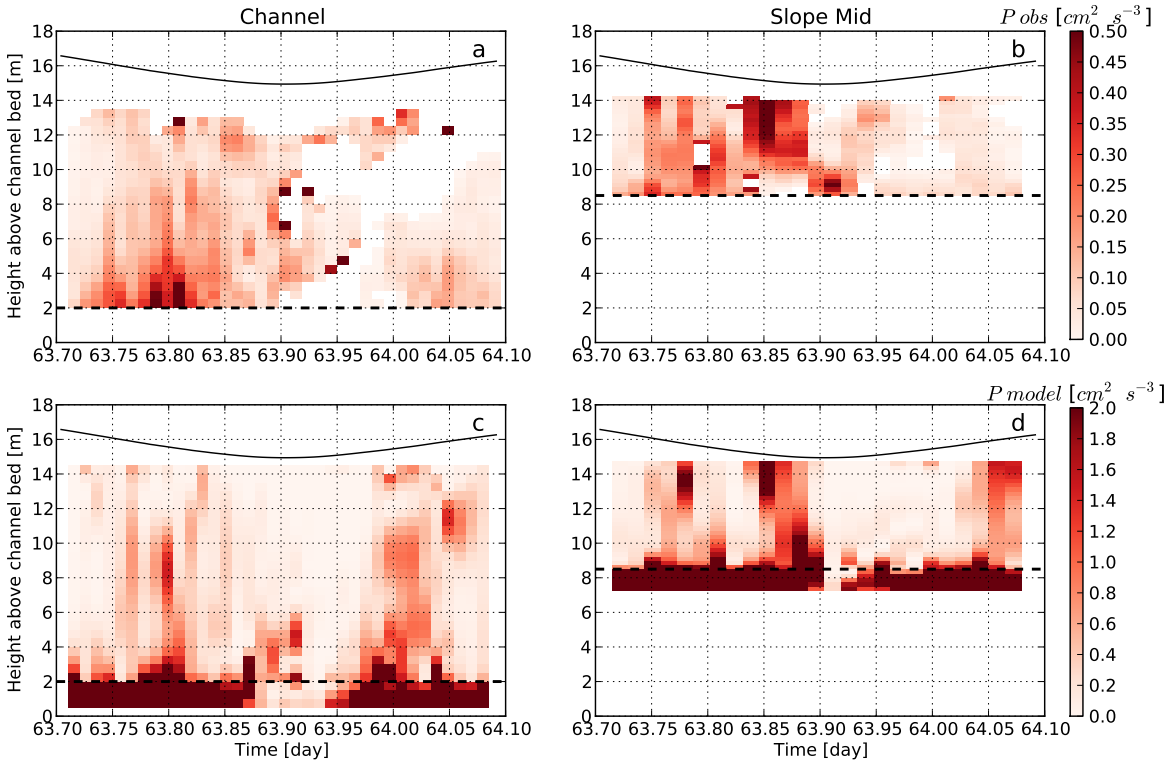

Figure 4.13: TKE shear production P during the 05 March 2009 transect survey: observations in the channel (a) and on the slope (b), and model outputs (case C) in the channel (c) and on the slope (d). The model case C is described in Table 4.2. The black solid line represents the surface elevation. The black dashed line represents the elevation of the lowest velocity observation available.

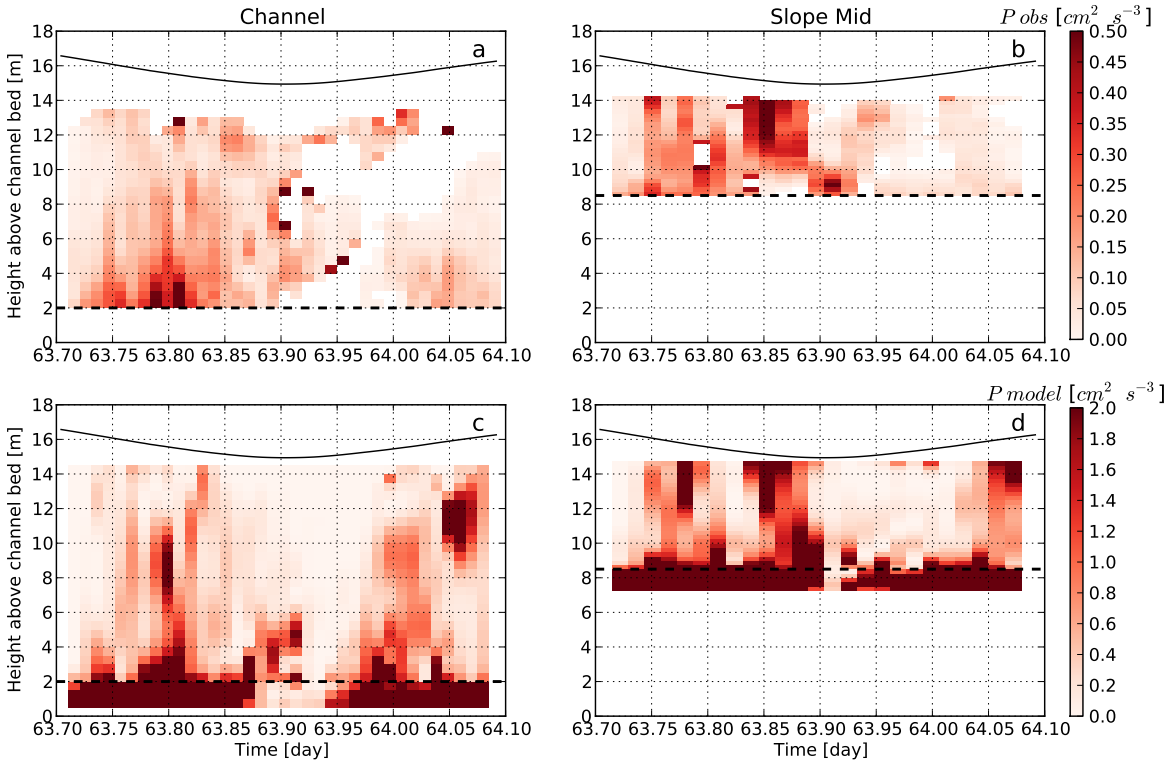

Figure 4.14: TKE shear production P during the 05 March 2009 transect survey: observations in the channel (a) and on the slope (b), and model outputs (case D) in the channel (c) and on the slope (d). The model case D is described in Table 4.2. The black solid line represents the surface elevation. The black dashed line represents the elevation of the lowest velocity observation available.

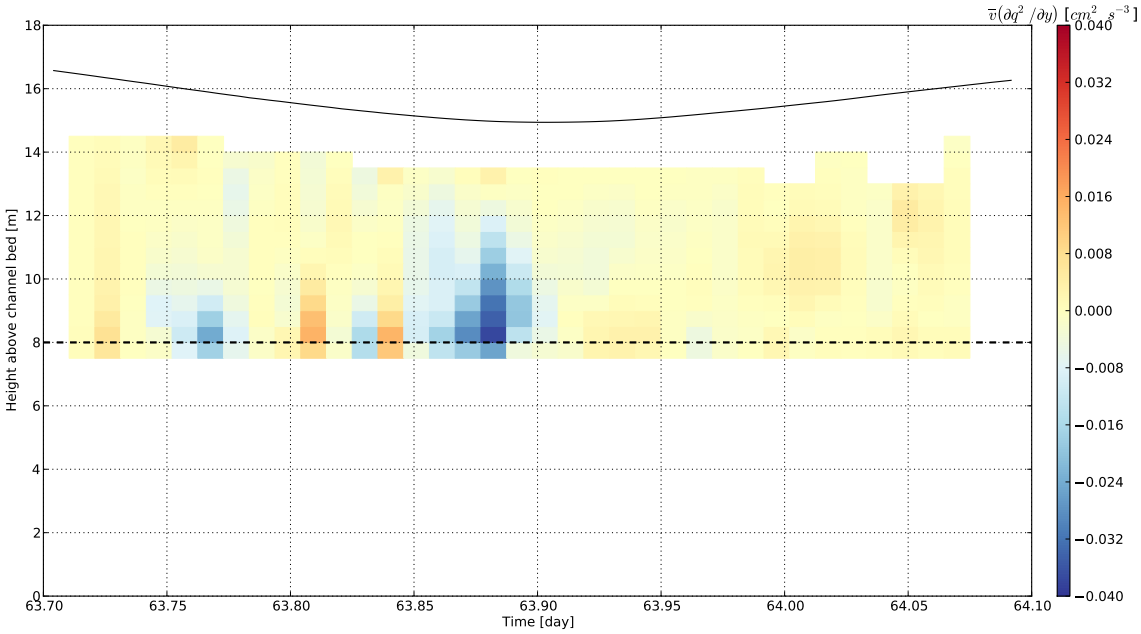

Figure 4.15: Lateral advection of TKE $\overline{v}(\partial q^2/\partial y)$ on the slope. The black solid line represents the surface elevation. The black dashed line represents the elevation of the lowest velocity observation available.

Table 4.1: Correlation coefficients between the bottom-drag power $C_D \left|\langle\overline{u}\rangle\right|^3/H$ and depth-averaged TKE shear production $\langle P\rangle$ or depth-averaged TKE dissipation rate $\langle\epsilon\rangle$. The drag coefficients C_D are estimated through a linear regression between $\langle P\rangle$ or $\langle\epsilon\rangle$ and $\left|\langle\overline{u}\rangle\right|^3/H$.

	$\langle P\rangle$ channel	$\langle P\rangle$ slope	$\langle\epsilon\rangle$ channel	$\langle\epsilon\rangle$ slope
Correlation Coefficient:	0.86	0.82	0.75	0.69
Drag Coefficient C_D:	8.3×10^{-4}	5.0×10^{-4}	4.0×10^{-4}	3.6×10^{-4}

Table 4.2: Turbulence closure models tested. The Generic Length Scale model was introduced by Umlauf and Burchard (2003). The Dynamic Dissipation Rate model is described by Rodi (1987).

Case	TKE q^2 models	Lengthscale l models	Stability functions models
A	$k-\epsilon$	General Length Scale	Schumann and Gerz (1995)
B	$k-\epsilon$	General Length Scale	Munk and Anderson (1954)
C	$k-\epsilon$	Dynamic Dissipation Rate	Schumann and Gerz (1995)
D	Mellor-Yamada	General Length Scale	Schumann and Gerz (1995)

Chapter 5

Horizontal Mixing

This chapter addresses the third research question described in section 1.3. On the shoals and in the channel, the velocity field is sheared mostly in the vertical direction (i.e. $\partial\overline{u}/\partial z$ and $\partial\overline{v}/\partial z$ are the largest coefficients of the shear rate tensor $s_{ij} = \partial\overline{u_i}/\partial x_j$) as a result of the no-slip boundary condition at the bed. As seen in the previous chapter, these vertical shears are the main source of turbulence as quantified by the TKE shear production term (equations 4.1 and 4.4), and therefore drive vertical and horizontal mixing in these two regions. Vertical shears are just as important on the slope, but lateral variations in bathymetry create a third dominant shear, the lateral shear of the longitudinal velocity component $\partial\overline{u}/\partial y$. At the shoal-channel interface, this lateral shear $\partial\overline{u}/\partial y$ is characterized by a the presence of an inflection point ($\partial^2\overline{u}/\partial y = 0$) where the lateral shear is maximum and therefore verifies a necessary condition for instabilities to develop (Kundu and Cohen 2008). Evidences of such horizontal shear instabilities have been observed in South San Francisco Bay (Figures 5.1 and 5.2). While the lateral shear is weaker than the vertical shears, the size of the associated horizontal instabilities is potentially much larger than those associated with the vertical shears, because not restricted by the height of the water column. These coherent structures or eddies associated with horizontal shear instabilities can transport momentum and scalars and therefore provide another potential mechanism for horizontal mixing across the shoal-channel interface. The first section is focused on the analysis of the lateral shear and quantifying lateral mixing at the interface. In the second section, different horizontal mixing processes are explored and compared to characterize the observed lateral mixing.

The analysis presented in this chapter is based on the data from the three winter 2009 transect surveys, and more specifically the low-pass filtered velocities ($\widehat{u}(y,z,t), \widehat{v}(y,z,t)$), which are obtained by applying a spatial low-pass filter (moving average with window size 200 m in the lateral direction y and 1 m in the vertical direction z) to the raw velocities (u, v). This low-pass filter removes the small-scale variability of the flow but preserves the large-scale variability associated with transverse changes in bathymetry at the shoal-channel interface.

5.1 The Lateral Shear Budget

Framework

To identify and analyze the physical processes driving the intratidal dynamics of the lateral shear at the shoal-channel interface, we derive a budget for the lateral shear of the depth-averaged, low pass filtered longitudinal velocity $\partial \langle \widehat{u} \rangle / \partial y$. The low-pass filtered continuity equation writes

$$\frac{\partial \widehat{u}}{\partial x} + \frac{\partial \widehat{v}}{\partial y} + \frac{\partial \widehat{w}}{\partial z} = 0 \tag{5.1}$$

and the momentum budget for the low-pass filtered longitudinal velocity $\widehat{u}$ writes

$$\frac{\partial \widehat{u}}{\partial t} + \frac{\partial \widehat{u}\widehat{u}}{\partial x} + \frac{\partial \widehat{v}\widehat{u}}{\partial y} + \frac{\partial \widehat{w}\widehat{u}}{\partial z} = -\frac{1}{\rho}\frac{\partial \widehat{p}}{\partial x} + \nu \Delta \widehat{u} - \frac{\partial}{\partial x}\left(\widehat{uu} - \widehat{u}\widehat{u}\right) - \frac{\partial}{\partial y}\left(\widehat{vu} - \widehat{v}\widehat{u}\right) - \frac{\partial}{\partial z}\left(\widehat{wu} - \widehat{w}\widehat{u}\right) \tag{5.2}$$

On the left hand side of equation (5.2), the first term is the inertia or unsteadiness term, the second is the longitudinal advection term, the third is the lateral advection term and the fourth is the vertical advection term. On the right hand side, the first term is the longitudinal pressure gradient, the second is the viscous stress term, the third represents the longitudinal subfilter scale (SFS) stress, the fourth represents the lateral SFS stress and the fifth represents the vertical SFS stress. The SFS stresses emerge from velocity correlations associated with structures of scale smaller than the low-pass filter cutoff (200 m in the y direction and 1 m in the z direction). These structures can be of various sources, for instance waves, turbulent eddies or billows associated with shear instabilities. We assume that the SFS stresses $\tau_{xx} = \widehat{uu} - \widehat{u}\widehat{u}$, $\tau_{yx} = \widehat{vu} - \widehat{v}\widehat{u}$ and $\tau_{zx} = \widehat{wu} - \widehat{w}\widehat{u}$ are much larger than viscous stresses, which we neglect from now on. Using the continuity equation (5.1) we can rewrite equation (5.2) as

$$\frac{\partial \widehat{u}}{\partial t} + \widehat{u}\frac{\partial \widehat{u}}{\partial x} + \widehat{v}\frac{\partial \widehat{u}}{\partial y} + \widehat{w}\frac{\partial \widehat{u}}{\partial z} = -\frac{1}{\rho}\frac{\partial \widehat{p}}{\partial x} - \frac{\partial \tau_{xx}}{\partial x} - \frac{\partial \tau_{yx}}{\partial y} - \frac{\partial \tau_{zx}}{\partial z} \tag{5.3}$$

Taking the depth-average of (5.3), represented by a bracket operator $\langle f \rangle \equiv 1/\left(H + \eta\right) \int_{-H}^{\eta} f dz$ where $z = -H$ is the coordinate of the bottom and $z = \eta$ is the coordinate of the free surface, yields:

$$\left\langle \frac{\partial \widehat{u}}{\partial t} \right\rangle + \left\langle \widehat{u}\frac{\partial \widehat{u}}{\partial x} \right\rangle + \left\langle \widehat{v}\frac{\partial \widehat{u}}{\partial y} \right\rangle + \left\langle \widehat{w}\frac{\partial \widehat{u}}{\partial z} \right\rangle = \left\langle -\frac{1}{\rho}\frac{\partial \widehat{p}}{\partial x} \right\rangle - \left\langle \frac{\partial \tau_{xx}}{\partial x} \right\rangle - \left\langle \frac{\partial \tau_{yx}}{\partial y} \right\rangle - \left\langle \frac{\partial \tau_{zx}}{\partial z} \right\rangle \tag{5.4}$$

Assuming no surface stress and modeling the bottom stress with a quadratic drag law yields:

$$\left\langle \frac{\partial \tau_{zx}}{\partial z} \right\rangle = \frac{\tau_{zx}(z = \eta) - \tau_{zx}(z = -H)}{H + \eta} = -\frac{\tau_{zx}(z = -H)}{H + \eta} = \frac{C_D \langle \widehat{u} \rangle \left| \langle \widehat{u} \rangle \right|}{H + \eta} \tag{5.5}$$

where C_D is a constant dimensionless drag coefficient, which we assume equal to 0.0025, a typical value for estuaries (Li and O'Donnell 1997; Stacey et al. 1999a). Since the free-surface

elevation η varies in time, the time derivative and depth-average operators do not commute in general:

$$\left\langle \frac{\partial \widehat{u}}{\partial t} \right\rangle = \frac{\partial \left\langle \widehat{u} \right\rangle}{\partial t} + \left(\frac{\left\langle \widehat{u} \right\rangle - \widehat{u}(z=\eta)}{H+\eta} \right) \frac{\partial \eta}{\partial t} \tag{5.6}$$

However, observations from the moored channel and slope mid ADCPs show that the second term on the right hand side of (5.6) is smaller than the other two terms in practice (Figure 5.3), such that the two operators approximately commute in this case:

$$\left\langle \frac{\partial \widehat{u}}{\partial t} \right\rangle \simeq \frac{\partial \left\langle \widehat{u} \right\rangle}{\partial t} \tag{5.7}$$

Substituting (5.5) and (5.7) in (5.4) yields then:

$$\frac{\partial \left\langle \widehat{u} \right\rangle}{\partial t} + \left\langle \widehat{u} \frac{\partial \widehat{u}}{\partial x} \right\rangle + \left\langle \widehat{v} \frac{\partial \widehat{u}}{\partial y} \right\rangle + \left\langle \widehat{w} \frac{\partial \widehat{u}}{\partial z} \right\rangle = \left\langle -\frac{1}{\rho} \frac{\partial \widehat{p}}{\partial x} \right\rangle - \left\langle \frac{\partial \tau_{xx}}{\partial x} \right\rangle - \left\langle \frac{\partial \tau_{yx}}{\partial y} \right\rangle - \frac{C_D \left\langle \widehat{u} \right\rangle \left| \left\langle \widehat{u} \right\rangle \right|}{H+\eta} \tag{5.8}$$

Finally, taking the lateral derivative $\partial/\partial y$ of this equation yields a budget for the depth-averaged lateral shear:

$$\begin{aligned} \frac{\partial}{\partial t}\left(\frac{\partial \left\langle \widehat{u} \right\rangle}{\partial y} \right) \simeq \; & -\frac{\partial}{\partial y}\left\langle \widehat{u} \frac{\partial \widehat{u}}{\partial x} \right\rangle - \frac{\partial}{\partial y}\left\langle \widehat{v} \frac{\partial \widehat{u}}{\partial y} \right\rangle - \frac{\partial}{\partial y}\left\langle \widehat{w} \frac{\partial \widehat{u}}{\partial z} \right\rangle \\ & -\frac{\partial}{\partial y}\left\langle \frac{\partial \tau_{xx}}{\partial x} \right\rangle - \frac{\partial}{\partial y}\left\langle \frac{\partial \tau_{yx}}{\partial y} \right\rangle - \frac{\partial}{\partial y}\left(\frac{C_D \left\langle \widehat{u} \right\rangle \left| \left\langle \widehat{u} \right\rangle \right|}{H+\eta} \right) \end{aligned} \tag{5.9}$$

where we assumed the lateral variations of the depth-averaged pressure gradient negligible at the scale of the shoal-channel interface:

$$\frac{\partial}{\partial y}\left\langle -\frac{1}{\rho} \frac{\partial \widehat{p}}{\partial x} \right\rangle \ll \frac{\partial}{\partial y}\left(\frac{C_D \left\langle \widehat{u} \right\rangle \left| \left\langle \widehat{u} \right\rangle \right|}{H+\eta} \right) \tag{5.10}$$

This assumption is motivated by the fact that in estuaries, the characteristic length scales of free-surface variations are typically set by the horizontal dimensions of the basin ($10-100\,\mathrm{km}$) or wavelengths of tidal constituents ($> 100\,\mathrm{km}$). These length scales are therefore much larger than the width the shoal-channel interface ($400\,\mathrm{m}$) which sets the characteristic length scale of lateral variations of the friction term. Similarly to the forcing (pressure gradient), the bathymetry H does not change significantly in the longitudinal direction x at the scale of the shoal-channel interface ($400\,\mathrm{m}$), and as a result longitudinal gradients $\partial\widehat{u}/\partial x$ and $\partial\tau_{xx}/\partial x$ can be neglected. The vertical velocity $\widehat{w}(y,z,t)$ is unknown because smaller than the detection level of the ADCPs, but it can be reconstructed by integrating the continuity equation:

$$0 = \frac{\partial \widehat{u}}{\partial x} + \frac{\partial \widehat{v}}{\partial y} + \frac{\partial \widehat{w}}{\partial z} \simeq \frac{\partial \widehat{v}}{\partial y} + \frac{\partial \widehat{w}}{\partial z} \tag{5.11}$$

vertically between the elevation z and the free surface elevation $z=\eta$:

$$\widehat{w}(y,z,t) = \frac{\partial \eta}{\partial t} + \int_z^\eta \frac{\partial \widehat{v}}{\partial y} dz \tag{5.12}$$

The rate of change of the free surface elevation $\partial\eta/\partial t$ is expected to scale with the tidal period and therefore be negligible in (5.12):

$$\frac{\partial \eta}{\partial t} \simeq \frac{2\,\mathrm{m}}{6\,\mathrm{hrs}} \simeq 10^{-4}\,\mathrm{m\,s^{-1}} \ll \int_z^\eta \frac{\partial \widehat{v}}{\partial y} dz \simeq (1-10\,\mathrm{m})\frac{0.1\,\mathrm{m\,s^{-1}}}{100\,\mathrm{m}} \simeq 10^{-2} - 10^{-3}\,\mathrm{m\,s^{-1}} \quad (5.13)$$

such that:

$$\widehat{w}(y,z,t) \simeq \int_z^\eta \frac{\partial \widehat{v}}{\partial y} dz \quad (5.14)$$

Finally, after subtituting (5.14) in (5.9), the physical processes involved in equation (5.9) can be better understood by expanding the bed friction term

$$\begin{aligned} \tfrac{\partial}{\partial t}\left(\tfrac{\partial \langle \widehat{u}\rangle}{\partial y}\right) \simeq \; & -\tfrac{\partial}{\partial y}\left\langle \widehat{v}\tfrac{\partial \widehat{u}}{\partial y}\right\rangle - \tfrac{\partial}{\partial y}\left\langle \left(\int_z^\eta \tfrac{\partial \widehat{v}}{\partial y} dz\right)\tfrac{\partial \widehat{u}}{\partial z}\right\rangle \\ & -\tfrac{\partial}{\partial y}\left\langle \tfrac{\partial \tau_{yx}}{\partial y}\right\rangle - \left[\tfrac{C_D\left|\langle \widehat{u}\rangle\right|}{H+\eta}\left(2\tfrac{\partial \langle \widehat{u}\rangle}{\partial y} - \tfrac{\langle \widehat{u}\rangle}{H+\eta}\tfrac{dH}{dy}\right)\right] \end{aligned} \quad (5.15)$$

where we neglected lateral variations of the free-surface $\partial\eta/\partial y \ll dH/dy$ in the friction term for the same reasons invoked in the previous paragraph. The term on the left hand side of equation (5.15) represents the rate of change of the lateral shear. On the right hand side, the first term represents lateral advection and the second term represents vertical advection. The third term represents the lateral diffusion of the lateral shear by subfilter scale coherent structures such as eddies associated with turbulence and shear instabilities, and is therefore expected to act primarily as a sink. The fourth and last term represents the effects of the bottom stress on the depth-averaged lateral shear. This term forces the lateral shear towards an equilibrium lateral profile $\langle \widehat{u}\rangle(y) \propto \sqrt{H(y)}$. If we consider an ebb tide ($\langle \widehat{u}\rangle > 0$; $\partial\langle \widehat{u}\rangle/\partial y > 0$) in the case of this shoal-channel interface ($dH/dy > 0$), the bottom stress term acts as a source if the lateral shear is smaller than the equilibrium shear:

$$\frac{\partial \langle \widehat{u}\rangle}{\partial y} < \frac{\langle \widehat{u}\rangle}{2(H+\eta)}\frac{dH}{dy} \quad (5.16)$$

and acts as a sink if the lateral shear is larger than the equilibrium shear:

$$\frac{\partial \langle \widehat{u}\rangle}{\partial y} > \frac{\langle \widehat{u}\rangle}{2(H+\eta)}\frac{dH}{dy} \quad (5.17)$$

All the terms of (5.15) are estimated using the transect observations, except for the lateral mixing term which is estimated as the residual:

$$\begin{aligned} -\tfrac{\partial}{\partial y}\left\langle \tfrac{\partial \tau_{yx}}{\partial y}\right\rangle \simeq \; & \tfrac{\partial}{\partial t}\left(\tfrac{\partial \langle \widehat{u}\rangle}{\partial y}\right) + \tfrac{\partial}{\partial y}\left\langle \widehat{v}\tfrac{\partial \widehat{u}}{\partial y}\right\rangle + \tfrac{\partial}{\partial y}\left\langle \left(\int_z^\eta \tfrac{\partial \widehat{v}}{\partial y} dz\right)\tfrac{\partial \widehat{u}}{\partial z}\right\rangle \\ & + \left[\tfrac{C_D\left|\langle \widehat{u}\rangle\right|}{H+\eta}\left(2\tfrac{\partial \langle \widehat{u}\rangle}{\partial y} - \tfrac{\langle \widehat{u}\rangle}{H+\eta}\tfrac{dH}{dy}\right)\right] \end{aligned} \quad (5.18)$$

The spatial and time derivatives are estimated using second order centered finite difference. The water column depth $H+\eta$ is inferred from the ADCP measurements.

27 February 2009 survey

The low-pass filtered velocity $(\widehat{u}(y,z,t), \widehat{v}(y,z,t))$ from the nineteen transects performed that day (referred to as T1-T19) are presented on Figure 5.4. During that day an entire flood was surveyed (T1-T12) and the beginning of the following ebb (T13-T19). The lateral velocity field displays clockwise circulations developing during the first two transects T1 and T12 and at the beginning of the ebb (T17 through T19). The lateral circulation is associated with a lateral convergence front developing at the edge of the shoal during T1, T18 and T19 (Figure 5.4b).

The depth-averaged lateral shear $\partial \langle \widehat{u} \rangle / \partial y$ is presented in Figure 5.5. At the beginning of the flood (T1: $t \simeq 57.70$ days), the flow on the shoal is leading the flow in the channel (Figure 5.4a) as a result of stronger friction and weaker inertia on the shoal (both a consequence of the smaller depth on the shoal) such that the lateral shear is still positive (Figure 5.5a). The lateral shear reverses around $t \simeq 57.75$ days. It becomes then concentrated in two cores located at the edge of the shoal and the edge of the channel, the former being the strongest with a peak lateral shear $\partial \langle \widehat{u} \rangle / \partial y \simeq -1 \times 10^{-3}\,\mathrm{s}^{-1}$. The two cores appear to shift gradually toward each other and eventually merge into a single wider but weaker core at the end of the flood (Figure 5.5a; $t \simeq 57.90$ days). During the following ebb, the lateral shear is concentrated in a single core at the edge of the shoal where $\partial \langle \widehat{u} \rangle / \partial y \simeq 1 \times 10^{-3}\,\mathrm{s}^{-1}$ (Figure 5.5a; $t \simeq 58.05$ days).

The five terms of the lateral shear budget (5.15) are presented on Figure 5.6. The friction term emerges as the strongest term of the budget with a peak value $\simeq -0.6 \times 10^{-6}\,\mathrm{s}^{-1}$ during the flood and $\simeq 0.4 \times 10^{-6}\,\mathrm{s}^{-1}$ during the ebb. This term is weak as the tide reverses around $t \simeq 57.90$ days (Figure 5.6a). The lateral and vertical advection terms are weaker during that survey (Figure 5.6b,c). The unsteadiness term contributes at leading order but displays less spatial and temporal coherence than the friction term (Figure 5.6d). As a result, the lateral mixing term estimated as the residual is also characterized by more spatial and temporal heterogeneity than the friction term (Figure 5.6e).

05 March 2009 survey

The low-pass filtered velocity data from the seventeen transects performed that day (referred to as T1-T17) were presented in chapter 3 on Figure 3.1. The survey sampled most of a strong ebb (T1-T11) and the beginning of the successive flood (T12-T17). The intratidal variability of the lateral circulation developing on the slope is characterized by multiple reversals throughout the ebb, which were described and analyzed in chapter 3.

Similarly to the lateral circulation, the depth-averaged lateral shear $\partial \langle \widehat{u} \rangle / \partial y$ displays pronounced spatial and temporal variability as shown on Figure 5.7. During the ebb, a positive core develops at the edge of the shoal (between $y = -400$ m and $y = -200$ m) with peak value reaching $\partial \langle \widehat{u} \rangle / \partial y \simeq 1.5 \times 10^{-3}\,\mathrm{s}^{-1}$. As the ebb tide slows down and reverses ($t \simeq 63.90$ days to $t \simeq 63.95$ days), the lateral shear becomes more variable spatially: the positive core shifts over the shoal (between $y = -600$ m and $y = -400$ m) and is replaced by

a negative core (Figure 5.7a). Simultaneously, positive shear develops in the channel. This pattern fades gradually from $t \simeq 63.95\,\text{days}$ until $t \simeq 64.05\,\text{days}$, then a weaker negative shear develops at the interface.

The five terms of the lateral shear budget (5.15) are presented on Figure 5.8. During that period, all terms contribute at leading order. As observed during the 27 February 2009, the friction term is strongest at the edge of the shoal, between $y = -400\,\text{m}$ and $y = -200\,\text{m}$ (Figure 5.8a). The advection and unsteadiness terms display greater spatial and temporal variability (Figure 5.8b,c,d). The variability of the advection terms is a direct consequence of the evolution of the lateral circulation on the slope. As a result, the residual/lateral mixing term is characterized by hot spots lasting $30 - 60\,\text{min}$ and a characteristic length scale of $200\,\text{m}$ in the transverse y direction (Figure 5.8e).

09 March 2009 survey

The low-pass filtered velocity data from the fifteen transects performed that day (referred to as T1-T15) are presented on Figure 5.9. The evolution of the lateral velocity field $\widehat{v}$ is similar to the observations described and analyzed in chapter 3: a clockwise circulation develops early in the ebb from transects T6 to T9, then nearly vanishes from T10 to T12 and strengthens again near the end of the ebb from T13 to T15 (Figure 5.9b). A convergence front develops during the last two transects T14 and T15 at the edge of the shoal.

The depth-averaged lateral shear $\partial \langle \widehat{u} \rangle / \partial y$ is presented in Figure 5.10. At the end of the flood, the depth-averaged lateral shear is concentrated in two cores at the edge of the shoal and the edge of the channel and reaches a peak value of $\partial \langle \widehat{u} \rangle / \partial y \simeq -8 \times 10^{-4}\,\text{s}^{-1}$. The lateral shear decreases as the tide reverses, down to zero about an hour after high water and quickly increases as the ebb accelerates. During the ebb, a stronger lateral shear layer develops at the edge of the shoal and reaches a maximal value of $\partial \langle \widehat{u} \rangle / \partial y \simeq 1.2 \times 10^{-3}\,\text{s}^{-1}$. The lateral shear layer expands over the width of the slope for most of the ebb, but narrows down late in the ebb ($t \geq 68.0\,\text{days}$).

The five terms of equation (5.15) are presented on Figure 5.11. The unsteadiness term $\partial/\partial t(\partial \langle \widehat{u} \rangle / \partial y)$ is small for most of the period sampled, except for the early part of the ebb (Figure 5.11d) when the depth-averaged lateral shear increases rapidly, as observed on Figure 5.10b. The bed friction term $-C_D \left| \langle \widehat{u} \rangle \right| / (H+\eta) \left[2\partial \langle \widehat{u} \rangle / \partial y - \langle \widehat{u} \rangle (dH/dy)/(H+\eta) \right]$ is small during the end of the flood, but increases rapidly early in the ebb to become the primary source of lateral shear at the edge of the shoal during the first half of the ebb, and vanishes progressively during the second half of the ebb (Figure 5.11a). The lateral advection term $-\partial/\partial y \langle \widehat{v}(\partial \widehat{u}/\partial y) \rangle$ only contributes to the depth-averaged lateral shear budget in the later half of the ebb (Figure 5.11b). This term acts as a source of lateral shear (positive sign) at the edge of the shoal (between $y = -400\,\text{m}$ and $y = -200\,\text{m}$) starting around $t = 68.0\,\text{days}$, and as a sink (negative sign) on the shoal (between $y = -600\,\text{m}$ and $y = -400\,\text{m}$; Figure 5.11b). Similarly, the vertical advection term $-\partial/\partial y \langle \widehat{w} \partial \widehat{u}/\partial z \rangle$ does not become significant until the end of the ebb $t \geq 68.0\,\text{days}$ and acts then as a sink over the lower half of the slope, between $y = -200\,\text{m}$ and $y = 0\,\text{m}$ (Figure 5.11c). These results suggest that the late

ebb convergence front is responsible for the compression of the shear layer at the edge of the shoal observed on Figure 5.10, by strengthening the lateral shear at the edge of the shoal and weakening it around the edge. Finally the residual is also a main contributor of the lateral shear budget throughout the ebb (Figure 5.11e). This residual term appears to be consistent with a lateral mixing term $-\partial/\partial y \left\langle \partial \tau_{yx}/\partial y \right\rangle$, acting as the main sink of lateral shear at the edge of the shoal.

Summary

To summarize, a budget for the depth-averaged lateral shear $\partial \left\langle \widehat{u} \right\rangle / \partial y$ was derived in this section, under the main assumption that the longitudinal pressure gradient is invariant at the scale of the shoal-channel interface. All terms of this budget can be estimated from velocity observations collected during the transect surveys, except for the lateral mixing of longitudinal momentum u which is inferred as the residual of the budget. During the weaker tide (27 February 2009), we find that the lateral mixing term is weaker and less spatially and temporally coherent than during the stronger tides (05 March and 09 March 2009). During these stronger tides, the friction term but also the advective terms are stronger as a result of the lateral circulation and convergence fronts developing at the interface. These results suggest that lateral mixing is sensitive to the lateral flow and as a result can display a similar spatial and temporal variability.

5.2 Analysis of Horizontal Mixing

Eddy viscosity and mixing length models

By analogy with viscous stresses, SFS stresses are frequently assumed to be proportional to the local velocity gradient (Speziale 1991). In the case of the lateral SFS stress τ_{yx}, this eddy-viscosity assumption yields

$$\tau_{yx} = -\nu_y \frac{\partial \widehat{u}}{\partial y} \tag{5.19}$$

The lateral mixing term in (5.15) becomes then

$$-\frac{\partial}{\partial y}\left\langle \frac{\partial \tau_{xy}}{\partial y} \right\rangle = \frac{\partial}{\partial y}\left\langle \frac{\partial}{\partial y}\left(\nu_y \frac{\partial \widehat{u}}{\partial y} \right) \right\rangle \tag{5.20}$$

A typical approach to scale mixing coefficients such as eddy viscosities and diffusivities is to use a mixing length model:

$$\nu_y = l_m v_m \tag{5.21}$$

where v_m is a characteristic mixing velocity and l_m is a characteristic mixing lengthscale. For turbulent flows, the square root of the turbulent kinetic energy $k^{1/2}$ is frequently used as the characteristic velocity (Pope 2000) and the size of the largest, energy-containing eddies

is usually used as the characteristic lengthscale. In the following subsections, we explore two different mixing velocity and lengthscale models associated with the two horizontal mixing processes at the shoal-channel interface: bottom boundary layer turbulence and horizontal shear instabilities.

Bottom boundary layer mixing

In channel flows, the scaling commonly used for the lateral eddy viscosity associated with bottom-generated turbulence (Fischer et al. 1979) uses the bed friction velocity as the mixing velocity scale v_m and a fraction of the water depth as the mixing lengthscale l_m:

$$\nu_y^{'}(y) = \underbrace{0.1H(y)}_{l_m} \underbrace{(C_D)^{1/2} \langle \widehat{u} \rangle (y)}_{v_m} \tag{5.22}$$

where C_D is the constant bottom drag coefficient introduced in (5.5). Substituting (5.22) in (5.20) yields

$$-\frac{\partial}{\partial y} \left\langle \frac{\partial \tau_{xy}}{\partial y} \right\rangle = 0.1(C_D)^{1/2} \frac{\partial}{\partial y} \left\langle \frac{\partial}{\partial y} \left(H \langle \widehat{u} \rangle \frac{\partial \widehat{u}}{\partial y} \right) \right\rangle \tag{5.23}$$

The right hand side of this equation can be estimated with the observations and compared to the observed lateral mixing term as estimated by the residual defined in (5.18). The observations show that this model (5.23) yields an estimate of the lateral mixing term (Figures 5.12b, 5.13b, 5.14b) about three order of magnitude smaller ($\sim 10^{-9}\,\mathrm{s}^{-2}$) than the residual (Figures 5.12a, 5.13a, 5.14a) for all three transect surveys. These results suggest that bed-generated turbulence is not a significant horizontal mixing process at the shoal-channel interface.

Horizontal shear instabilities

When a transverse horizontal shear $\partial\widehat{u}/\partial y$ is present, another scaling for ν_y can be constructed, using the width δ of the shear layer for the mixing lengthscale l_m. Following VanProoijen et al. (2005), we use for the mixing velocity scale the velocity difference across the shear region $\Delta\widehat{u} = \delta\,|\partial\widehat{u}/\partial y|$ scaled by the water depth:

$$v_m = \delta \frac{H_m}{H(y)} \left| \frac{\partial \widehat{u}}{\partial y} \right| \tag{5.24}$$

The introduction of the ratio $H_m/H(y)$ is motivated by volume conservation along the perimeter of the horizontal coherent structures resulting from the shear instability: the characteristic velocity v_m is greater on the shallow side of the interface (shoal) and smaller on the deeper side (channel).

The eddy viscosity model writes in this case:

$$\nu_y^{''}(y) = \alpha\delta^2 \frac{H_m}{H(y)} \left| \frac{\partial \widehat{u}}{\partial y} \right| \tag{5.25}$$

where α is a fitting parameter. Typical values for this fitting parameter are around $\alpha \simeq 0.01$ (VanProoijen et al. 2005). Substituting (5.25) in (5.20) yields finally the following model for lateral mixing associated with horizontal shear instabilities:

$$-\frac{\partial}{\partial y}\left\langle\frac{\partial \tau_{xy}}{\partial y}\right\rangle = \alpha\delta^2\frac{\partial}{\partial y}\left\langle\frac{\partial}{\partial y}\left(\frac{H_m}{H}\left|\frac{\partial \widehat{u}}{\partial y}\right|\frac{\partial \widehat{u}}{\partial y}\right)\right\rangle \tag{5.26}$$

We used $H_m = 8\,\mathrm{m}$ for the mean depth at the interface, $\alpha = 0.01$ and the width of the slope as the characteristic width of the shear layer $\delta = 400\mathrm{m}$. This model yields a lateral mixing term with magnitudes in the range $1 - 3 \times 10^{-7}\,\mathrm{s}^{-2}$ (Figures 5.12c, 5.13c, 5.14c), a factor 4 smaller than the residual but two orders of magnitude greater than the boundary layer model (5.23). These results suggest that lateral mixing at the interface quantified by the residual is driven primarily by horizontal coherent structures associated with lateral shear instabilities. The eddy viscosity model (5.26) performs well for the 09 March 2009 survey (Figure 5.14c), when the shear layer is stronger and not subject to large intratidal variations (Figure 5.10). However, this model does not compare favorably with the residual during the 27 February 2009 survey (Figure 5.12c) when the shear layer was weaker (Figure 5.5), or during the 05 March 2009 survey (Figure 5.13c) when the shear layer was characterized by large intratidal variations (Figure 5.7). These discrepancies can be explained by the fact that the model (5.25) assumes a steady shear layer, which is not the case during the 27 February and 05 March surveys. During the 09 March 2009 survey, the lateral eddy viscosity ν_y was estimated from equation (5.25) with a fitting parameter $\alpha = 0.04$ which yields a best fit between the model (5.26) and the residual. We find that ν_y is largest at the edge of the shoal between $y = -500\,\mathrm{m}$ and $y = -300\,\mathrm{m}$ (Figure 5.15a). Peak values of ν_y are about $7\,\mathrm{m}^2\,\mathrm{s}^{-1}$ during the flood and $15\,\mathrm{m}^2\,\mathrm{s}^{-1}$ during the ebb.

5.3 Summary

An analytical framework was developed to estimate transverse mixing of longitudinal momentum $\widehat{u}$ at the shoal-channel interface. This framework is based on a budget for the lateral shear $\partial\widehat{u}/\partial y$. In the case of a straight, shallow and narrow (compared to the basin scale and tidal wavelength) shoal-channel interface, the pressure gradient is assumed invariant at the scale of the interface and a lateral mixing term can then be estimated as the residual of the lateral shear budget. The observations show that while lateral shear $\partial\widehat{u}/\partial y$ is initiated by lateral variations in friction, the lateral and vertical advection terms play an important role especially during the ebb when convergence fronts develop at the interface. In other words, the lateral shear is found to be sensitive to the lateral dynamics. The residual term interpreted as the lateral mixing term is found to be also contributing at leading order in all three surveys.

This residual is compared to two models based on the eddy viscosity assumption. The first model uses a parametrization of the lateral eddy viscosity ν_y based on water depth and friction velocity and therefore quantifies the contribution of bottom boundary layer

turbulence to horizontal mixing. The second model uses a parametrization based on the width of the shear layer and the horizontal velocity difference across the shear layer and therefore quantifies the contribution of horizontal shear instabilities to horizontal mixing. We find that the first model is three order of magnitude smaller than the residual but the second model is of same order of magnitude. These results suggest that horizontal shear instabilities are the dominant horizontal mixing process at the interface, in part because the lengthscale of the horizontal shear instabilities is not restricted by depth and therefore much larger than the mixing length associated with the bottom boundary layer. This second model compares favorably with the residual during the 09 March 2009 transect survey when the shear $\partial\widehat{u}/\partial y$ was strongest and quasi-steady (no intratidal variations), but not during the first two winter surveys when the shear $\partial\widehat{u}/\partial y$ was more spatially and temporally variable.

To conclude, this work introduces a new approach to quantifying horizontal mixing at a straight, narrow shoal-channel interface and highlights the important role of lateral dynamics in forcing intratidal variations of horizontal mixing. While the existing analytical model is appropriate for quasi-steady lateral shear layer, it fails to reproduce this intratidal variability. We recommend therefore to include variables relevant to lateral dynamics such as the lateral convergence rate $\partial\widehat{v}/\partial y$ in future parametrization efforts.

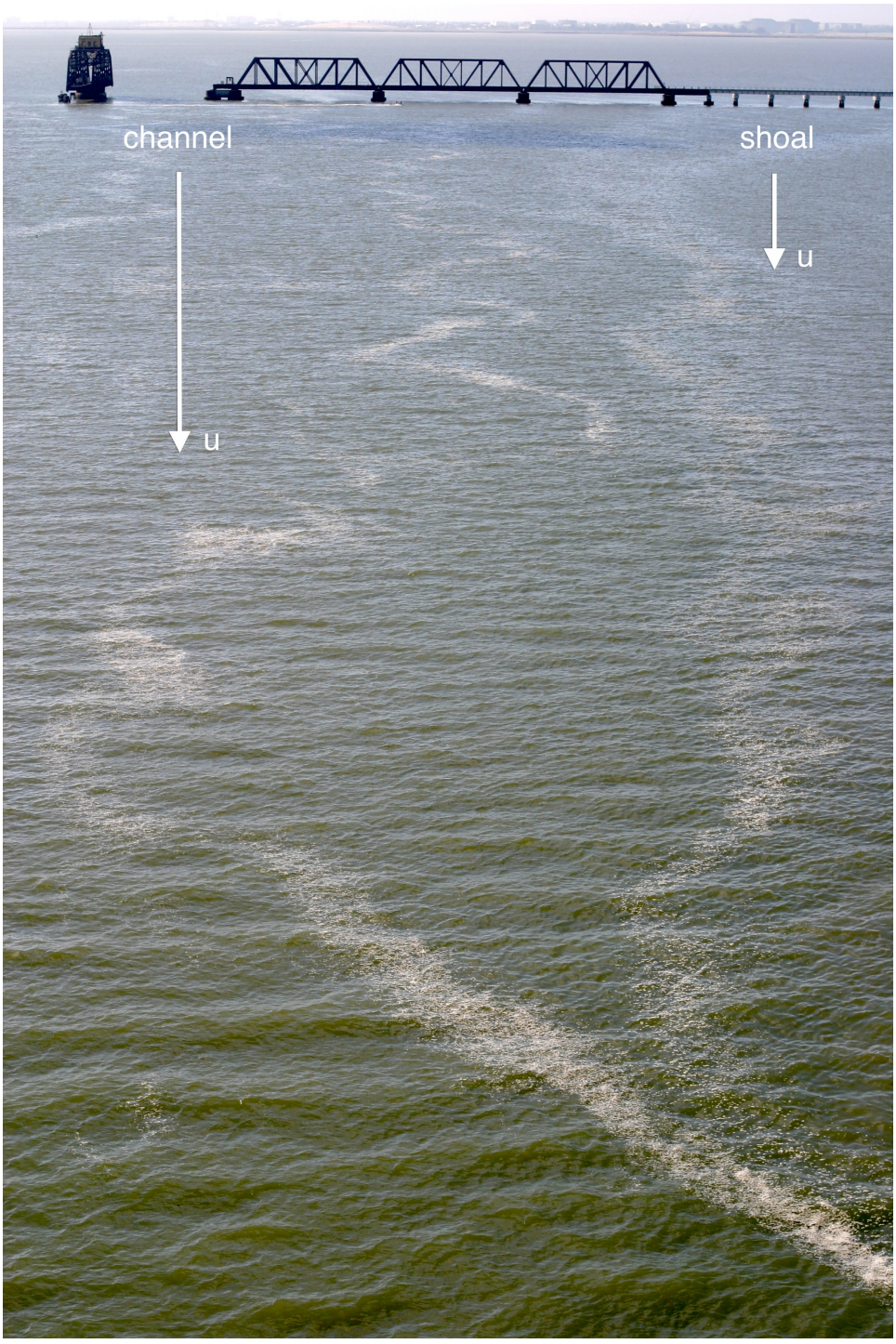

Figure 5.1: Surface fronts at the shoal-channel interface during an ebb tide. The view is to the South, looking from Dumbarton Bridge in South San Francisco Bay. The arrows represent the direction of the principal current direction u (not to scale). Some of the fronts visible might be generated by other bathymetric features upstream.

Figure 5.2: Surface fronts at the shoal-channel interface during an ebb tide. The view is to the South, looking from Dumbarton Bridge in South San Francisco Bay. The arrows represent the direction of the principal current direction u (not to scale).

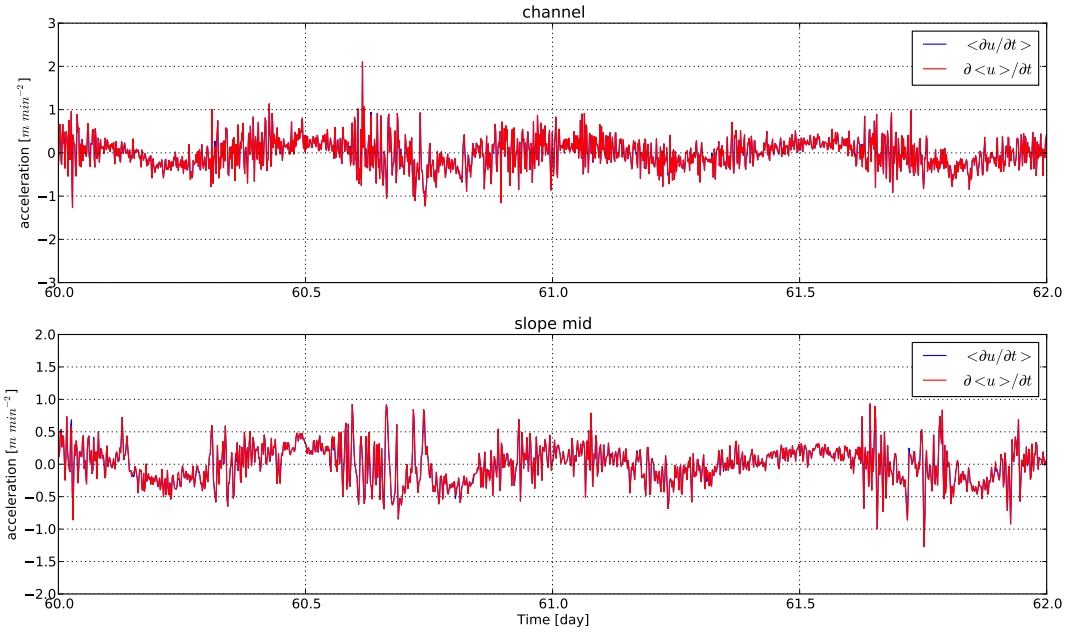

Figure 5.3: Time derivative of the depth-averaged velocity $\partial \langle u \rangle / \partial t$ (red) and depth-averaged acceleration $\langle \partial u / \partial t \rangle$ (blue) in the channel (top) and on the slope (bottom).

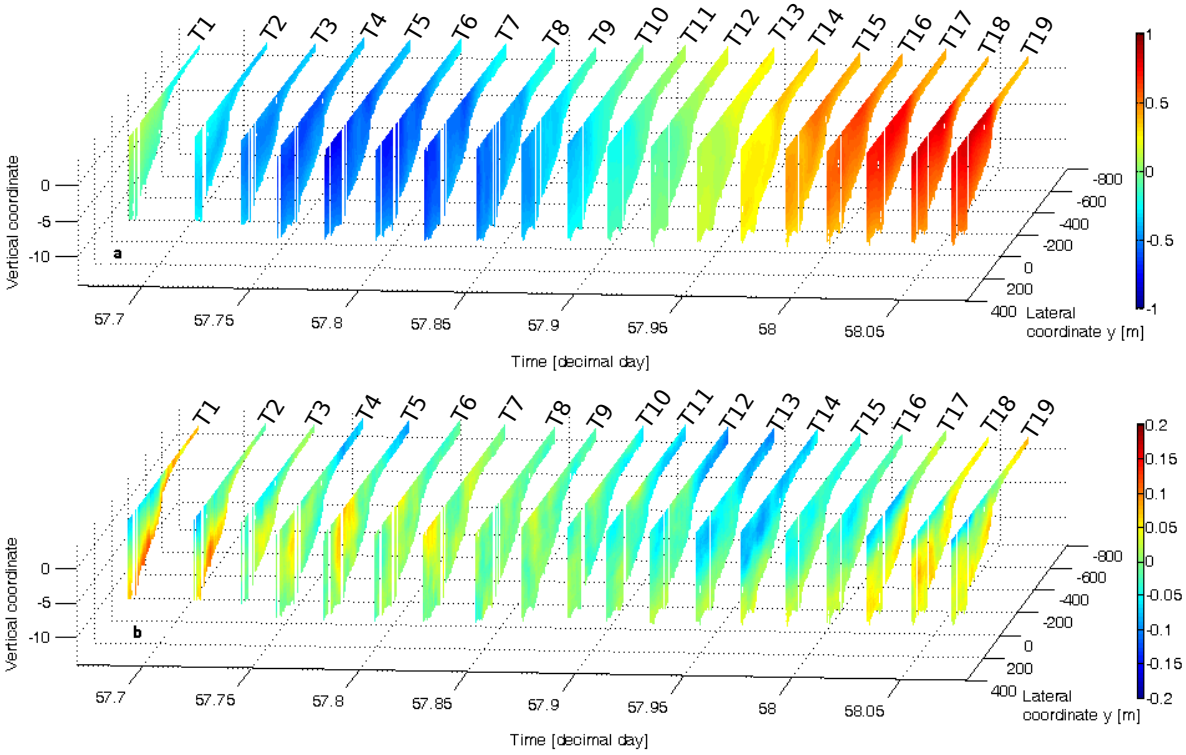

Figure 5.4: Low-pass filtered longitudinal velocity $\widehat{u}$ in $\mathrm{m\,s^{-1}}$ (a) and lateral velocity $\widehat{v}$ in $\mathrm{m\,s^{-1}}$ (b) during the 27 February 2009 survey. The time between two transects is about thirty minutes.

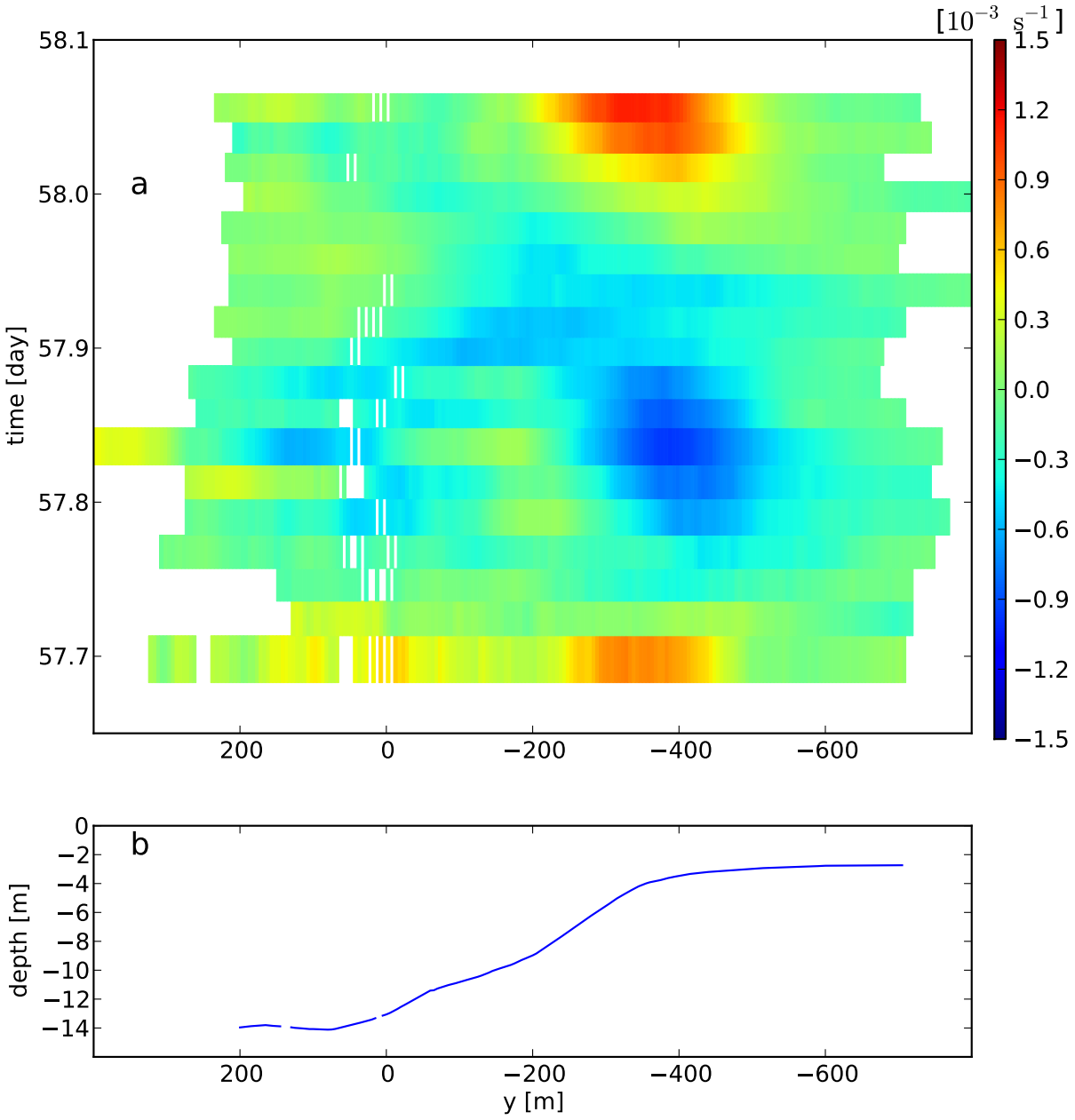

Figure 5.5: Bathymetry (b) and depth-averaged the lateral shear $\partial \langle \widehat{u} \rangle / \partial y$ (a) during the 27 February 2009 transect survey

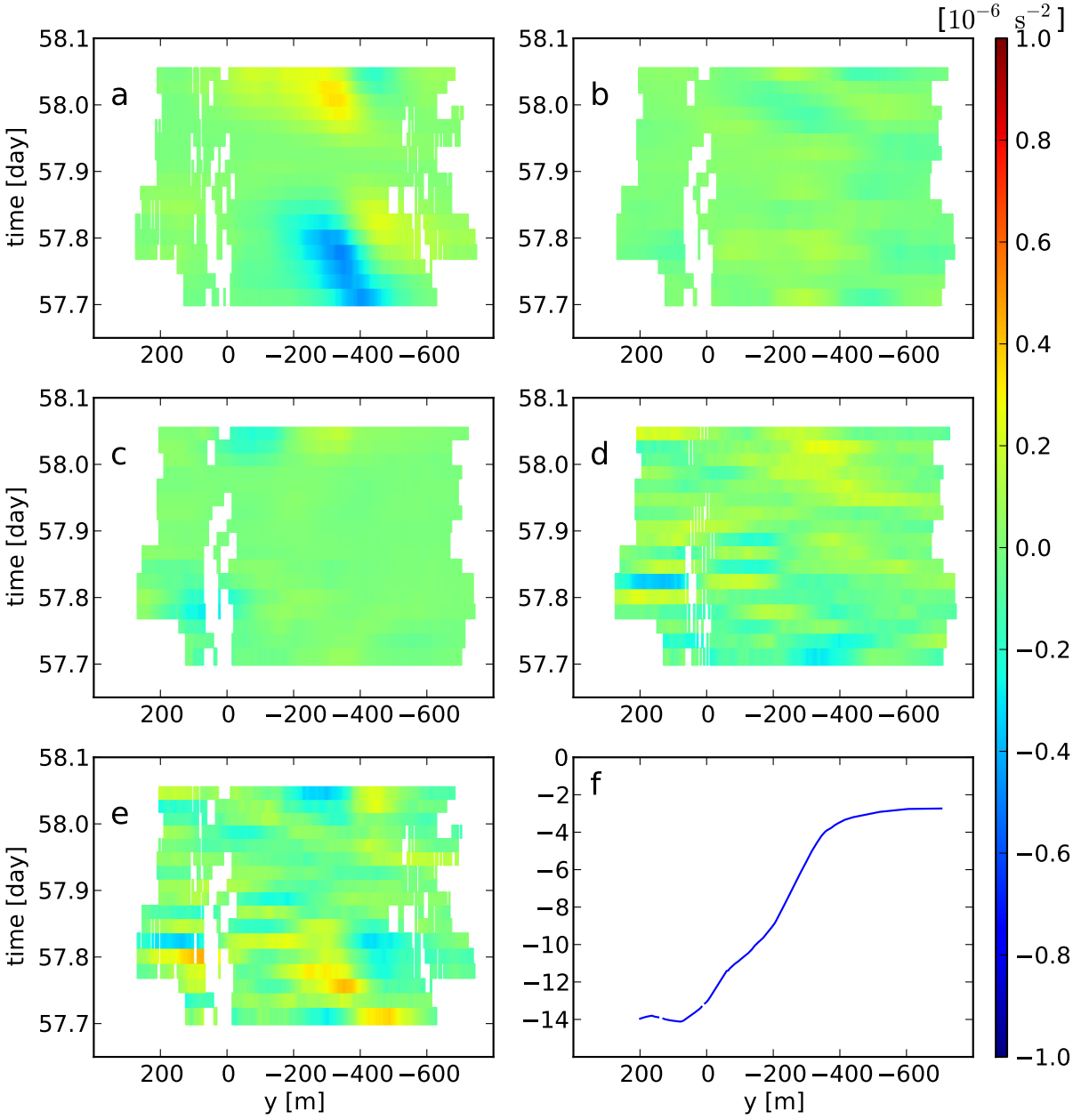

Figure 5.6: Terms of the lateral shear budget (5.15) during the 27 February 2009 survey: friction term $-C_D \left|\langle \widehat{u} \rangle\right| / (H+\eta) \left[2\partial \langle \widehat{u} \rangle / \partial y - \langle \widehat{u} \rangle (dH/dy)/(H+\eta)\right]$ (a), lateral advection term $-\partial/\partial y \langle \widehat{v}(\partial \widehat{u}/\partial y) \rangle$ (b), vertical advection term $-\partial/\partial y \langle \widehat{w}(\partial \widehat{u}/\partial z) \rangle$ (c), unsteadiness term $\partial/\partial t \left(\partial \langle \widehat{u} \rangle / \partial y\right)$ (d), residual as defined in (5.18) (e) and bathymetry $-H(y)$ (f).

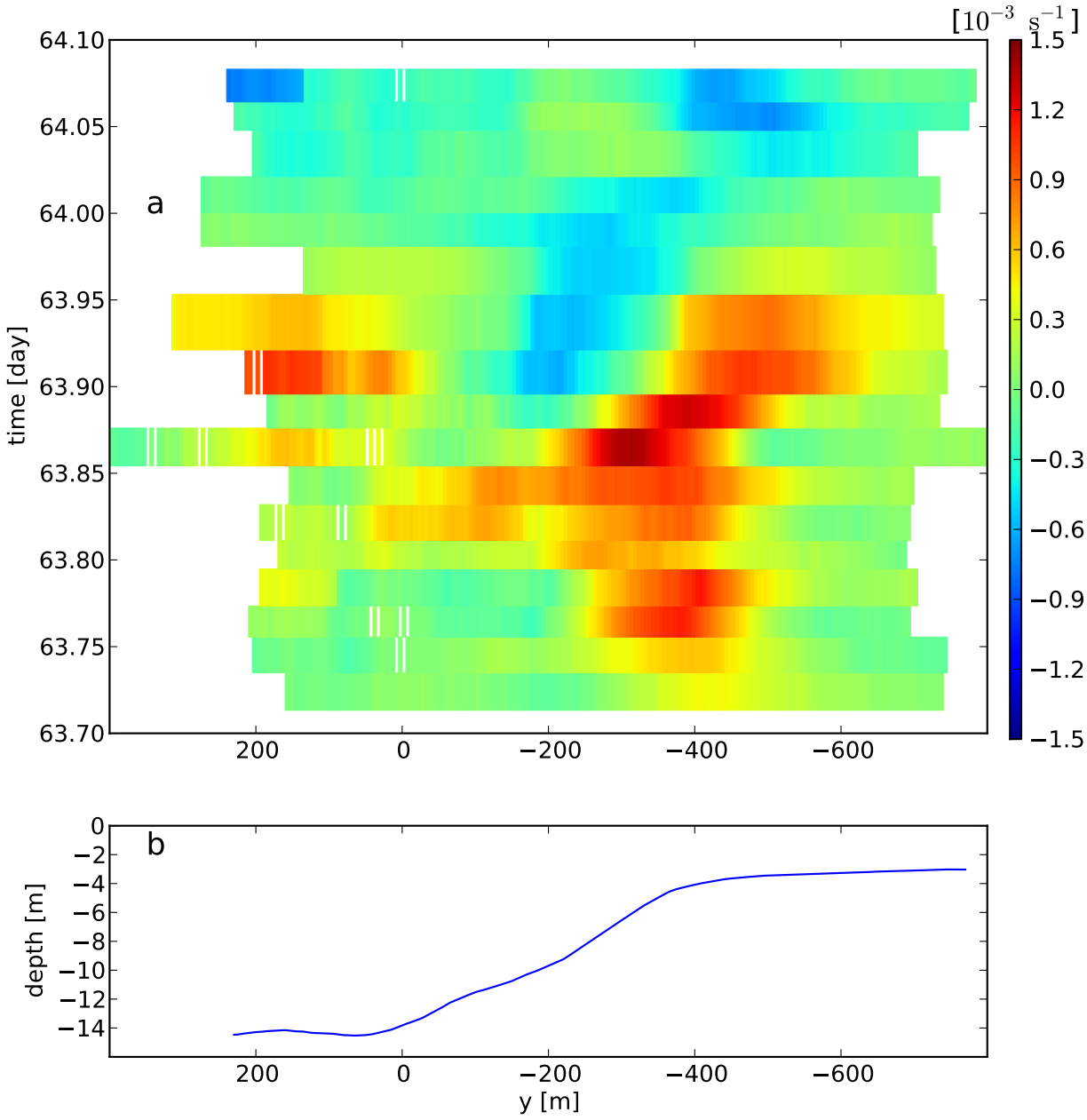

Figure 5.7: Bathymetry (b) and depth-averaged the lateral shear $\partial \langle \widehat{u} \rangle / \partial y$ (a) during the 05 March 2009 transect survey

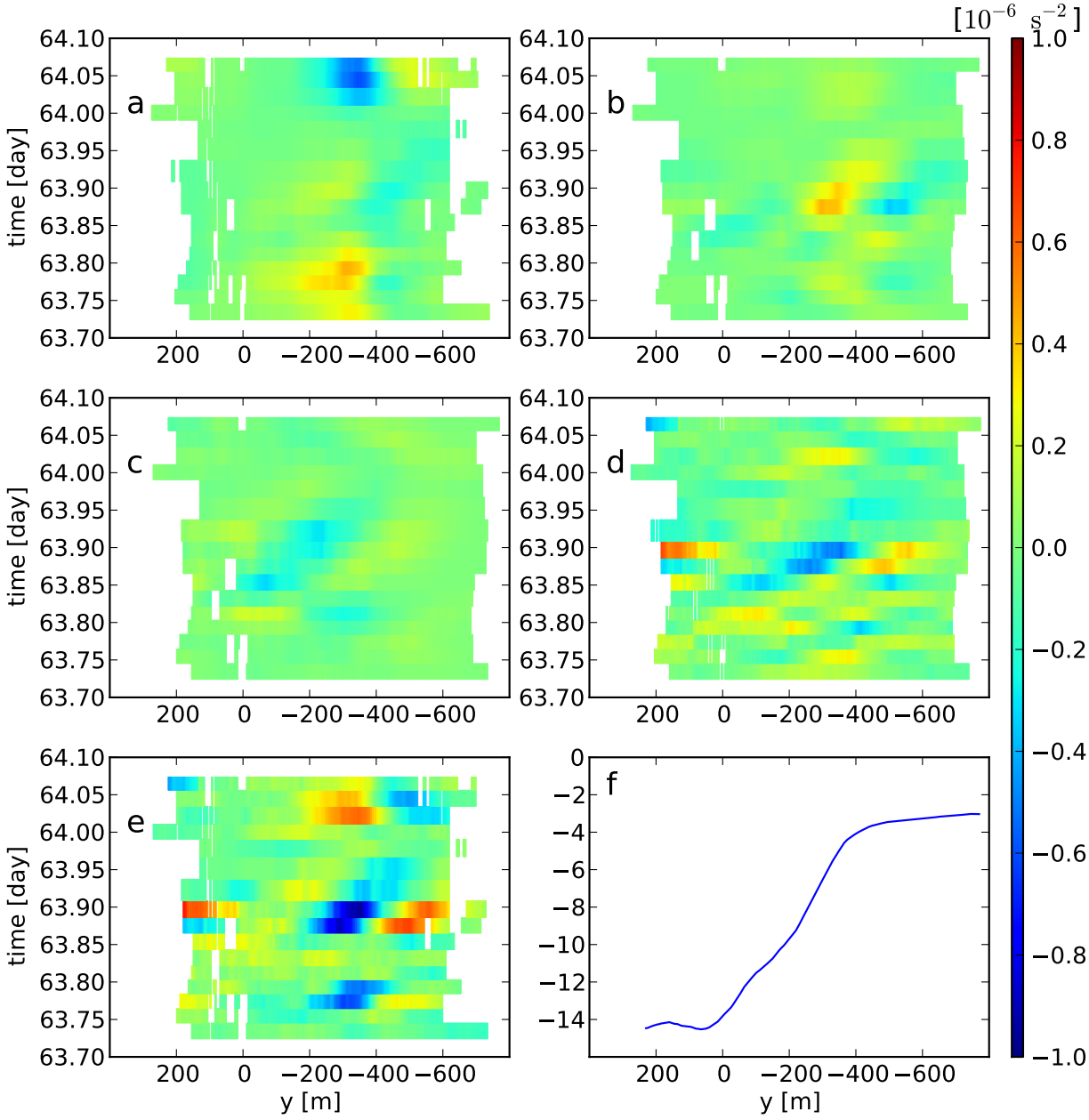

Figure 5.8: Terms of the lateral shear budget (5.15) during the 05 March 2009 survey: friction term $-C_D \left|\langle \widehat{u} \rangle\right| / (H+\eta) \left[2\partial \langle \widehat{u} \rangle / \partial y - \langle \widehat{u} \rangle (dH/dy)/(H+\eta)\right]$ (a), lateral advection term $-\partial/\partial y \langle \widehat{v}(\partial \widehat{u}/\partial y) \rangle$ (b), vertical advection term $-\partial/\partial y \langle \widehat{w}(\partial \widehat{u}/\partial z) \rangle$ (c), unsteadiness term $\partial/\partial t \left(\partial \langle \widehat{u} \rangle / \partial y\right)$ (d), residual as defined in (5.18) (e) and bathymetry $-H(y)$ (f).

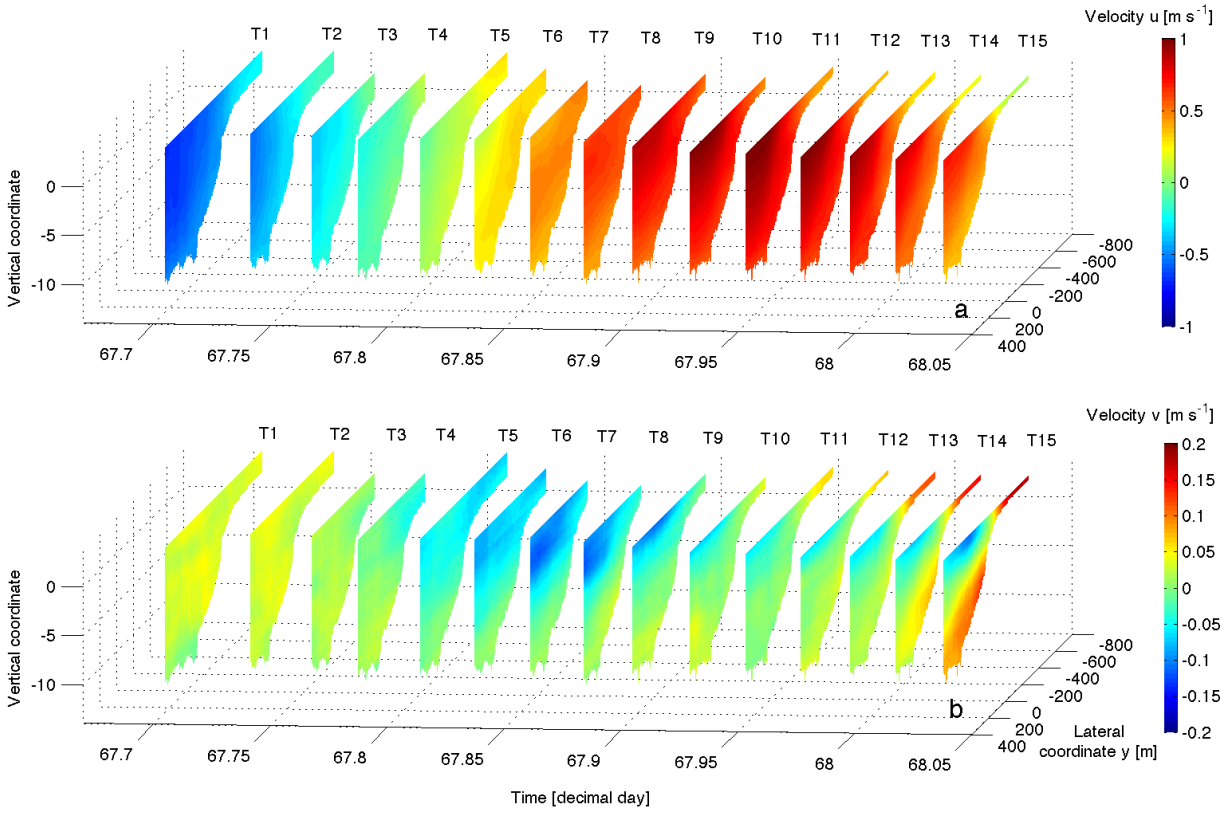

Figure 5.9: Low-pass filtered longitudinal velocity $\widehat{u}$ (a) and lateral velocity $\widehat{v}$ (b) during the 09 March 2009 survey. The time between two transects is about thirty minutes.

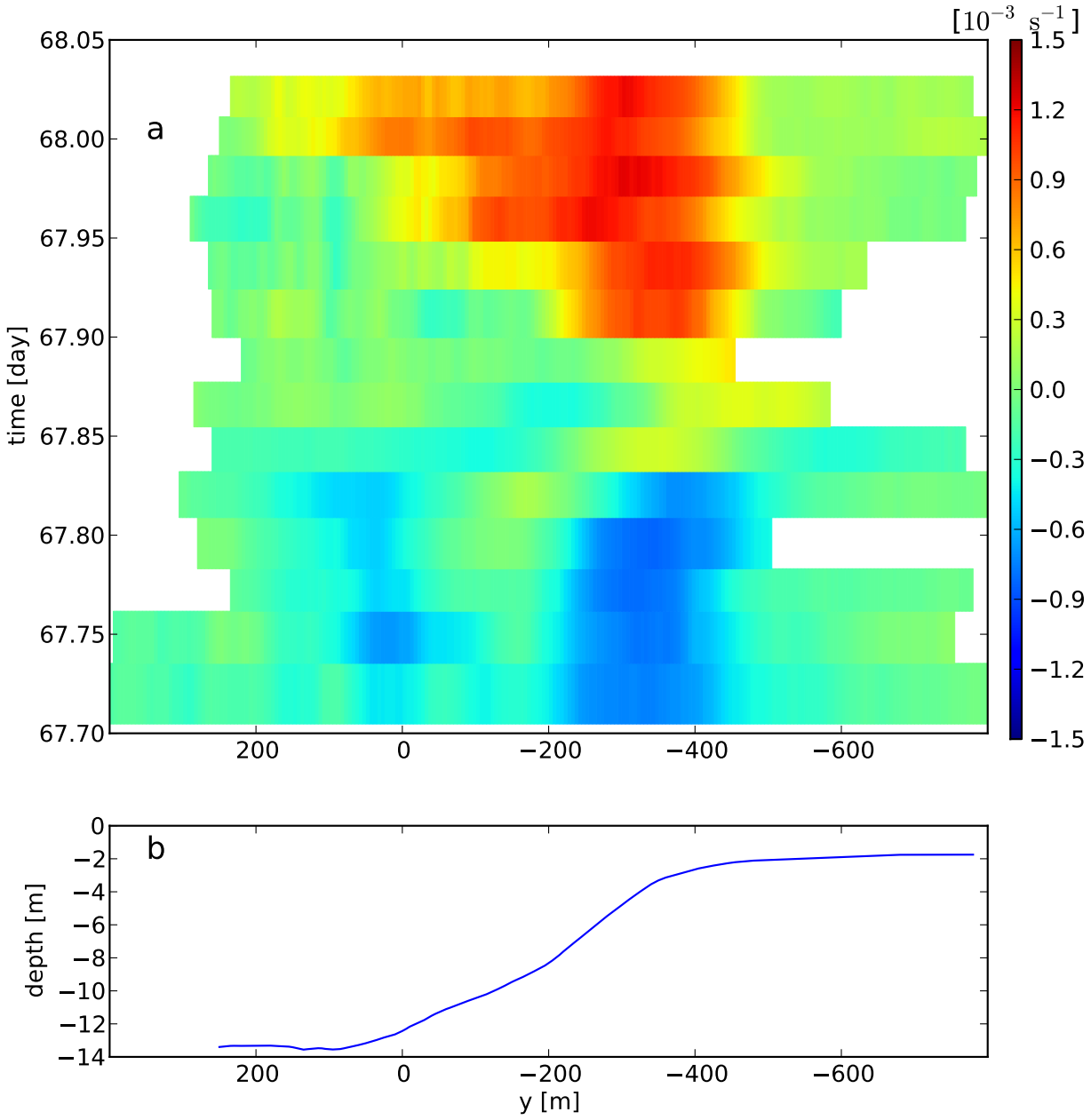

Figure 5.10: Bathymetry (b) and depth-averaged the lateral shear $\partial \langle \hat{u} \rangle / \partial y$ (a) during the 09 March 2009 transect survey

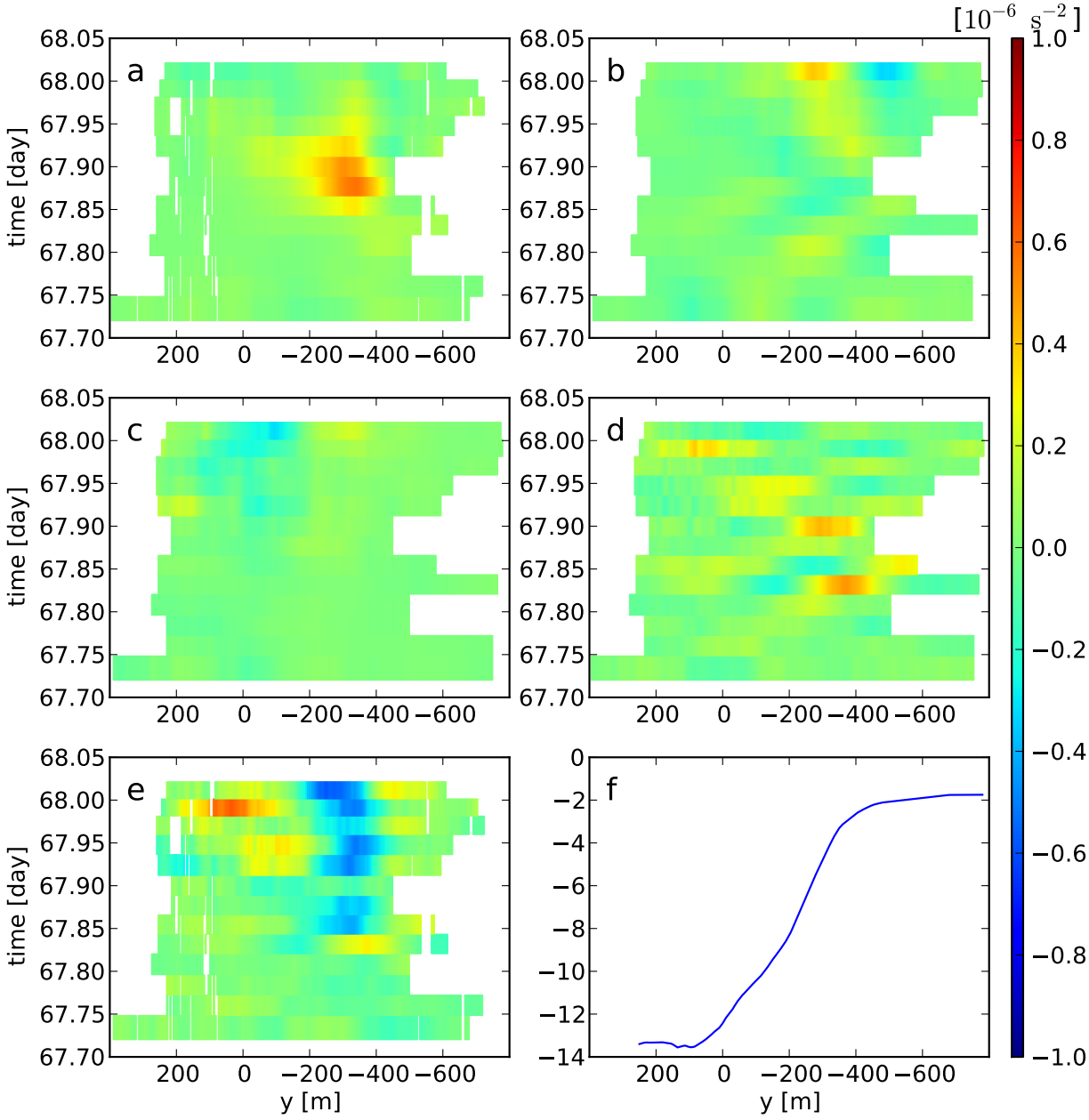

Figure 5.11: Terms of the lateral shear budget (5.15) during the 09 March 2009 survey: friction term $-C_D \left|\langle\widehat{u}\rangle\right| / (H+\eta) \left[2\partial \langle\widehat{u}\rangle / \partial y - \langle\widehat{u}\rangle (dH/dy)/(H+\eta)\right]$ (a), lateral advection term $-\partial/\partial y \langle\widehat{v}(\partial\widehat{u}/\partial y)\rangle$ (b), vertical advection term $-\partial/\partial y \langle\widehat{w}(\partial\widehat{u}/\partial z)\rangle$ (c), unsteadiness term $\partial/\partial t \left(\partial \langle\widehat{u}\rangle / \partial y\right)$ (d), residual as defined in (5.18) (e) and bathymetry $-H(y)$ (f).

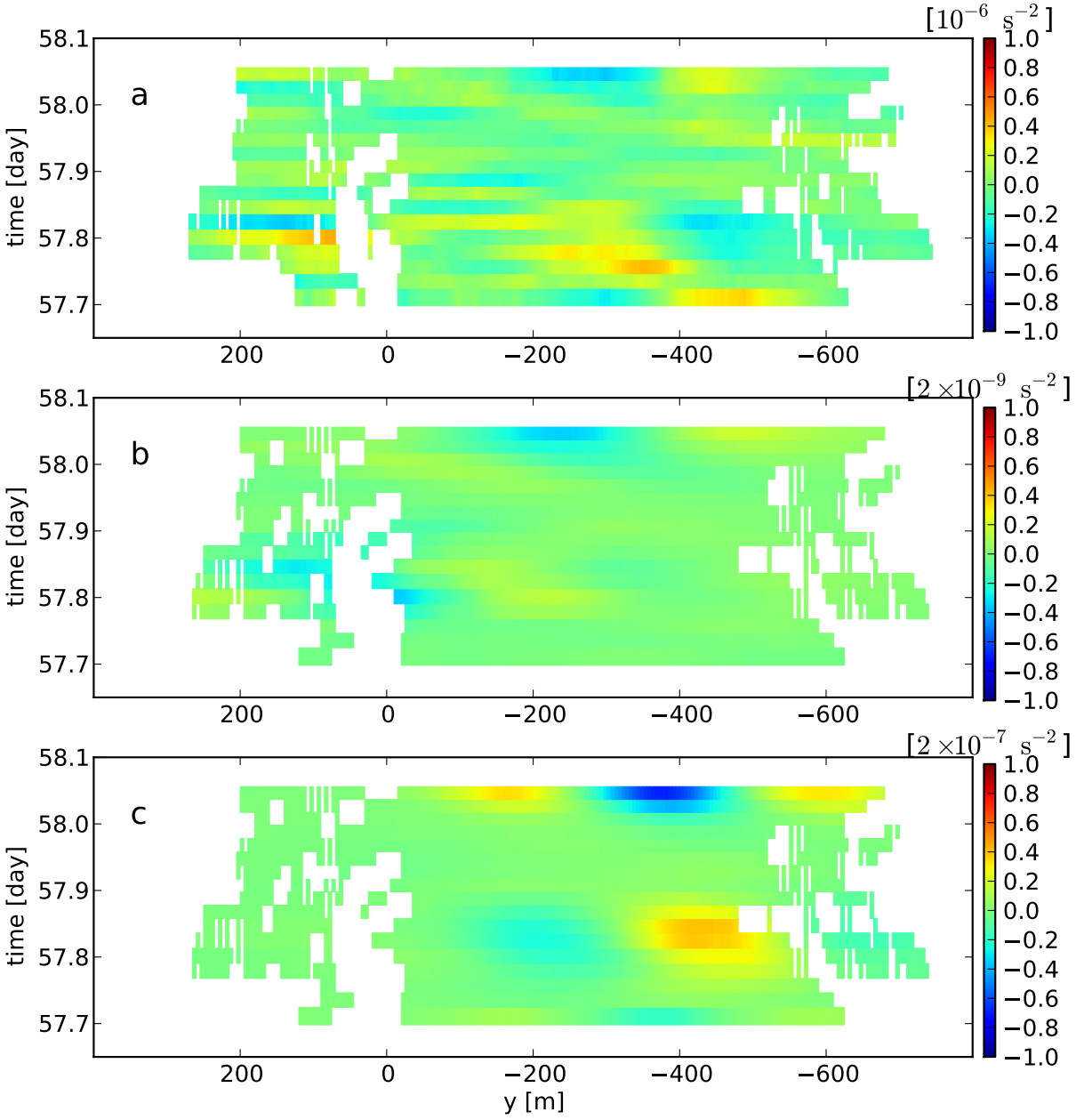

Figure 5.12: Analysis of horizontal mixing during the 27 February 2009 transect survey: (a) residual term as defined in (5.18), lateral mixing model associated with (b) the bottom boundary layer (equation 5.23) and (c) horizontal shear instabilities (equation 5.26).

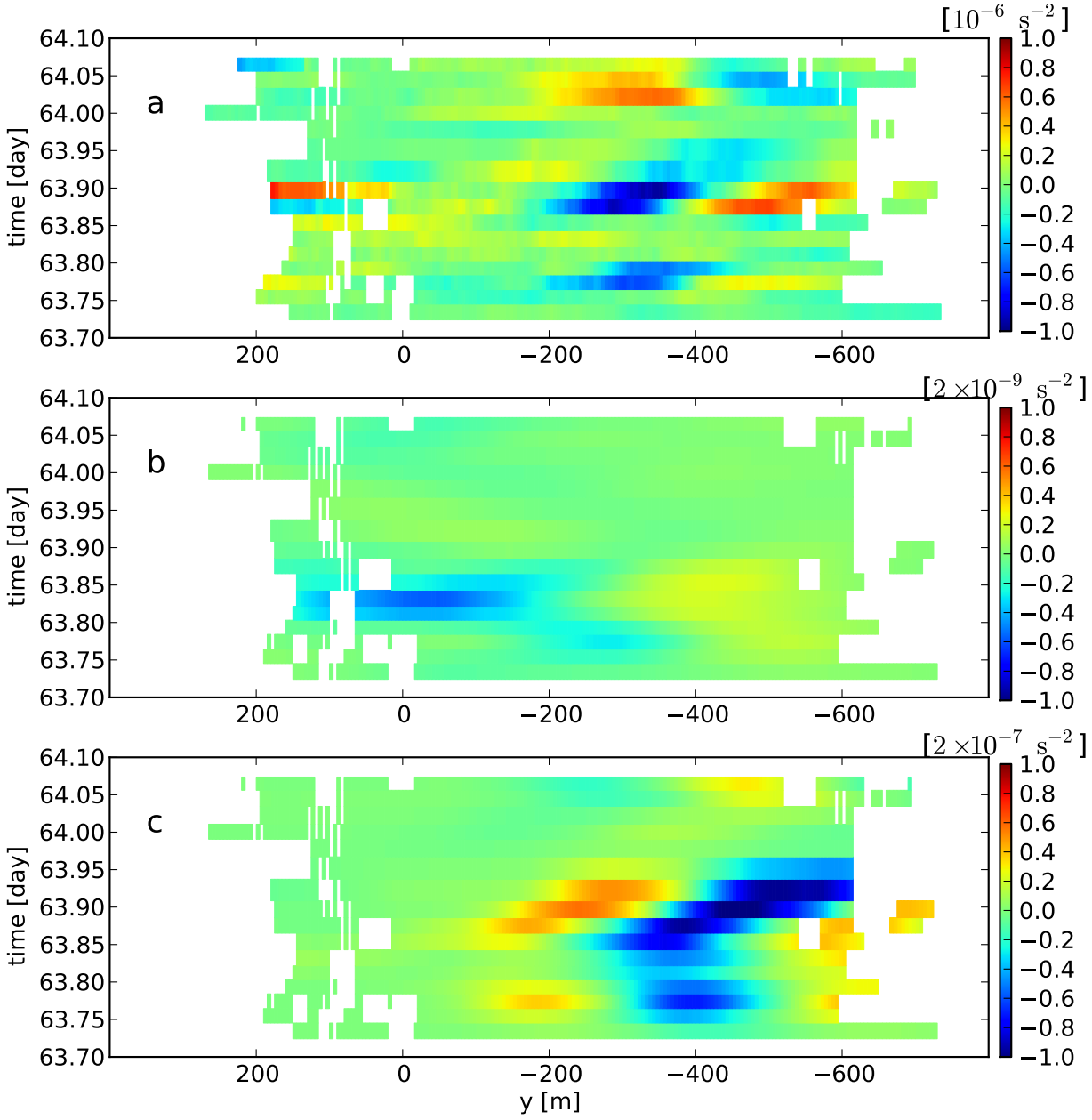

Figure 5.13: Analysis of horizontal mixing during the 05 March 2009 transect survey: (a) residual term as defined in (5.18), lateral mixing model associated with (b) the bottom boundary layer (equation 5.23) and (c) horizontal shear instabilities (equation 5.26).

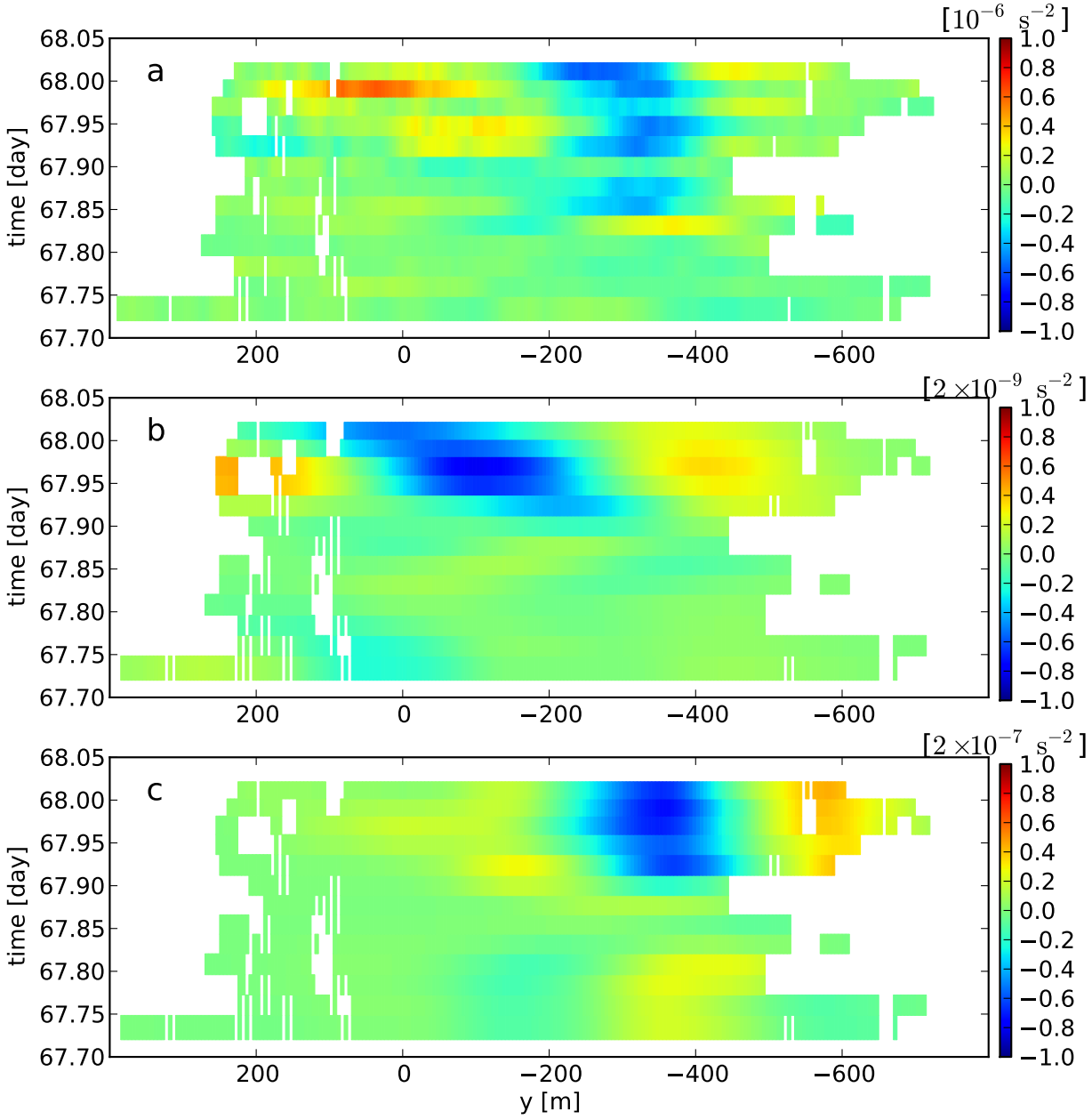

Figure 5.14: Analysis of horizontal mixing during the 09 March 2009 transect survey: (a) residual term as defined in (5.18), lateral mixing model associated with (b) the bottom boundary layer (equation 5.23) and (c) horizontal shear instabilities (equation 5.26).

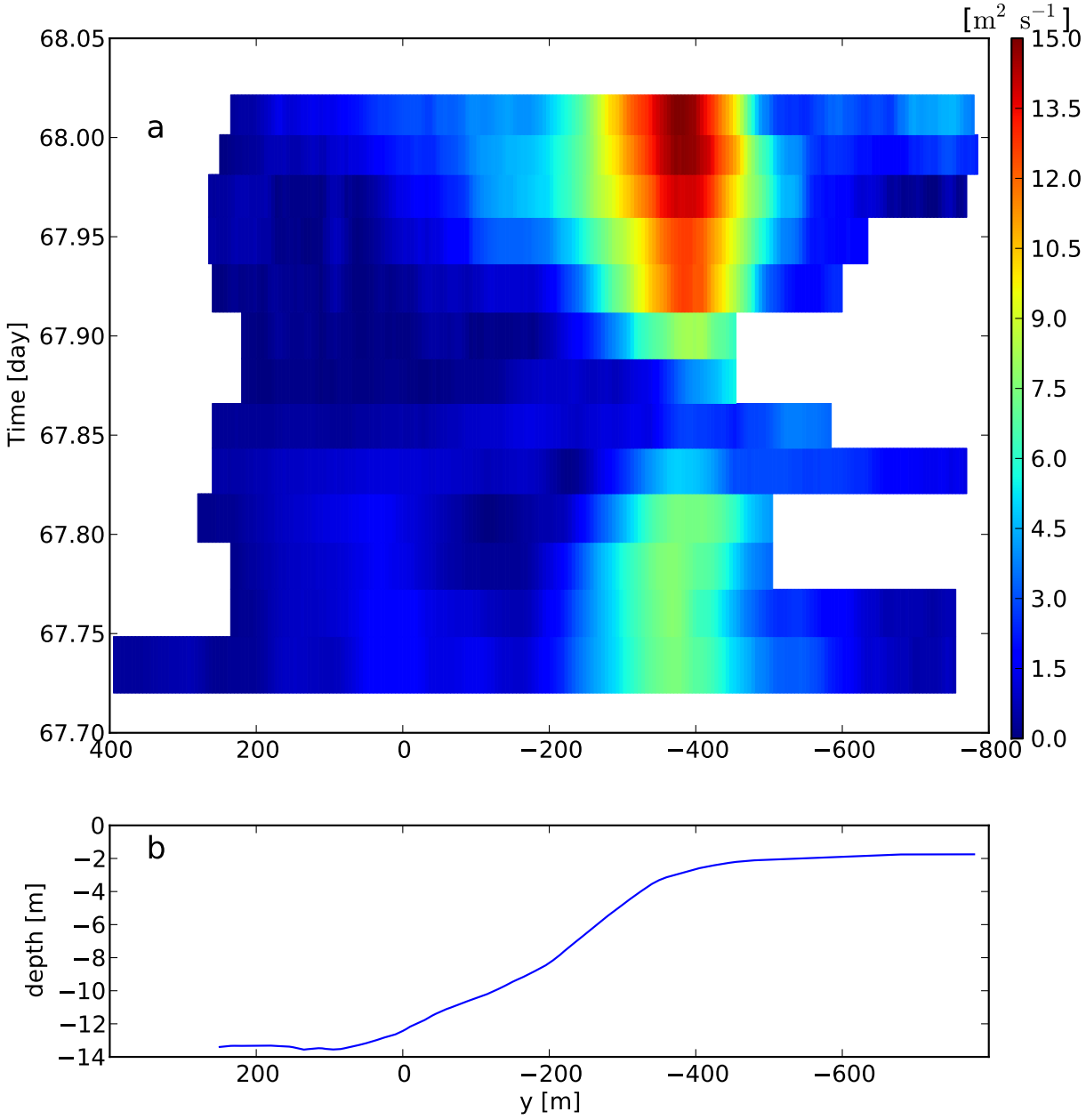

Figure 5.15: Analysis of horizontal mixing during the 09 March 2009 transect survey: horizontal eddy viscosity $\nu_y(y,t)$ (a) associated with horizontal shear instabilities (equation 5.25) and bathymetry (b).

Chapter 6

Conclusion

Transport and mixing processes at the shoal-channel interface in partially-stratified conditions are characterized by important intratidal variations with typical timescales between one and two hours. These intratidal variations are driven predominantly by the evolution of the transverse density gradient at the interface. It is therefore crucial that numerical models addressing shoal-channel exchange reproduce this evolution, which will require accurate horizontal advection and vertical mixing of salinity. In particular, the slope between channel and shoal should be treated as a third separate region rather than a monotonic transition or discontinuous interface because different physical processes are at play in this region. Chief among them are the lateral advection of momentum and scalars, the straining of transverse gradients by the lateral circulation, and horizontal shear instabilities.

These physical processes are characterized by horizontal and vertical length scales smaller than those relevant to the processes in the channel and on the shoal. Spatial resolution of numerical models should therefore reflect this constraint. We recommend using grid spacings $\leq 10\,\mathrm{m}$ in the horizontal plane and $\leq 0.5\,\mathrm{m}$ in the vertical direction to reliably reproduce horizontal and vertical gradients at the shoal-channel interface.

Existing zero-equation models for horizontal eddy viscosity based on the width of the interface and the horizontal shear appear to be appropriate for quasi-steady lateral shear varying only tidally, but fall short to reproduce the observed intratidal variations of horizontal mixing at the shoal-channel interface. We recommend that, similarly to vertical eddy viscosity and diffusivities, one or two equations dynamical models for the horizontal eddy viscosity and diffusivities be pursued to account for the unsteady nature of horizontal shears and mixing in this system.

Bibliography

Banas, NS, P MacCready, and BM Hickey (2009). "The Columbia River plume as cross-shelf exporter and along-coast barrier". *Cont Shelf Res* 29.1, pp. 292–301.

Basak, S and S Sarkar (2006). "Dynamics of a stratified shear layer with horizontal shear". *J Fluid Mech* 568, pp. 19–54.

Burchard, H, O Petersen, and TP Rippeth (1998). "Comparing the performance of the Mellor-Yamada and the k-epsilon two-equation turbulence models". *J Geophys Res* 103.C5, pp. 10543–10554.

Chant, RJ, WR Geyer, R Houghton, E Hunter, and J Lerczak (2007). "Estuarine boundary layer mixing processes: Insights from dye experiments". *J Phys Oceanogr* 37.7, pp. 1859–1877.

Chen, S and LP Sanford (2008). "Lateral circulation driven by boundary mixing and the associated transport of sediments in idealized partially mixed estuaries". *Cont Shelf Res* 29.1, pp. 101–118.

Chen, S, LP Sanford, and DK Ralston (2009). "Lateral circulation and sediment transport driven by axial winds in an idealized, partially mixed estuary". *J Geophys Res* 114, p. C12006.

Cheng, P, RE Wilson, RJ Chant, DC Fugate, and RD Flood (2009). "Modeling Influence of Stratification on Lateral Circulation in a Stratified Estuary". *J Phys Oceanogr* 39.9, pp. 2324–2337.

Cheng, RT and JW Gartner (1985). "Harmonic-analysis of tides and tidal currents in South San Francisco bay, California". *Estuar Coast Shelf S* 21.1, pp. 57–74.

Clarke, LB, D Ackerman, and J Largier (2007). "Dye dispersion in the surf zone: Measurements and simple models". *Cont Shelf Res* 27.5, pp. 650–669.

Deloncle, A, JM Chomaz, and P Billant (2007). "Three-dimensional stability of a horizontally sheared flow in a stably stratified fluid". *J Fluid Mech* 570, pp. 297–305.

Erdogan, ME and PC Chatwin (1967). "The effects of curvature and buoyancy on the laminar dispersion of solute in a horizontal tube". *J Fluid Mech* 29.3, pp. 465–484.

Farmer, D, R Pawlowicz, and R Jiang (2002). "Tilting separation flows: a mechanism for intense vertical mixing in the coastal ocean". *Dynam Atmos Oceans* 36.1-3, pp. 43–58.

Fischer, HB (1972). "Mass transport mechanisms in partially stratified estuaries". *J Fluid Mech* 53.4, pp. 671–687.

Fischer, HB, EJ List, RCY Koh, J Imberger, and NH Brooks (1979). *Mixing in Inland and Coastal Waters*. Academic Press.

Fong, DA and MT Stacey (2003). "Horizontal dispersion of a near-bed coastal plume". *J Fluid Mech* 489, pp. 239–267.

Fugate, DC, CT Friedrichs, and LP Sanford (2007). "Lateral dynamics and associated transport of sediment in the upper reaches of a partially mixed estuary, Chesapeake Bay, USA". *Cont Shelf Res* 27.5, pp. 679–698.

Gargett, AE and JN Moum (1995). "Mixing efficiencies in turbulent tidal fronts - results from direct and indirect measurements of density flux". *Journal of Physical Oceanography* 25.11, pp. 2583–2608.

Garrett, C, P MacCready, and P Rhines (1993). "Boundary mixing and arrested Ekman layers: Rotating stratified flow near a sloping boundary". *Annu Rev Fluid Mech* 25, pp. 291–323.

Geyer, WR (1993). "Three-dimensional tidal flow around headlands". *J Geophys Res* 98.C1, pp. 955–966.

Geyer, WR and DK Ralston (2011). "The Dynamics of Strongly Stratified Estuaries". *Treatise on Estuarine and Coastal Science* 2. Ed. by Wolanski E and McLusky DS, pp. 37–52.

Geyer, WR, JD Woodruff, and P Traykovski (2001). "Sediment Transport and Trapping in the Hudson River Estuary". *Estuaries* 24.5, pp. 670–679.

Geyer, WR, PS Hill, and GC Kineke (2004). "The transport, transformation and dispersal of sediment by buoyant coastal flows". *Cont Shelf Res* 24.7-8, pp. 927–949.

Geyer, WR, ME Scully, and DK Ralston (2008). "Quantifying vertical mixing in estuaries". *Environ Fluid Mech* 8.5-6, pp. 495–509.

Gill, AE (1982). *Atmosphere-Ocean Dynamics*. Academic Press.

Handler, RA, RP Mied, TE Evans, and TF Donato (2001). "Convergence fronts in tidally forced rotating estuaries". *J Geophys Res* 106.C11, pp. 27145–27162.

Handler, RA, RP Mied, GJ Lindemann, and TE Evans (2009). "Turbulent Channel Flows on a Rotating Earth". *J Phys Oceanogr* 39.4, pp. 952–968.

Hansen, DV and M Rattray (1965). "Gravitationnal Circulation in Straits and Estuaries". *J Mar Res* 23.2.

Huijts, KMH, HE de Swart, GP Schramkowski, and HM Schuttelaars (2011). "Transverse structure of tidal and residual flow and sediment concentration in estuaries". *Ocean Dynam* 61.8, pp. 1067–1091.

Huzzey, L and JM Brubaker (1988). "The formation of longitudinal fronts in a coastal-plain estuary". *J Geophys Res* 93.C2, pp. 1329–1334.

Ivey, GN, KB Winters, and JR Koseff (2008). "Density stratification, turbulence, but how much mixing?" *Annu Rev Fluid Mech* 40, pp. 169–184.

Kawanisi, K and S Yokosi (1994). "Mean and turbulence characteristics in a tidal river". *Estuar Coast Shelf S* 38.5, pp. 447–469.

Kundu, PK and IM Cohen (2008). *Fluid Mechanics 4th Edition*. Academic Press.

LaCasce, JH (2008). "Statistics from Lagrangian observations". *Prog Oceanogr* 77.1, pp. 1–29.

Lacy, JR and SG Monismith (2001). "Secondary currents in a curved, stratified, estuarine channel". *J Geophys Res* 106.C12, pp. 31283–31302.

Lacy, JR, MT Stacey, JR Burau, and SG Monismith (2003). "Interaction of lateral baroclinic forcing and turbulence in an estuary". *J Geophys Res* 108.C3, p. 3089.

Lerczak, J, WR Geyer, and RJ Chant (2006). "Mechanisms driving the time-dependent salt flux in a partially stratified estuary". *J Phys Oceanogr* 36, pp. 2296–2311.

Lerczak, JA and WR Geyer (2004). "Modeling the lateral circulation in straight, stratified estuaries". *J Phys Oceanogr* 34.6, pp. 1410–1428.

Li, C and J O'Donnell (1997). "Tidally driven residual circulation in shallow estuaries with lateral depth variation". *J Geophys Res* 102.C13, pp. 27915–27929.

Li, M, S Radhakrishnan, U Piomelli, and WR Geyer (2010). "Large-eddy simulation of the tidal-cycle variations of an estuarine boundary layer". *J Geophys Res* 115, p. C08003.

Lohrmann, A, B Hackett, and L Røed (1990). "High-resolution measurements of turbulence, velocity and stress using a pulse-to-pulse coherent sonar". *J Atmos Ocean Tech* 7.1, pp. 19–37.

Lorke, A and A Wuest (2005). "Application of coherent ADCP for turbulence measurements in the bottom boundary layer". *J Atmos Ocean Tech* 22.11, pp. 1821–1828.

Lu, YY and RG Lueck (1999). "Using a broadband ADCP in a tidal channel. Part II: Turbulence". *J Atmos Ocean Tech* 16.11, pp. 1568–1579.

Lucas, LV, JR Koseff, SG Monismith, JE Cloern, and JK Thompson (1999). "Processes governing phytoplankton blooms in estuaries. II: The role of horizontal transport". *Mar Ecol-Prog Ser* 187, pp. 17–30.

Lucas, LV, JR Koseff, SG Monismith, and JK Thompson (2009). "Shallow water processes govern system-wide phytoplankton bloom dynamics: A modeling study". *J Marine Syst* 75.1-2, pp. 70–86.

MacCready, P (1999). "Estuarine adjustment to changes in river flow and tidal mixing". *J Phys Oceanogr* 29.4, pp. 708–726.

— (2004). "Toward a unified theory of tidally-averaged estuarine salinity structure". *Estuaries* 27.4, pp. 561–570.

MacCready, P and NS Banas (2011). "Residual Circulation, Mixing, and Dispersion". *Treatise on Estuarine and Coastal Science* 2. Ed. by Wolanski E and McLusky DS, pp. 75–90.

MacCready, P and WR Geyer (2010). "Advances in Estuarine Physics". *Annu Rev Marine Sci* 2.1, pp. 35–58.

Michalke, A (1964). "On the inviscid instability of the hyperbolic-tangent velocity profile". *J Fluid Mech* 19.4, pp. 543–556.

Mied, RP, RA Handler, and TE Evans (2000). "Longitudinal convergence fronts in homogeneous rotating channels". *J Geophys Res* 105.C4, pp. 8647–8658.

Mied, RP, RA Handler, and TF Donato (2002). "Regions of estuarine convergence at high Rossby number: A solution in estuaries with elliptical cross sections". *J Geophys Res* 107.C11, p. 3206.

Miles, JW (1961). "On the stability of heterogeneous shear flows". *J Fluid Mech* 10.4, pp. 496–508.

Monismith, SG, W Kimmerer, JR Burau, and MT Stacey (2002). "Structure and flow-induced variability of the subtidal salinity field in northern San Francisco Bay". *J Phys Oceanogr* 32.11, pp. 3003–3019.

Nunes, R and JH Simpson (1985). "Axial convergence in a well-mixed estuary". *Estuar Coast Shelf S* 20.5, pp. 637–649.

Ott, MW and C Garrett (1998). "Frictional estuarine flow in Juan de Fuca Strait, with implications for secondary circulation". *J Geophys Res* 103.C8, pp. 15657–15666.

Ott, MW, R Dewey, and C Garrett (2002). "Reynolds stresses and secondary circulation in a stratified rotating shear flow". *J Phys Oceanogr* 32.11, pp. 3249–3268.

Ozkan-Haller, HT and JT Kirby (1999). "Nonlinear evolution of shear instabilities of the long-shore current: A comparison of observations and computations". *J Geophys Res* 104.C11, pp. 25953–25984.

Peters, H (1999). "Spatial and temporal variability of turbulent mixing in an estuary". *J Mar Res* 57, pp. 805–845.

Peters, H and R Bokhorst (2000). "Microstructure observations of turbulent mixing in a partially mixed estuary. Part I: Dissipation rate". *J Phys Oceanogr* 30.6, pp. 1232–1244.

Peterson, DH and JF Festa (1984). "Numerical-simulation of Phytoplankton Productivity in Partially Mixed Estuaries". *Estuar Coast Shelf S* 19.5, pp. 563–589.

Pope, SB (2000). *Turbulent Flows*. Cambridge University Press.

Pritchard, DW (1952a). "Estuarine Hydrography". *Adv Geophys* 1, pp. 243–280.

— (1952b). "Salinity distribution and circulation in the Chesapeake bay estuarine system". *J Mar Res* 11.2, pp. 106–123.

Rippeth, TP, NR Fisher, and JH Simpson (2001). "The cycle of turbulent dissipation in the presence of tidal straining". *J Phys Oceanogr* 31.8, pp. 2458–2471.

Rodi, W (1987). "Examples of calculation methods for flow and mixing in stratified fluids". *J Geophys Res* 92.C5, pp. 5305–5328.

Schumann, U and T Gerz (1995). "Turbulent mixing in stably stratified shear flows". *J Appl Meteorol* 34.1, pp. 33–48.

Scully, ME, WR Geyer, and JA Lerczak (2009). "The Influence of Lateral Advection on the Residual Estuarine Circulation: A Numerical Modeling Study of the Hudson River Estuary". *J Phys Oceanogr* 39.1, pp. 107–124.

Shaw, WJ, JH Trowbridge, and AJ Williams (2001). "Budgets of turbulent kinetic energy and scalar variance in the continental shelf bottom boundary layer". *J Geophys Res* 106.C5, pp. 9551–9564.

Signell, RP and WR Geyer (1991). "Transient eddy formation around headlands". *J Geophys Res* 96.C2, pp. 2561–2575.

Simpson, JH, J Brown, J Matthews, and G Allen (1990). "Tidal straining, density currents, and stirring in the control of estuarine stratification". *Estuaries* 13.2, pp. 125–132.

Simpson, JH, WR Crawford, TP Rippeth, AR Campbell, and JVS Cheok (1996). "The vertical structure of turbulent dissipation in shelf seas". *J Phys Oceanogr* 26.8, pp. 1579–1590.

Simpson, JH, H Burchard, NR Fisher, and TP Rippeth (2002). "The semi-diurnal cycle of dissipation in a ROFI: model-measurement comparisons". *Cont Shelf Res* 22.11-13, pp. 1615–1628.

Smith, R (1976). "Longitudinal dispersion of a buoyant contaminant in a shallow channel". *J Fluid Mech* 78, pp. 677–688.

Socolofsky, SA and GH Jirka (2004). "Large-scale flow structures and stability in shallow flows". *J Environ Eng Sci* 3.5, pp. 451–462.

Speziale, CG (1991). "Analytical methods for the development of Reynolds-stress closures in turbulence". *Annu Rev Fluid Mec* 23, pp. 107–157.

Spydell, MS, F Feddersen, and RT Guza (2009). "Observations of drifter dispersion in the surfzone: The effect of sheared alongshore currents". *J Geophys Res* 114, p. C07028.

Stacey, MT (2003). "Estimation of diffusive transport of turbulent kinetic energy from acoustic Doppler current profiler data". *J Atmos Ocean Tech* 20.6, pp. 927–935.

Stacey, MT and DK Ralston (2005). "The scaling and structure of the estuarine bottom boundary layer". *J Phys Oceanogr* 35.1, pp. 55–71.

Stacey, MT, SG Monismith, and JR Burau (1999a). "Measurements of Reynolds stress profiles in unstratified tidal flow". *J Geophys Res-Oceans* 104.C5, pp. 10933–10949.

— (1999b). "Observations of turbulence in a partially stratified estuary". *J Phys Oceanogr* 29.8, pp. 1950–1970.

Stacey, MT, JR Burau, and SG Monismith (2001). "Creation of residual flows in a partially stratified estuary". *J Geophys Res-Oceans* 106.C8, pp. 17013–17037.

Stacey, MT, TP Rippeth, and JD Nash (2012). "Turbulence and Stratification in Estuaries and Coastal Seas". *Treatise on Estuarine and Coastal Science* 2, pp. 9–36.

Taylor, G (1953). "Dispersion of Soluble Matter in Solvent Flowing slowly through a Tube". *Proc R Soc Lond A* 219, pp. 186–203.

Trowbridge, JH, WR Geyer, MM Bowen, and AJ Williams (1999). "Near-bottom turbulence measurements in a partially mixed estuary: Turbulent energy balance, velocity structure, and along-channel momentum balance". *J Phys Oceanogr* 29.12, pp. 3056–3072.

Turner, JS (1973). *Buoyancy Effects in Fluids*. Cambridge University Press.

Umlauf, L and H Burchard (2003). "A generic length-scale equation for geophysical turbulence models". *J Mar Res* 61.2, pp. 235–265.

Umlauf, Lars, Hans Burchard, and Karsten Bolding (2007). *GOTM Sourcecode and Test Case Documentation*, pp. 1–360.

Valle-Levinson, A and LP Atkinson (1999). "Spatial gradients in the flow over an estuarine channel". *Estuaries* 22.2A, pp. 179–193.

Valle-Levinson, A, CY Li, KC Wong, and KMM Lwiza (2000). "Convergence of lateral flow along a coastal plain estuary". *J Geophys Res* 105.C7, pp. 17045–17061.

Valle-Levinson, A, WC Boicourt, and MR Roman (2003). "On the linkages among density, flow, and bathymetry gradients at the entrance to the Chesapeake Bay". *Estuaries* 26.6, pp. 1437–1449.

Valle-Levinson, A, WR Geyer, CT Friedrichs, D Jay, RJ Chant, C Winant, SG Monismith, J O'Donnell, J Largier, and LV Lucas (2010). *Contemporary Issues in Estuarine Physics*. Cambridge University press.

Vallis, GK (2006). *Atmospheric And Oceanic Fluid Dynamics: Fundamentals And Large-scale Circulation*. Cambridge University Press.

VanProoijen, BC and W Uijttewaal (2002). "A linear approach for the evolution of coherent structures in shallow mixing layers". *Phys Fluids* 14.12, pp. 4105–4114.

VanProoijen, BC, JA Battjes, and WSJ Uijttewaal (2005). "Momentum exchange in straight uniform compound channel flow". *J Hydraul Eng* 131.3, pp. 175–183.

Wiles, PJ, TP Rippeth, JH Simpson, and PJ Hendricks (2006). "A novel technique for measuring the rate of turbulent dissipation in the marine environment". *Geophys Res Lett* 33.21, p. L21608.